Virginia Commonwealth University

VCU Scholars Compass

2023

Novel Development of a Low-Cost, Micrometer-Scale Tip-Enhanced Raman Spectroscopy System

John Yates
Virginia Commonwealth University

Novel Development of a Low-Cost, Micrometer-Scale Tip-Enhanced Raman Spectroscopy

System

A dissertation submitted in partial fulfillment of the requirements for the degree of Doctor of

Philosophy at Virginia Commonwealth University

by

John Wayne Yates

BS Physics – Virginia Commonwealth University 2017

AS – Lord Fairfax Community College 2015

Director: Massimo Bertino, Department of Physics

Virginia Commonwealth University

Richmond, Virginia

May, 2023

Acknowledgements

I want to say thank you to several people that I could not have completed this project without. First, I would like the friends I have gained along the way during my time at VCU: Roemello Armstrong, Ryan Lambert, Bobby Cox, Tyler Selden, and Tristan Moon. You kept me sane and served as a sounding board for my frustrations with school, research, and life. I would like to thank my research committee as well for helping me to narrow down, prepare, and execute a successful thesis proposal and defense. I, of course, cannot thank my family enough. My cousins, aunts/uncles, and my brothers helped to keep me motivated and lifted me when I was down, whether you knew it. I want to extend a very special statement of appreciation to my parents, John and Kim Yates, who have supported me in my every changing and extensive academic career from the first day of school to whenever my last day of school will be. My grandparents, John and Brenda Yates, were and are instrumental in the moral support of my studies and the pride they show in my studies kept me going. Finally, I want to thank the two most important people in my life; my son, John, it fills me with joy seeing your face light up talking about science and pushed me to keep going, to prove to you that you can do anything you put your mind to. My fiancée, Ruthie Rowane, you were with me every step of the way. Pushing me, supporting me, challenging me through this degree and I could not have done it without you. Once again, thank you all and we finally did it!

Table of Contents

List of Tables

List of Figures

ix

List of Abbreviations

AFM – Atomic Force Microscopy

ASCII – American Standard Code for Information Interchange

AgNP – Silver Nanoparticle

CCD – Charged-coupled Device

Cl – Chloride

DI – Deionized

EM – Electromagnetic

GUI – Graphical User Interface

HCl – Hydrochloric Acid

IR – Infrared

NaCl – Sodium Chloride

OD – Optical Density

QTF – Quartz Tuning Fork

SERS – Surface Enhanced Raman Spectroscopy

SPP – Surface Plasmon

SPP – Surface Plasmon Polariton

TE – Transverse Electric Field

TERS – Tip Enhanced Raman Spectroscopy

TM – Transverse Magnetic Field

w.r.t. – with respect to

UV – Ultraviolet

UV-Vis – Ultraviolet to Visible Light

VI – Virtual Instrument

Abstract

Modern scientific instruments are significant capital investments for universities. These investments can be outside of the funding capabilities of some smaller universities or departments and can be a significant barrier in the pursuit of scientific breakthroughs. This project aims to provide a template for universities or research groups to upgrade, at a reasonable price, an existing Raman spectroscopy system to a Tip-Enhanced Raman Spectroscopy (TERS) system. This system can serve as a permanent upgrade to an existing system or as a bridge necessary to prove the viability of a research path before significant capital investment in a commercial TERS system. This project explains, in detail, all required components of a TERS system and the rationale of each designed component. The enhancement factor demonstrated using this homebuilt TERS system shows the potential of this system as an alternative to much more expensive commercial systems.

1.   Raman Theory

1.1   Introduction to Raman Spectroscopy

Raman spectroscopy is a characterization technique utilizing the Raman scattering

phenomenon. The scattering events were first theorized by Austrian theoretical physicist Adolf

Smekal in 1923 [1] and then experimentally confirmed by Indian experimental physicists C.V.

Raman and K.S. Krishnan in 1928 [2]. These early experiments utilized focused, filtered broad

spectrum light, usually from the sun or a high-powered lamp. Modern day Raman spectroscopy

setups utilize coherent laser setups passing through microscopes into a mirror setup with

specialized filters to block out the source laser before hitting diffraction gratings with CCD

cameras as seen in Figure 1.
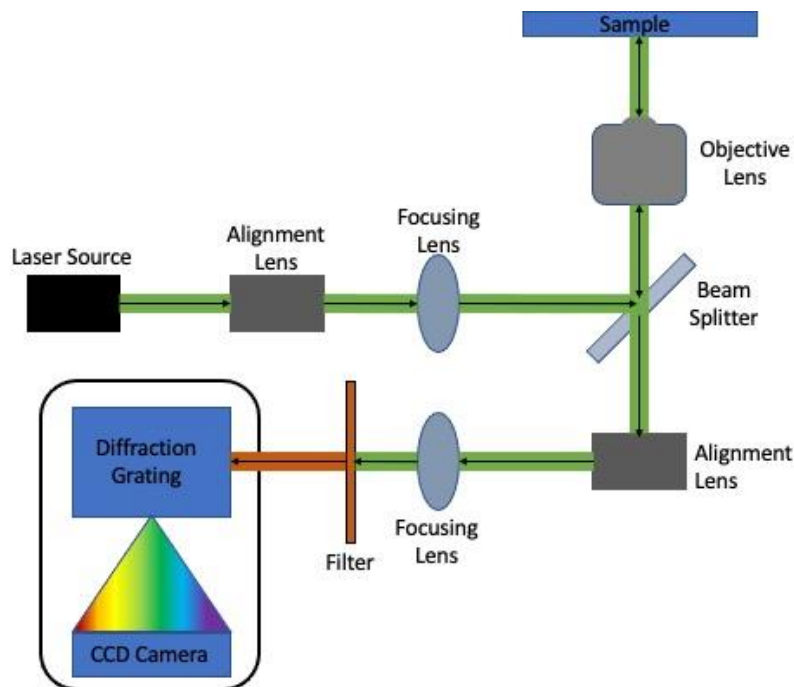
Figure 1: Basic Raman Spectroscopic Setup.

The Raman scattered light is a different wavelength than the incident laser wavelength. Most of the incident light that is scattered will have the same wavelength as the incident light and is known as Rayleigh scattering. The incoming photons from the coherent laser have a very low possibility of either shifting to a longer wavelength or a shorter wavelength, a Stokes shift or anti-Stokes shift respectively. It is this wavelength shift due to interactions of the laser with the chemical bonds of the sample that is the Raman effect. For a photon to experience an anti-Stokes shift, it must absorb energy from the bond that scattered the photon. This is only possible if the target bond is in an excited energy state and according to the Boltzmann distribution of energy levels with respect to temperature explored later, the anti-Stokes shift signal would increase with increasing temperature and the corresponding Stokes shift would decrease with increasing temperature.
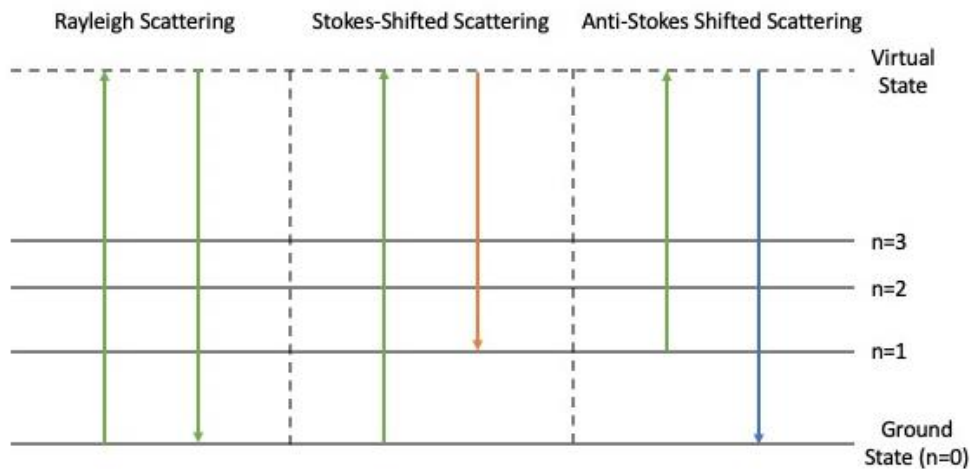
Figure 2: Incident Light Scattering Energy Levels

Raman spectroscopy is an important characterization technique because it is a non-destructive analysis tool that has the capability to determine the chemical bond fingerprints of

potentially complex molecules. The samples do not have to be in physical contact with the Raman spectroscopy system and because Raman frequency shifts do not depend on wavelength, it is possible to use a variety of enclosures and wavelengths of light as noted in Figure 3 as the Raman effect is caused by the vibration of the bonded valence electrons in a molecule. This allows research teams such as NASA's Perseverance Mars Rover to search for the chemical fingerprints of life on Mars using a deep-UV Raman setup known as SHERLOC [3] to take advantage of the fluorescence of organic molecules when exposed to UV light.

Radiowaves		Microwaves	Far-IR	IR	Vis	UV	X-Rays
Nuclear Spin in Magnetic field	Electron Spin in Magnetic Field	Molecular Rotation		Internuclear Vibrations	Valence Electrons Orbital Motions		Inner Shell Electron Energy

| $\lambda(m)$ | 10^0 | 10^{-1} | 10^{-2} | 10^{-3} | 10^{-4} | 10^{-5} | 10^{-6} | 10^{-7} | 10^{-8} |

Figure 3: Spectroscopic Wavelength Characteristics

From Figure 3, it is apparent that IR-spectroscopy would also overlap with Raman spectroscopy as both share a piece of the valence electron orbital motion. In terms of basic setups, the Raman spectra is a scattering spectrum with peaks corresponding to the chemical bond energies while IR-spectroscopy is an absorption spectrum with valleys corresponding to the chemical bonds. The difference in the origin of the two types of spectroscopies will explained in greater detail in section 1.3 but a general overview is that the Raman effect requires the change in polarization while for a molecule to be IR-active it must have a change in the electric dipole moment of the molecule. A molecule can be either Raman-active, IR-active,

3

or both when irradiated and depends on the set of rules explored in the later section. Raman

and IR-spectroscopy are generally seen as supporting characterization techniques because of

the selection rules, if a molecule is not IR-active it will be Raman-active. This allows for the

analysis of any molecule through at least one of the two characterization techniques.

1.2   Raman Effect Origin

To determine the expected Raman scattering frequencies of a molecule, we must define the

frequencies of the light scattered from a molecule irradiated by a light source and the vibration

of a diatomic bond in a diatomic molecule. We start at the classical definition of the electric

field strength (E) of an electromagnetic wave, generally a laser beam

$$E = E_0 cos(2\pi v_0 t) \tag{1-1}$$

The term E_0 is the maximum vibrational amplitude of the beam and the term v_0 is the

frequency of the laser beam. For the Raman effect, a molecule must be irradiated with the

beam and cause a change in polarization. The irradiation causes an electric dipole moment P to

be induced

$$P = \alpha E \tag{1-2}$$

$$P = \alpha E_0 cos(2\pi v_0 t) \tag{1-3}$$

The term α is the proportionality constant and is known as the polarizability of the molecule. If

the irradiation causes the molecule to vibrate at a frequency of v_m, we can write the nuclear

displacement (q) as

$$q = q_0 cos(2\pi v_m t) \tag{1-4}$$

Using similar logic as in (1-1) to explain the motion as a wave, the maximum amplitude is

defined as q_0. If we assume that the vibrations of the diatomic molecule are small enough, we

can use a linear approximation of the power series expansion with respect to α

$$\alpha = \alpha_0 + \left(\frac{\partial \alpha}{\partial q}\right)_0 q + \cdots \tag{1-5}$$

For this expansion, α_0 is the polarizability at the equilibrium position. The partial derivative of

the polarizability with respect to the change in displacement $\left(\frac{\partial \alpha}{\partial q}\right)_0$ is according to the

equilibrium position. We can combine the two equations (1-4) and (1-5) then we can take that

solution and substitute it into (1-3) for a equation that describes the different frequencies of

the scattered light from the irradiation of a diatomic molecule by a laser beam

$$\alpha = \alpha_0 + \left(\frac{\partial \alpha}{\partial q}\right)_0 q_0 cos(2\pi v_m t) \tag{1-6}$$

$$P = \alpha_0 E_0 cos(2\pi v_0 t) + \left(\frac{\partial \alpha}{\partial q}\right)_0 q_0 E_0 cos(2\pi v_m t) cos(2\pi v_0 t) \tag{1-7}$$

This equation can finally be expanded out further using the trigonometric identity

$cos(a)cos(b) = cos(a + b) + cos(a - b)$ on the second term which is important for the

definitions of the observed Raman frequencies

$$P = \alpha_0 E_0 cos(2\pi v_0 t) + \left(\frac{\partial \alpha}{\partial q}\right)_0 q_0 E_0 [cos(2\pi(v_0 + v_m)t) + cos(2\pi(v_0 - v_m)t)] \tag{1-8}$$

The first term in this final equation relates to a scattered light of the same frequency as the

incident light which is the definition of a Rayleigh scattered photon. The two remaining terms in

the equation describe photons of higher frequency (shorter wavelength) or lower frequency

(longer wavelength) with respect to the incident light from the laser. The shift to a higher

5

frequency or shorter wavelength is the previously mentioned anti-Stokes shifted Raman

scattering while the lower frequency or longer wavelength shift is the Stokes shifted Raman

scattering. From the second and third terms having a dependency on the change in

polarizability term. It is easy to see that for a molecule to have Raman scattering events, it must

have a non-zero change in polarizability while vibrating.

1.2.1   Classical Vibration Framework

The mathematical description of the vibrations needed to generate the change in

polarization of the diatomic molecule was originally a classical explanation. The vibrational

energy of the system must be calculated to determine the energy range of the scattered

photons. The diatomic molecules can be approximated as two balls with a given mass and the

chemical bond between them can be approximated as a spring. We will use the following

physical setup in our mathematically explanation.
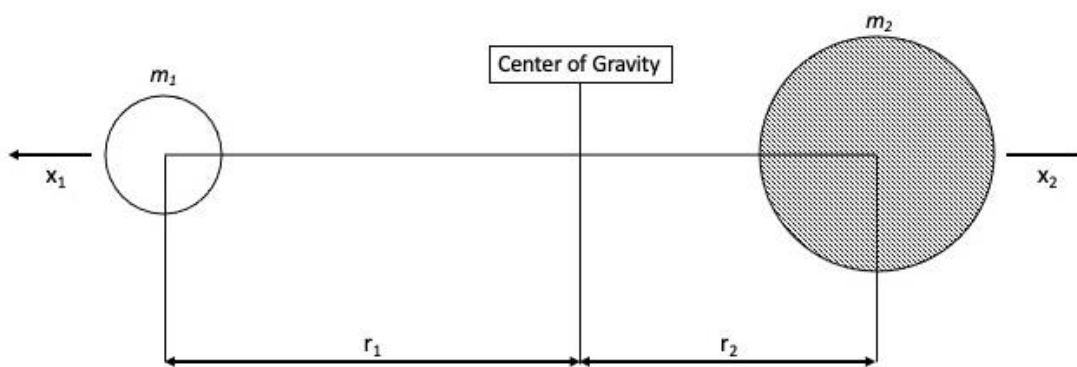
Figure 4: Diatomic Molecule Approximation

The center of gravity for this diatomic molecule is the point at which the weight of the molecule

on the left is equal to the weight on the right which we can define as:

$$m_1 r_1 = m_2 r_2 \qquad (1\text{-}9)$$

The movement of the molecules due to vibrations is labeled in the diagram as movement along

the x-axis and is incorporated into the conservation of the center of gravity above as:

$$m_1(r_1 + x_1) = m_2(r_2 + x_2) \qquad (1\text{-}10)$$

The above equation can be further modified by using equation (1-1) to remove the components

that do not have an x-term. We do this by substituting either side of (1-1) and then subtracting

that substituted term from both sides. This leaves the modified form

$$m_1 x_1 = m_2 x_2 \qquad (1\text{-}11)$$

Since the chemical bond is approximated as a spring, we can use Hooke's Law to define the

total restoring force on the system

$$f_{TOT} = -k(x_1 + x_2) \qquad (1\text{-}12)$$

We can substitute values of x_1 or x_2 into (1-4) by rearranging (1-3) and substituting these values

to focus solely on either x-component, we get the restoring force on either atom

$$f_1 = -k\left(\frac{m_1 + m_2}{m_2}\right)x_1 \qquad (1\text{-}13)$$

$$f_2 = -k\left(\frac{m_1 + m_2}{m_1}\right)x_2 \qquad (1\text{-}14)$$

The restoring force can be rewritten in the style of Newton's Second Law ($f = ma$) by using the

components above and the definition that acceleration is the second derivative of position with

respect to time and determining the

$$m_1 \frac{d^2 x_1}{dt^2} = -k \left(\frac{m_1 + m_2}{m_2} \right) x_1 \tag{1-15}$$

$$m_2 \frac{d^2 x_2}{dt^2} = -k \left(\frac{m_1 + m_2}{m_1} \right) x_2 \tag{1-16}$$

Since equations (1-7) and (1-8) are the individual restoring forces on their respective atoms, we have to combine them for a total restoring force on the system of atoms. We do this by having

(1-7) $\times \frac{m_2}{m_1 + m_2}$ and (1-8) $\times \frac{m_1}{m_1 + m_2}$

$$\left(\frac{m_1 m_2}{m_1 + m_2} \right) \frac{d^2 x_1}{dt^2} = -k x_1 \tag{1-17}$$

$$\left(\frac{m_1 m_2}{m_1 + m_2} \right) \frac{d^2 x_2}{dt^2} = -k x_2 \tag{1-18}$$

By putting these equations together as in (1-4) and using the definitions of reduced mass ($\mu = \frac{m_1 m_2}{m_1 + m_2}$) and the definition of displacement ($q = x_1 + x_2$). The displacement is only in the x-direction for this example derivation.

$$\mu \left(\frac{d^2 x_1}{dt^2} + \frac{d^2 x_2}{dt^2} \right) = -k(x_1 + x_2) \tag{1-19}$$

$$\mu \left(\frac{d^2 q}{dt^2} \right) = -kq \tag{1-20}$$

The solution to this simple differential equation is widely known

$$q = q_0 \sin(2\pi v_0 t + \phi) \tag{1-21}$$

The phase constant for the displacement term (ϕ) is between 0 and π at positions of maximum +x-direction or maximum -x-direction respectively. The q_0 term is the maximum displacement and the v_0 term is the classical frequency of the vibration

8

$$v_0 = \frac{1}{2\pi}\sqrt{\frac{k}{\mu}} \tag{1-22}$$

We can follow through to determine the potential energy, kinetic energy, and the type of oscillatory motion this diatomic molecule will follow. This will be important with regards to relating the classical framework with the quantum-mechanical framework. The potential energy (V) is defined as

$$dV = -f\,dq = kq\,dq \tag{1-23}$$

$$V = \frac{1}{2}kq^2 \tag{1-24}$$

$$V = \frac{1}{2}kq_0^2 \sin^2(v_0 t + \phi) \tag{1-25}$$

We can use (1-22) rearranged with respect to k to rewrite (1-25)

$$V = 2\pi^2 v_0^2 \mu q_0^2 \sin^2(v_0 t + \phi) \tag{1-26}$$

The kinetic energy (T) of the system can be written using the definition of velocity as the first derivative with respect to position (x)

$$T = \frac{1}{2}m_1\left(\frac{dx_1}{dt}\right)^2 + \frac{1}{2}m_2\left(\frac{dx_2}{dt}\right)^2 \tag{1-27}$$

Using the definitions of reduced mass and displacement again, we can rewrite (1-27)

$$T = \frac{1}{2}\mu\left(\frac{dq}{dt}\right)^2 \tag{1-28}$$

$$T = 2\pi^2 v_0^2 \mu q_0^2 \cos^2(v_0 t + \phi) \tag{1-29}$$

Finally, the total energy of the system (E) can be written with the trig identity of ($cos^2 + sin^2 = 1$)

$$E = 2\pi^2 v_0^2 \mu q_0^2 \tag{1-30}$$

The potential energy is a parabolic function with a minima at $q = 0$ and maxima at $q = \pm q_0$, it

follows then that the kinetic energy has the opposite values at the previously mentioned

values.
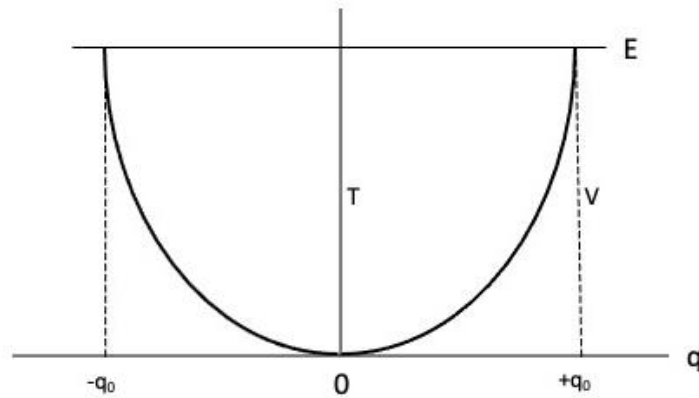
Figure 5: Energy Diagram of Harmonic Oscillator

1.2.2   Quantum-Mechanical Framework

The quantum-mechanical derivation for the Raman effect was first put forward by Albrecht [4]

in 1961. The explanation by Ferraro, Nakamoto, and Brown in *Introductory Raman Spectroscopy*

is an excellent reference source for the framework but does not start from the beginning, the

Maxwell Wave equation but rather jumps into Schrödinger's equation for a diatomic molecule

treated as a single particle in motion with potential [5]. For the fullness of the quantum-

mechanical explanation for the energy range of the scattered photons, it is necessary to begin

with the Maxwell equation for an electromagnetic wave and proceed to the necessary solution

previously mentioned.

$$\nabla^2\vec{E} - \frac{1}{c^2}\frac{\partial^2\vec{E}}{\partial t^2} = 0 \tag{1-31}$$

If we can restrict the electric component into just the x-axis, we can rewrite the equation

$$\frac{\partial^2\vec{E}}{\partial x^2} - \frac{1}{c^2}\frac{\partial^2\vec{E}}{\partial t^2} = 0 \tag{1-32}$$

The solution for the electric component of the wave would then be

$$\vec{E}(x,t) = \vec{E_0}e^{i(kx-\omega t)} \tag{1-33}$$

We can plug this back into (1-32) and solve

$$\left(\frac{\partial^2}{\partial x^2} - \frac{1}{c^2}\frac{\partial^2}{\partial t^2}\right)\vec{E_0}e^{i(kx-\omega t)} = 0 \tag{1-34}$$

$$\left(k^2 - \frac{\omega^2}{c^2}\right)\vec{E_0}e^{i(kx-\omega t)} = 0 \tag{1-35}$$

This proves that electromagnetic waves move at a speed of c

$$\omega = ck \tag{1-36}$$

We now consider the definitions of energy and momentum for a photon by the photoelectric effect and Compton scattering respectively

$$E = h\nu = \hbar\omega \tag{1-37}$$

$$p = \frac{h}{\lambda} = \hbar k \tag{1-38}$$

We can use these definitions to rewrite the k and ω terms in (1-34)

$$\vec{E}(x,t) = \vec{E_0}e^{i\left(\frac{p}{\hbar}x - \frac{E}{\hbar}t\right)} \tag{1-39}$$

$$\vec{E}(x,t) = \vec{E_0}e^{\frac{i}{\hbar}(px - Et)} \tag{1-40}$$

Once we apply the operators from (1-34) to (1-39), we have a solution for the wave equation with regards to the momentum and energy of the photon with an electric field moving in the x-axis as before

$$\left(\frac{\partial^2}{\partial x^2} - \frac{1}{c^2}\frac{\partial^2}{\partial t^2}\right)\overrightarrow{E_0}e^{\frac{i}{\hbar}(px-Et)} = 0 \qquad (1\text{-}41)$$

$$\left(p^2 - \frac{E^2}{c^2}\right)\overrightarrow{E_0}e^{\frac{i}{\hbar}(px-Et)} = 0 \qquad (1\text{-}42)$$

The solutions provided give the energy-momentum relationship for a moving, massless particle subject to no potential

$$E^2 = c^2p^2 \qquad (1\text{-}43)$$

The next step in the progression is to consider a particle with a non-zero rest mass that is moving at relativistic speeds. The wave equation operator must return the modified energy-momentum relationship

$$E^2 = c^2p^2 + m_0^2c^4 \qquad (1\text{-}44)$$

The second term is the non-zero rest mass for a particle moving at relativistic speeds. Since we are no longer using a photon, we will use the notation preferred by Schrödinger for wave functions (ϕ). In the new notation, the constant (A) is used in the place of $\overrightarrow{E_0}$. We know that from (1-41) that the plane wave operator returns (1-43). For the operator to return in the form of (1-44), we need to add a constant term into the operator of $\frac{m_0^2c^4}{\hbar^2}$. The logic of this constant term is shown

$$\phi(x,t) = Ae^{\frac{i}{\hbar}(px-Et)} \qquad (1\text{-}45)$$

$$\left(\frac{\partial^2}{\partial x^2} - \frac{1}{c^2}\frac{\partial^2}{\partial t^2} - \frac{m_0^2 c^4}{\hbar^2}\right) A e^{\frac{i}{\hbar}(px - Et)} = 0 \tag{1-46}$$

$$-\frac{1}{\hbar^2}\left(p^2 - \frac{E^2}{c^2} - m_0^2 c^4\right) A e^{\frac{i}{\hbar}(px - Et)} = 0 \tag{1-47}$$

This equation is known as the Klein-Gordon equation, but this equation is not applicable for the

Raman effect as it describes the relativistic motion. If we follow the same logic as above but use

the energy-momentum relationship for a non-relativistic particle ($E = \frac{p^2}{2m}$). We will use the

same wave function from (1-34) to describe a non-relativistic, non-zero rest mass particle. The

desired energy-momentum relationship though does not have a E^2 like (1-44) so the wave

function operator cannot have a second-derivative with respect to time and there is no c^2 term

either. The new wave equation can be written as

$$i\hbar \frac{\partial \phi(x,t)}{\partial t} + \frac{\hbar^2}{2m}\frac{\partial^2 \phi(x,t)}{\partial x^2} = 0 \tag{1-48}$$

$$\left(i\hbar \frac{\partial}{\partial t} + \frac{\hbar^2}{2m}\frac{\partial^2}{\partial x^2}\right) A e^{\frac{i}{\hbar}(px - Et)} = 0 \tag{1-49}$$

If we perform the operator on the wave equations to get a solution for the energy-momentum

relationship while ignoring the constant A

$$\left(E - \frac{p^2}{2m}\right) A e^{\frac{i}{\hbar}(px - Et)} = 0 \tag{1-50}$$

The solution satisfies the energy-momentum relationship for the non-relativistic particle and

the equation (1-38) is Schrödinger's equation for a free particle. No particle exists without being

subject to some potential so we must account for that in the wave function operator and the

13

energy-momentum relationship. This relationship for the non-relativistic, non-zero rest mass

particle can be shown for a non-constant potential $(V(x))$

$$E = \frac{p^2}{2m} + V(x) \tag{1-51}$$

The momentum of the particle varies as time progresses because the particle moves from a

point of maximum momentum to lowest momentum due to its interaction with the potential. If

we consider the wave function for the particle at a given point x, this will allow the same logic

shown in (1-48) to be used.

$$i\hbar \frac{\partial \phi(x,t)}{\partial t} + \frac{\hbar^2}{2m} \frac{\partial^2 \phi(x,t)}{\partial x^2} - V(x)\phi(x,t) = 0 \tag{1-52}$$

$$\left[i\hbar \frac{\partial}{\partial t} + \frac{\hbar^2}{2m} \frac{\partial^2}{\partial x^2} - V(x) \right] \phi(x,t) = 0 \tag{1-53}$$

This modified wave function operator generates the needed solution of (1-51) and is known as

the one-dimensional Schrödinger equation. The final steps would be to expand this equation

out into the 3 Cartesian coordinate dimensions and substitute the definition of displacement

into the equation

$$\left[i\hbar \frac{\partial}{\partial t} + \frac{\hbar^2}{2m} \left(\frac{\partial^2}{\partial x^2} + \frac{\partial^2}{\partial y^2} + \frac{\partial^2}{\partial z^2} \right) - V(x,y,z) \right] \phi(x,y,z,t) = 0 \tag{1-54}$$

$$\left[i\hbar \frac{\partial}{\partial t} + \frac{\hbar^2}{2m} \frac{\partial^2}{\partial q^2} - V(q) \right] \phi(q,t) = 0 \tag{1-55}$$

This the standard Schrödinger's equation and the starting point for a quantum-mechanical

explanation for a diatomic molecule Raman effect. The diatomic molecule though is treated as

a single particle with reduced mass (μ). From the classical framework equation (1-24), we can

rewrite the Schrödinger equation for the diatomic molecule

$$\left[i\hbar\frac{\partial}{\partial t} + \frac{\hbar^2}{2\mu}\frac{\partial^2}{\partial q^2} - \frac{1}{2}kq^2\right]\phi(q,t) = 0 \tag{1-56}$$

The solutions to this equation must be single-valued, finite, and continuous. These conditions

give us the eigenvalues

$$E_n = h\nu\left(n + \frac{1}{2}\right) \tag{1-57}$$

The frequency of vibration (ν) is described by (1-22) and the n term is the vibrational quantum

number. The n term can only be a whole number starting with 0. The relevant eigenfunctions

that generate solutions

$$\phi_n = \frac{(\alpha/\pi)^{1/4}}{\sqrt{2^n n!}} e^{-\alpha q^2/2} H_n\left(\sqrt{\alpha q}\right) \tag{1-58}$$

The term $H_n\left(\sqrt{\alpha q}\right)$ is a Hermite polynomial of the nth degree and the α can be defined as

$$\alpha = 4\pi^2 \mu\nu/h \tag{1-59}$$

The eigenvalues for the first 3 levels with their corresponding quantum numbers are

$$n = 0 \qquad\qquad E_0 = \frac{1}{2}h\nu$$

$$n = 1 \qquad\qquad E_1 = \frac{3}{2}h\nu \tag{1-60}$$

$$n = 2 \qquad\qquad E_2 = \frac{5}{2}h\nu$$

The verification of the math can be found in Appendix A for the first eigenvalue as the solutions

are further verified through the entire field of quantum-mechanics. The frequencies for the

classical description and the quantum-mechanical description are the same but the energy for

$n = 0$ is markedly different for the classical framework ($E_0 = 0$) when compared to the

quantum-mechanical description ($E_0 = \frac{1}{2}hv$). This lowest energy state agrees with Heisenberg's

uncertainty principle and is the more accurate description of the atomic energy levels. One of

the primary rules for quantum-mechanics is that energy is quantized and can only change in

integers of $\left(n + \frac{1}{2}hv\right)$; creating individual energy levels.

The derivations were based upon the test case of a harmonic oscillator potential which

generated evenly spaced vibrational energy levels. A more accurate approximation of the

potential in a molecule is given by the Morse potential function [6]

$$V = D_e\left(1 - e^{-\beta q}\right)^2 \tag{1-61}$$

For the Morse function, D_e is defined as the dissociation energy (energy change when bond is

broken) and β is the measure of curvature for the bottom of the potential well for the diatomic

molecule. Solving the Schrödinger equation with the new Morse potential gives the following

eigenvalues

$$E_n = hc\omega_3\left(n + \frac{1}{2}\right) - hc\chi_e\omega_e\left(n + \frac{1}{2}\right)^2 + \cdots \tag{1-62}$$

These eigenvalues introduce the wavenumber corrected for the molecule's anharmonicity (ω_e)

and the magnitude of the anharmonicity ($\chi_e\omega_e$) for the potential. The eigenvalues describe a

molecule with energy levels that grow closer together with increasing quantum numbers.
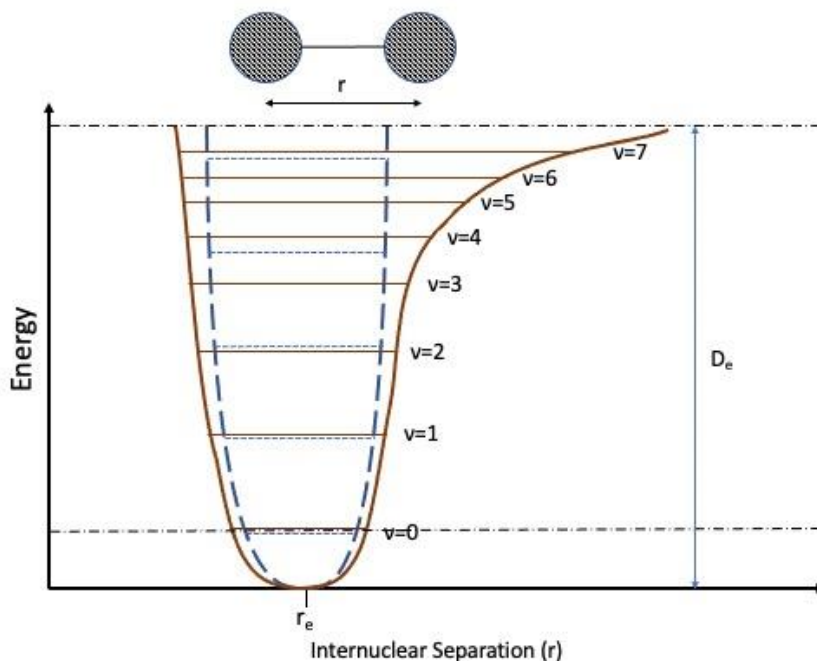
Figure 6: Morse Potential vs Harmonic Oscillator Potential

The excitation of an electron into a higher energy level and then the subsequent relaxation to a lower energy level is the basic definition of how a chemical bond generates a photon. The most dominate transitions for a molecule will generally be of $\Delta n = \pm 1$ of which the fundamental transition from the ground level to the first energy level ($n = 0 \leftrightarrow 1$) is the largest contributor to a Raman spectrum. We can use the Maxwell-Boltzmann distribution to calculate the ratio of the ground state energy level and the first excited energy level for a few different diatomic molecules using values found in Table 1: Sample Diatomic Molecule Vibrational Frequency, Reduced Mass, and Force ConstantsTable 1

$$\frac{P_n}{P_0} = e^{-\Delta E/kT} \tag{1-63}$$

17

Molecule	Obs. $\tilde{v}$ (cm^{-1})	ω_e (cm^{-1})	μ (awu)	k (mdyn/Å)
H_2	4,160	4395	0.5041	5.73
Cl_2	546	565	17.4814	3.19
N_2	2,331	2,360	7.004	22.9

The determination of the population ratio between the first two energy levels ($n = 0,1$) of

hydrogen follows

$$E = hc\tilde{v} \tag{1-64}$$

$$\Delta E = \tilde{v}$$

$$kT = 1.38 \times 10^{-16}(\text{erg}/K) * 300K \tag{1-65}$$

$$kT = 4.14 \times 10^{-14}(\text{erg})/\left[1.99 \times 10^{-16}\left(\frac{\text{erg}}{cm^{-1}}\right)\right] \tag{1-66}$$

$$kT = 208cm^{-1} \tag{1-67}$$

$$\frac{P_1}{P_0} = e^{-4160cm^{-1}/(208cm^{-1})} \tag{1-68}$$

$$\frac{P_1}{P_0} = 2.06 \times 10^{-9} \tag{1-69}$$

This demonstrates that for the diatomic hydrogen molecule at room temperature, virtually all

electrons are in the ground state. The population ratios for Cl_2 (0.07) and N_2 (1.36×10^{-5})

further proves this pattern. The population ratios should begin to favor the higher energy levels

as temperature increase. For room temperature Raman applications, the Stokes shifted spectra

should dominate as more electrons are in the lowest energy levels.

1.3   Selection Rules

The characteristic Raman frequencies of different molecules can be described by the wavelength shift and are caused by the change in polarization as previously demonstrated. The explanations of why certain frequencies appear can be explained by the idea of irreducible representations in Group Theory. The irreducible representations are the different descriptors for translational, rotational, and vibrational degrees of freedom for a molecule also known as the different modes of a molecule. The basics of group theory rely on the four different symmetry elements, ways to classify the different ways a molecule can be symmetric.

The first symmetry element is the most basic, the rotation around a center axis. The notation for rotational symmetry is C_n^m, where $n = 360°/(\text{degree of rotation})$ and m is how many times that rotation was performed. We can observe this symmetry element using the molecule boron trichloride (BF_3) about the axis perpendicular to the center boron atom:
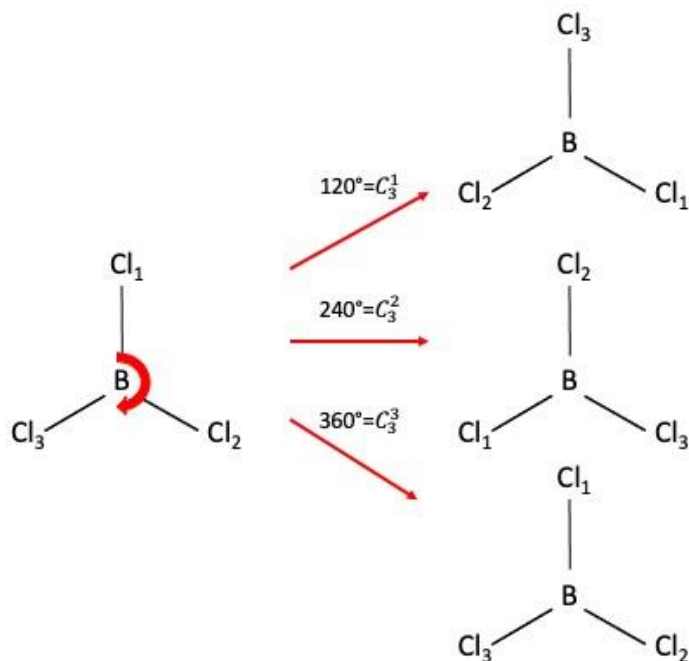
Figure 7: Rotation Symmetry Element Boron Trichloride (BCl₃).

When there are multiple axes of rotation that have symmetry like above, the axis that has the largest n-value is defined as the principal axis. In the case that $m = n$, the rotations return the molecule to the beginning orientation, and this is defined as the identity symmetry operator (E). The identity symmetry operator uses the symbol (E) German for einheit, meaning unity.

The next set of symmetry elements, reflections, have several different variations. In a reflection symmetry element, the molecule is reflected across a mirror plane designated as (σ). There are three further types of reflection that are shown in Figure 8:

- σ_h = horizontal mirror plane that is perpendicular to the main rotation axis

- σ_v = vertical mirror plane that contains the main rotation axis

- σ_d = dihedral mirror planes that are vertical mirror planes that bisect bond angles
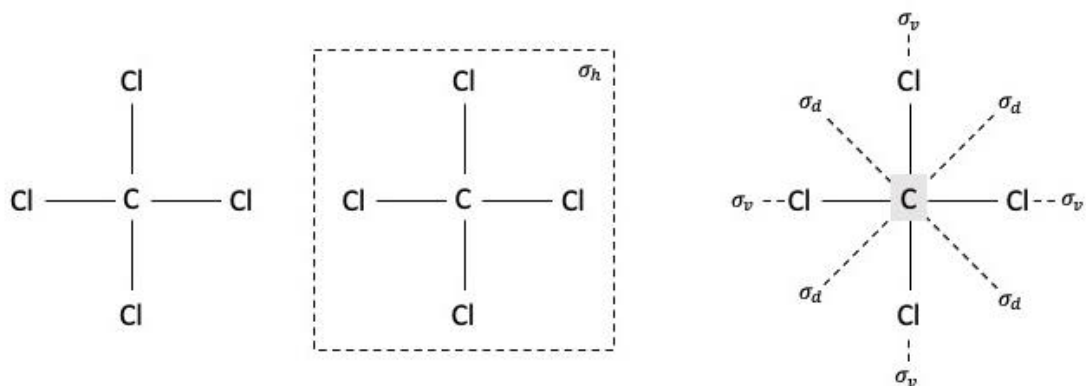
Figure 8: Reflection Symmetry Elements of Carbon Tetrachloride (CCl₄).

The last basic symmetry element involves inverting the molecule through the center of

symmetry. In the case that the molecule's center of symmetry resides at (0,0,0) then it can be

said that $(x, y, z) \rightarrow (-x, -y, -z)$. For molecules that show inversion symmetry, related

molecules are generally notated with a (') on one of the inversion related pairs as show in sulfur

hexafluoride with sulfur as the obvious center of symmetry:
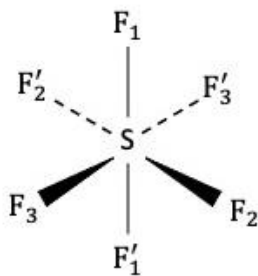
Figure 9: Inversion Symmetry Element of Sulfur Hexafluoride (SF₆).

The final symmetry element and the most complicated of the symmetry elements is the

improper rotation (S_n). This element is a combination of rotational symmetry and reflection

elements. First a molecule is rotated around a C_n-axis and then reflected across an axis that is perpendicular to the rotational axis as shown with Methane (CH_4):
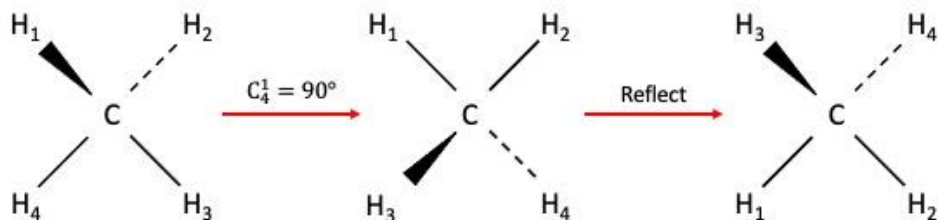
Figure 10: Improper Rotation Symmetry Element of Methane (CH_4).

A symmetry element can be used to transform a molecule and will be designated with a hat so the four symmetry elements as operators are ($\widehat{C_n}, \hat{\sigma}, \hat{\imath}, \widehat{S_n}$) as well as the identity operator ($\hat{E}$). There are only a certain number of ways to arrange atoms in a molecule and thus all molecules that have the same specific symmetry operators are called a point group. The point group designations follow a sequence of questions to assign a molecule into that point group. The questions are as follows:

- Is the molecule a high symmetry (linear, cubic) point group?

- Does the molecule have a principal rotational axis C_n?

- Does the molecule have any C_2 rotational axes perpendicular to the principal axis?

- Does the molecule have σ_h symmetry?

- Does the molecule have σ_v symmetry?

The answers to these questions determine the symbol describing the point group such as for water, C_{2v}. This means that water has a principal axis of C_2 and at least one vertical mirror

plane (σ_v). For the case of water, it has two vertical mirror planes designated (σ_v) and (σ_v') as shown in Figure 11.
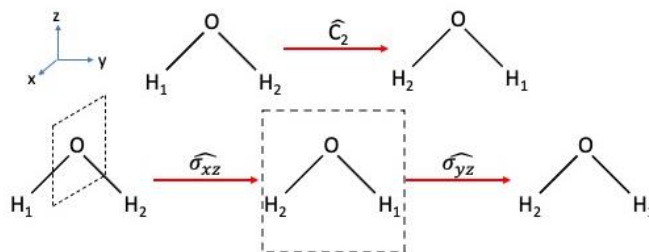
Figure 11: Symmetry Operators of Water (H₂O).

It is necessary to express the different symmetry operators in matrix form as group theory relies on the mechanics of matrices to easily express what is happening to a molecule as it goes through a transformation matrix $D(x)$, where x is whatever symmetry operator being applied. The transformation matrix has the characterization of D because of the German word *darstellung* meaning representation. The transformation needs to generate a new position vector matrix ($\vec{p'}$) from the original position vector matrix ($\vec{p}$) such that

$$\vec{p'} = D(x)\vec{p} \tag{1-70}$$

The different transformation matrices for the symmetry operators of water are shown in based off the definition of the identity operator and Figure 11:

Operator	Transformation Matrix	
Identity ($\hat{E}$)	$D(\hat{E}) = \begin{pmatrix} 1 & 0 & 0 \\ 0 & 1 & 0 \\ 0 & 0 & 1 \end{pmatrix}$	(1-71)
Rotation (C_2)	$D(\widehat{C_2}) = \begin{pmatrix} -1 & 0 & 0 \\ 0 & -1 & 0 \\ 0 & 0 & 1 \end{pmatrix}$	(1-72)
xz-plane Reflection (σ_v)	$D(\widehat{\sigma_v}) = \begin{pmatrix} 1 & 0 & 0 \\ 0 & -1 & 0 \\ 0 & 0 & 1 \end{pmatrix}$	(1-73)
yz-plane Reflection (σ_v')	$D(\widehat{\sigma_v'}) = \begin{pmatrix} -1 & 0 & 0 \\ 0 & 1 & 0 \\ 0 & 0 & 1 \end{pmatrix}$	(1-74)

By using the transformation matrix on a position vector ($\vec{p} = x\hat{i} + y\hat{j} + z\hat{k}$) and applying the transformation matrix, we can write a character table representing all the symmetry operators of the C_{2v} molecule. The values of 1 in the table mean that the specified component did not change signs while a value of -1 means that the component changed signs in relation to its position.

Table 3: Character Integer Values with Respect to x,y, and z for C_{2v} Point Group

C_{2v}	$\hat{E}$	$\widehat{C_2}$	$\widehat{\sigma_v}$	$\widehat{\sigma_v'}$
x	1	-1	1	-1
y	1	-1	-1	1
z	1	1	1	1

The character table for the C_{2v} point group can be related to the Mulliken symbols listed in .

These new symbols will allow us to express different transformations more effectively.

Table 4: Mulliken Symbol Definitions

Symbol	Definition
A	Singly degenerate, symmetric with respect to (w.r.t.) rotation around principal axis C_n
B	Singly degenerate, anti-symmetric w.r.t. rotation around principal axis C_n
E	Doubly degenerate
T	Triply degenerate
subscript 1	Symmetric w.r.t. C_2 perpendicular to C_n, or σ_v if no secondary C_2 axis present
subscript 2	Anti-symmetric w.r.t. C_2 perpendicular to C_n, or σ_v if no secondary C_2 axis present
g	Symmetric w.r.t. to inversion
u	Anti-symmetric w.r.t. to inversion
'	Symmetric w.r.t. σ_h
"	Anti-symmetric w.r.t. σ_h

The terms symmetric mean an unchanged value (1) while anti-symmetric means a changed

value (-1) for the respective coordinates x,y, or z. With these definitions in mind, we can expand

on Table 3 for an irreducible character table for the C_{2v} point group.

Table 5: Irreducible Character Group of C_{2v} molecule with Linear Functions

C_{2v}	$\hat{E}$	$\widehat{C_2}$	$\widehat{\sigma_v}$	$\widehat{\sigma'_v}$	Linear Function
A_1	1	1	1	1	z
A_2	1	1	-1	-1	
B_1	1	-1	1	-1	x
B_2	1	-1	-1	1	y

The assigned linear functions are describing what coordinate the single matrix contains that the

Mulliken symbol defines.

The molecule may instead of going through a symmetry operator transformation, go

through a rotational operator transformation $(\widehat{R_x}, \widehat{R_y}, \widehat{R_z})$. The rotational transformations are

shown in Figure 12 with a secondary model shown looking down the axis that the rotational

transformation acts upon with vectors showing direction of movement for the atoms in the

molecule.
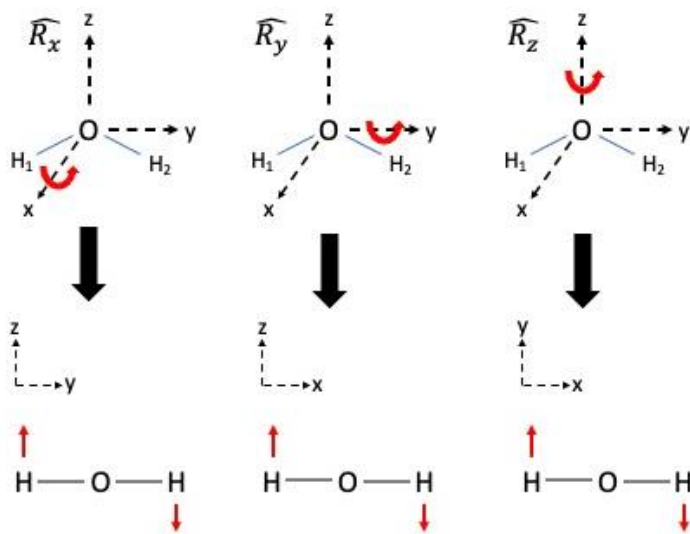
Figure 12: Rotational Operators of Water with Motion Vectors.

The easiest way to define the Mulliken symbols for rotational transformations will be using the movement vectors and then performing a symmetry operator on it to determine if the sign changes for the movement vectors. A change results in a value of (-1) and no change is a value of (1).

Table 6: Character Table for Rotational Transformation of Water

C_{2v}	$\hat{E}$	$\widehat{C_2}$	$\widehat{\sigma_v}$	$\widehat{\sigma_v'}$	Mulliken Symbol
$\widehat{R_x}$	1	-1	-1	1	B_1
$\widehat{R_y}$	1	-1	1	-1	B_2
$\widehat{R_z}$	1	1	-1	-1	A_2

The final family of operators on a molecule are the translational operators ($\widehat{T_x}, \widehat{T_y}, \widehat{T_z}$).

These are the movement of the entire molecule in one direction and can be represented

similarly to the rotational operator movement vectors. For the translational operators though,

movement vectors are applied to the entire molecule.
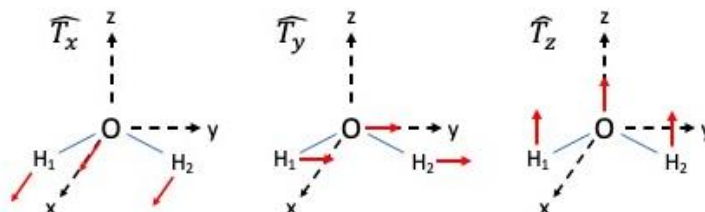
Figure 13: Translational Operators on Water with Movement Vectors

If the translational movement vectors change their direction of movement when the symmetry

operator is applied, then a value of (-1) is recorded; if no change in the direction of the

movement vector is observed, then a value of (1) is applied.

Table 7: Character Table for Translational Transformation of Water

C_{2v}	$\hat{E}$	$\widehat{C_2}$	$\widehat{\sigma_v}$	$\widehat{\sigma_v'}$	Mulliken Symbol
$\widehat{T_x}$	1	-1	1	-1	B_1
$\widehat{T_y}$	1	-1	-1	1	B_2
$\widehat{T_z}$	1	1	1	1	A_1

We have described every degree of freedom that a C_{2v} molecule such as water. To verify this,

we will create a matrix representing all the Cartesian coordinates for the molecule and apply

28

the corresponding symmetry operators. The integer values of the (9x9) symmetry operator

matrices determine what happens to the atom's coordinate in the same way the (3x3)

symmetry operator matrices of Table 2.

Table 8: Atomic Vector Transformation Matrices for C_{2v} Point Group

Operator	Transformation Matrix	
$\hat{E}$	$$\begin{pmatrix} 1 & 0 & 0 & 0 & 0 & 0 & 0 & 0 & 0 \\ 0 & 1 & 0 & 0 & 0 & 0 & 0 & 0 & 0 \\ 0 & 0 & 1 & 0 & 0 & 0 & 0 & 0 & 0 \\ 0 & 0 & 0 & 1 & 0 & 0 & 0 & 0 & 0 \\ 0 & 0 & 0 & 0 & 1 & 0 & 0 & 0 & 0 \\ 0 & 0 & 0 & 0 & 0 & 1 & 0 & 0 & 0 \\ 0 & 0 & 0 & 0 & 0 & 0 & 1 & 0 & 0 \\ 0 & 0 & 0 & 0 & 0 & 0 & 0 & 1 & 0 \\ 0 & 0 & 0 & 0 & 0 & 0 & 0 & 0 & 1 \end{pmatrix}$$	(1-75)
C_2	$$\begin{pmatrix} -1 & 0 & 0 & 0 & 0 & 0 & 0 & 0 & 0 \\ 0 & -1 & 0 & 0 & 0 & 0 & 0 & 0 & 0 \\ 0 & 0 & 1 & 0 & 0 & 0 & 0 & 0 & 0 \\ 0 & 0 & 0 & 0 & 0 & 0 & -1 & 0 & 0 \\ 0 & 0 & 0 & 0 & 0 & 0 & 0 & -1 & 0 \\ 0 & 0 & 0 & 0 & 0 & 0 & 0 & 0 & 1 \\ 0 & 0 & 0 & -1 & 0 & 0 & 0 & 0 & 0 \\ 0 & 0 & 0 & 0 & -1 & 0 & 0 & 0 & 0 \\ 0 & 0 & 0 & 0 & 0 & 1 & 0 & 0 & 0 \end{pmatrix}$$	(1-76)
σ_v	$$\begin{pmatrix} 1 & 0 & 0 & 0 & 0 & 0 & 0 & 0 & 0 \\ 0 & -1 & 0 & 0 & 0 & 0 & 0 & 0 & 0 \\ 0 & 0 & 1 & 0 & 0 & 0 & 0 & 0 & 0 \\ 0 & 0 & 0 & 0 & 0 & 0 & 1 & 0 & 0 \\ 0 & 0 & 0 & 0 & 0 & 0 & 0 & -1 & 0 \\ 0 & 0 & 0 & 0 & 0 & 0 & 0 & 0 & 1 \\ 0 & 0 & 0 & 1 & 0 & 0 & 0 & 0 & 0 \\ 0 & 0 & 0 & 0 & -1 & 0 & 0 & 0 & 0 \\ 0 & 0 & 0 & 0 & 0 & 1 & 0 & 0 & 0 \end{pmatrix}$$	(1-77)

| σ_v' | $\begin{pmatrix} -1 & 0 & 0 & 0 & 0 & 0 & 0 & 0 & 0 \\ 0 & 1 & 0 & 0 & 0 & 0 & 0 & 0 & 0 \\ 0 & 0 & 1 & 0 & 0 & 0 & 0 & 0 & 0 \\ 0 & 0 & 0 & -1 & 0 & 0 & 0 & 0 & 0 \\ 0 & 0 & 0 & 0 & 1 & 0 & 0 & 0 & 0 \\ 0 & 0 & 0 & 0 & 0 & 1 & 0 & 0 & 0 \\ 0 & 0 & 0 & 0 & 0 & 0 & -1 & 0 & 0 \\ 0 & 0 & 0 & 0 & 0 & 0 & 0 & 1 & 0 \\ 0 & 0 & 0 & 0 & 0 & 0 & 0 & 0 & 1 \end{pmatrix}$ | (1-78) |

If we calculate the character (χ) of the individual matrices, we would be able to get a representation of the point group based on the 3n vectors as the basis set (Γ_{3n}). The value of n in the Γ term is the number of atoms inside the molecule, for the C_{2v} point group the value is 3. The character is calculated by summing all the integers along the longest diagonal from left to right. This representation is known as a reducible representation because it is not expressed in non-reducible notation like a Mulliken symbol. The reducible representation then for the C_{2v} molecule with the character integers as values is as follows:

Table 9: Reducible Representation for C_{2v} Point Group

	$\hat{E}$	$\widehat{C_2}$	$\widehat{\sigma_v}$	$\widehat{\sigma_v'}$
Γ_{3n}	9	-1	1	3

We are then able to draw out the irreducible representation for Γ_{3n} as the summation of all the individual irreducible representations of the different types of transformations we did before. To verify this answer though, we will use the reduction formula:

$$a_i = \frac{1}{g}\Sigma(n_R\chi_R\chi_{IR})\tag{1-79}$$

The terms in the reduction formula are:

a_i -   number of times an irreducible representation contributes to the reducible

       representation

g -   total number of symmetry operations for the point group

n_R-   number of operations in the class of operation

χ_R -   character in the reducible representation corresponding to the class of operation

χ_{IR} -   corresponding character in the irreducible representation a_i

I have shown the work of the reducing formula for the irreducible representation A_1 below and

the process for calculating the remaining irreducible representations (A_2, B_1, B_2) is the same.

$$A_1 = \frac{1}{4}[(1 \times 9 \times 1) + (1 \times -1 \times 1) + (1 \times 1 \times 1) + (1 \times 3 \times 1)] = 3\tag{1-80}$$

We end up with the irreducible representation Γ_{3n} for the C_{2v} point group as:

$$\Gamma_{3n} = 3A_1 + 1A_2 + 2B_1 + 3B_2\tag{1-81}$$

This irreducible representation is for every irreducible transformation representation of the C_{2v}

point group but we are only interested in the vibration representations, not the rotational or

translational components found in Table 6 and Table 7 respectively. We take the sum of these

two unwanted components and then subtract it from (1-71).

$$\Gamma_{translation+rotation} = A_1 + A_2 + 2B_1 + 2B_2\tag{1-82}$$

$$\Gamma_{vibration} = 2A_1 + B_2\tag{1-83}$$

These vibrational modes irreducible representations can be determined by drawing vectors showing the vibration movement and then applying the symmetry operators. The C_{2v} point group has two stretching modes, symmetric and asymmetric stretching, and a bending mode as shown below.
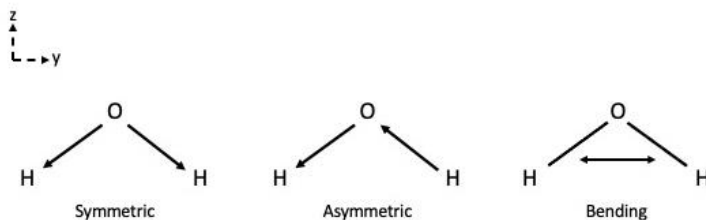
Figure 14: Vibrational Modes of Water with Motion Vectors

This will then allow us to finally designate irreducible representations for each vibrational mode according to the interactions with the symmetry operators:

Table 10: Vibrational Irreducible Representation Character Table of Water

C_{2v}	$\hat{E}$	$\widehat{C_2}$	$\widehat{\sigma_v}$	$\widehat{\sigma_v'}$	Mulliken Symbol
$\Gamma_{\text{O-H symm}}$	1	1	1	1	A_1
$\Gamma_{O\text{-H asymm}}$	1	-1	-1	1	B_2
Γ_{bend}	1	1	1	1	A_1

The final step in determining the if the vibrational modes are Raman active is determining if the mode corresponding to a quadratic function (x^2, y^2, z^2, and xy). The final, full irreducible character table for the C_{2v} point group will shed light into what vibrational modes match up to these quadratic functions.

Table 11: Irreducible Character Table for the C_{2v} Point Group

C_{2v}	$\hat{E}$	$\widehat{C_2}$	$\widehat{\sigma_v}$	$\widehat{\sigma_v'}$	Linear functions	Quadratic Functions
A_1	1	1	1	1	z, T_z	x^2, y^2, z^2
A_2	1	1	-1	-1	R_z	xy
B_1	1	-1	1	-1	x, T_x, R_y	xz
B_2	1	-1	-1	1	y, T_y, R_x	yz

From looking at the column of quadratic functions, we can see that the A_1 and B_2 vibrational modes are Raman active. There are irreducible character tables generated for every point group available for reference in every book on Group Theory and the respective linear or quadratic functions to determine if a vibrational mode is Raman active. An important note is that Raman spectra reference guides will note if a specific vibrational mode is polarized or depolarized. This is determined by have a plane-polarized incident light strike the molecule and if the scattered light remains polarized in the plane, then the mode is polarized. Conversely, if the scattered light becomes depolarized, the mode is deemed depolarized.

1.4 Surface Enhanced Raman Spectroscopy

The Raman effect can be significantly amplified with the use of appropriate roughened surfaces. This amplified effect was first shown by Fleischman et al in 1974 [7] with the analysis of pyridine on a roughened silver electrode. The group assumed it was due to the enhanced surface area provided by the roughening of the electrode but an explanation for the actual phenomenon was put forth by Albrecht and Creighton in 1977 [8]. They introduced the theory of the interaction of the adsorbed molecules on the roughened silver electrodes with the surface plasmons generated on the electrodes and the increased Raman cross-sections as explanations behind the increased Raman spectrum. This field of Raman spectroscopy became creatively known as Surface-Enhanced Raman Spectroscopy (SERS). The typical surfaces for SERS are silver (Ag), gold (Au), or copper (Cu) that are roughened or for modern setups, nanoparticles of differing geometries.

There are two theoretical systems that explain the enhanced signal, the chemical and electromagnetic theories for SERS systems. To begin the explanation of the two sources of signal enhancement found in SERS, we must first introduce the surface plasmon polariton (SPP).

1.4.1 Surface Plasmon Polaritons

The first step in the definition of a surface plasmon polariton, also known as a surface plasmon, is the definition of a plasmon. A plasmon or volume plasmon is the oscillation of the electron cloud around the positive nucleus. For metals and heavily doped semiconductors, these clouds are the collection of loosely bound valence electrons. The oscillating clouds have a peak amplitude at the plasma frequency (ω_p) defined in Appendix D as:

$$\omega_p = \sqrt{\frac{Ne^2}{m^*\epsilon_0}} \tag{1-84}$$

If the incident light frequency is below the plasma frequency, the metal reflects the light. For

incident frequencies above the plasma frequency, the light is transmitted through the electron

clouds. The incident light can also be absorbed and at the metal's plasma frequency, the

absorbance is highest which is expressed in the maximum amplitude of the oscillating electron

cloud.

If we confine the plasma oscillations to just the electron charges along the boundary of

the metal, then we have created a surface plasmon (SP) or a surface plasmon polariton (SPP).

The mathematical description for the surface plasmon begins with the curl equations from

Maxwell's equations with no external charge or current densities

$$\nabla \times \vec{E} = -\frac{\partial \vec{B}}{\partial t} \tag{1-85}$$

$$\nabla \times \vec{H} = \frac{\partial \vec{D}}{\partial t} \tag{1-86}$$

Using the substitutions for the definition of $\vec{D}$ and $\vec{B}$ for a linearly polarized, isotropic, and non-

magnetic media($\mu = 0$)

$$\vec{D} = \epsilon_0 \epsilon \vec{E} \tag{1-87}$$

$$\vec{B} = \mu_0 \vec{H} \tag{1-88}$$

We can rewrite the Maxwell equations

$$\nabla \times \vec{E} = -\mu_0 \frac{\partial \vec{H}}{\partial t} \tag{1-89}$$

$$\nabla \times \vec{H} = \epsilon_0 \epsilon \frac{\partial \vec{\mathrm{E}}}{\partial \mathrm{t}} \tag{1-90}$$

With these new definitions, we take the curl of (1-89) and relate that to (1-90)

$$\nabla \times \nabla \times \vec{E} = \nabla \times \left(-\mu_0 \frac{\partial \vec{H}}{\partial t} \right) \tag{1-91}$$

$$\nabla \times \nabla \times \vec{E} = -\mu_0 \epsilon_0 \epsilon \frac{\partial^2 \vec{E}}{\partial t^2} \tag{1-92}$$

Now with the curl identity

$$\nabla \times \nabla \times \vec{E} = \nabla(\nabla \cdot \vec{E}) - \nabla^2 \vec{E} \tag{1-93}$$

Since our electric field is going through a material with the permittivity of ϵ, we need to use the divergence identity for the modified electric field term $(\epsilon\vec{E})$

$$\nabla \cdot \left(\epsilon\vec{\mathrm{E}} \right) = \vec{\mathrm{E}} \cdot \nabla\epsilon + \epsilon\nabla \cdot \vec{\mathrm{E}} \tag{1-94}$$

If we recognize that the permittivity of the medium does not vary as it is isotropic and that the system has no external charge density ($\nabla \cdot \vec{E} = 0$), then (1-94) equals 0 and allows (1-92) and (1-93) to be written as

$$\nabla^2\vec{E} - \mu_0\epsilon_0\epsilon \frac{\partial^2 \vec{\mathrm{E}}}{\partial t^2} = 0 \tag{1-95}$$

Using the definition of the speed of light (c) with respect to the permittivity of free space (ϵ_0) and the permeability of free space (μ_0)

$$c = \frac{1}{\sqrt{\epsilon_0\mu_0}} \tag{1-96}$$

We can rewrite (1-95) to become the wave equation:

$$\nabla^2\vec{E} - \frac{\epsilon}{c^2}\frac{\partial^2\vec{E}}{\partial t^2} = 0 \qquad (1\text{-}97)$$

By setting up the system to having an EM wave with electric field propagation only in the x-direction and the only variation in the permittivity of the system in the z-direction as shown in Figure 15, We can create the Helmholtz equation from (1-97) by assuming that the EM-wave has a harmonic time dependence and so the electric field can be written as $(\vec{E}(\vec{r}, t) = \vec{E}(\vec{r})e^{-i\omega t})$

$$\nabla^2\vec{E} - \frac{\epsilon}{c^2}\frac{\partial^2\vec{E}(\vec{r})e^{-i\omega t}}{\partial t^2} = 0 \qquad (1\text{-}98)$$

$$\nabla^2\vec{E} + \frac{\epsilon\omega^2}{c^2}\vec{E} = 0 \qquad (1\text{-}99)$$

Final step to make this into the Helmholtz equation is to use the definition of the wavevector (k_0) to rewrite (1-99)

$$k_0 = \frac{\omega}{c} \qquad (1\text{-}100)$$

$$\nabla^2\vec{E} + k_0^2\epsilon\vec{E} = 0 \qquad (1\text{-}101)$$
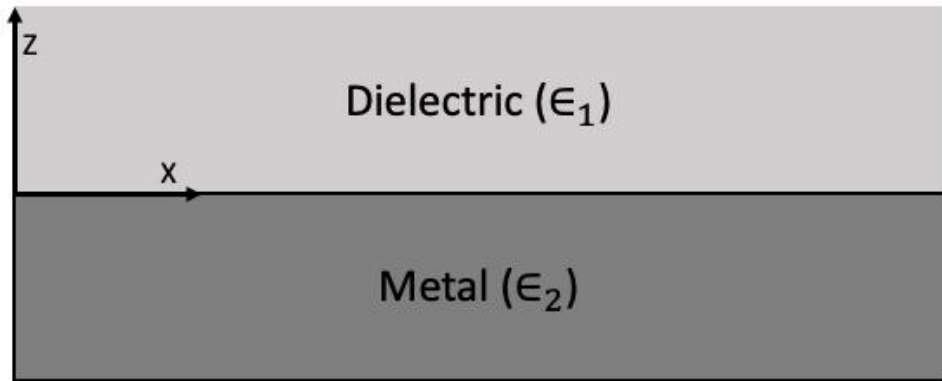
Figure 15: Surface Plasmon Propagation Geometry for Metal/Dielectric System. The electric field propagates along the x-axis and has an evanescent propagation in the z-direction.

Now that the time dependence is taken care of, the next step is to account for the physical propagation of the wave in the x-direction in addition to a plane at $z = 0$. The electric field with respect to the surface is $\vec{E}(x, y, z) = \vec{E}(z)e^{i\beta x}$ and the term β is a complex parameter called the propagation constant that is the wave vector component in the direction of propagation. If we focus on the $\nabla^2 \vec{E}$ term and plug in the electric field equation for the surface, we can create the full wave equation

$$\nabla^2 \vec{E} = \nabla^2 \left(\vec{E}(z)e^{i\beta x} \right) \tag{1-102}$$

$$\nabla^2 \left(\vec{E}(z)e^{i\beta x} \right) = \frac{\partial^2 \left(\vec{E}(z)e^{i\beta x} \right)}{\partial z^2} - \beta^2 \vec{E}(z)e^{i\beta x} \tag{1-103}$$

$$-\beta^2 \vec{E}(z)e^{i\beta x} = \frac{\partial^2 \vec{E}}{\partial z^2} - \beta^2 \vec{E} \tag{1-104}$$

Plugging (1-94) back into (1-91) gives

$$\frac{\partial^2 \vec{E}}{\partial z^2} + (k_0^2 \epsilon - \beta)\vec{E} = 0 \tag{1-105}$$

For the magnetic field, the same process is undertaken resulting in an equation with the substitutions for the magnetic field. We now need to perform the mathematical functions described in (1-89) and (1-90) to get the coupled equations between the magnetic-field and the electric-field for the respective cartesian components in the system. The curl operator has the known solution

$$\nabla \times \vec{F} = \left(\frac{\partial F_z}{\partial y} - \frac{\partial F_y}{\partial z} \right)\hat{\imath} + \left(\frac{\partial F_x}{\partial z} - \frac{\partial F_z}{\partial x} \right)\hat{\jmath} + \left(\frac{\partial F_y}{\partial x} - \frac{\partial F_x}{\partial y} \right)\hat{k} \tag{1-106}$$

Using the curl operator solution in (1-89) and (1-90) with the further definition that with a harmonic time dependence the partial with respect to time is $\frac{\partial}{\partial t} = -i\omega$, we can write out the

38

individual Cartesian component equivalencies for the electric and magnetic fields for our

surface wave

$$\left(\frac{\partial E_z}{\partial y} - \frac{\partial E_y}{\partial z}\right) = i\omega\mu_0 H_x \qquad \text{(1-107)}$$

$$\left(\frac{\partial E_x}{\partial z} - \frac{\partial E_z}{\partial x}\right) = i\omega\mu_0 H_y \qquad \text{(1-108)}$$

$$\left(\frac{\partial E_y}{\partial x} - \frac{\partial E_x}{\partial y}\right) = i\omega\mu_0 H_z \qquad \text{(1-109)}$$

$$\left(\frac{\partial H_z}{\partial y} - \frac{\partial H_y}{\partial z}\right) = -i\omega\epsilon_0\epsilon E_x \qquad \text{(1-110)}$$

$$\left(\frac{\partial H_x}{\partial z} - \frac{\partial H_z}{\partial x}\right) = -i\omega\epsilon_0\epsilon E_y \qquad \text{(1-111)}$$

$$\left(\frac{\partial H_y}{\partial x} - \frac{\partial H_x}{\partial y}\right) = -i\omega\epsilon_0\epsilon E_z \qquad \text{(1-112)}$$

These terms can be reduced if we note that because there is no change for the electric or

magnetic fields in the y-axis, then $\frac{\partial}{\partial y} = 0$. It can be further reduced since the propagation is in

the x-direction so the partial derivative term $\frac{\partial}{\partial x} = -i\beta$.

$$\frac{\partial E_y}{\partial z} = -i\omega\mu_0 H_x \qquad \text{(1-113)}$$

$$\frac{\partial E_x}{\partial z} - i\beta E_z = i\omega\mu_0 H_y \qquad \text{(1-114)}$$

$$i\beta E_y = i\omega\mu_0 H_z \qquad \text{(1-115)}$$

$$\frac{\partial H_y}{\partial z} = i\omega\epsilon_0\epsilon E_x \qquad \text{(1-116)}$$

$$\frac{\partial H_x}{\partial z} - i\beta H_z = -i\omega\epsilon_0\epsilon E_y \qquad (1\text{-}117)$$

$$i\beta H_y = -i\omega\epsilon_0\epsilon E_z \qquad (1\text{-}118)$$

The components have two separate set of solutions, one for a transverse magnetic-field (TM) mode and one for a transverse electric-field (TE) mode. In a TM mode, there is no magnetic field component in the direction of the wave propagation. The non-zero components for this mode are E_x, E_z, and H_y. The coupled equations then for the TM mode are

$$E_x = -\frac{i}{\omega\epsilon_0\epsilon}\frac{\partial H_y}{\partial z} \qquad (1\text{-}119)$$

$$E_z = -\frac{\beta}{\omega\epsilon_0\epsilon}H_y \qquad (1\text{-}120)$$

The wave equation for the TM modes then is the wave equation with the only non-zero magnetic field (H_y)

$$\frac{\partial^2 H_y}{\partial t^2} + (k_0^2\epsilon - \beta^2)H_y = 0 \qquad (1\text{-}121)$$

The logic for a TE wave is the same with the non-zero components being H_x, H_z, and E_y. The corresponding coupled equations then are

$$H_x = \frac{i}{\omega\epsilon_0\epsilon}\frac{\partial E_y}{\partial z} \qquad (1\text{-}122)$$

$$H_z = \frac{\beta}{\omega\mu_0}E_y \qquad (1\text{-}123)$$

The wave equation for TE modes is then

$$\frac{\partial^2 E_y}{\partial t^2} - (k_0^2\epsilon - \beta^2)E_y = 0 \qquad (1\text{-}124)$$

40

Now that we have determined the wave equation for waves propagating on the surface

between two interfaces of differing permittivity, we move on to applying these equations with

boundary conditions. Surface plasmons require metals or heavily doped semiconductors that

functionally are metals and both types of surfaces have a real dielectric value below 0, $Re[\epsilon_1] <$

0. This condition is only satisfied at frequencies below the bulk plasma frequency.

In our surface plasmon setup from before, the wave solutions needed to decay in the z-

direction away from the surface ($z = 0$). These types of waves are called evanescent waves and

we will work with the TM mode solutions so that the electric field has a decaying z-component

to the electric field.
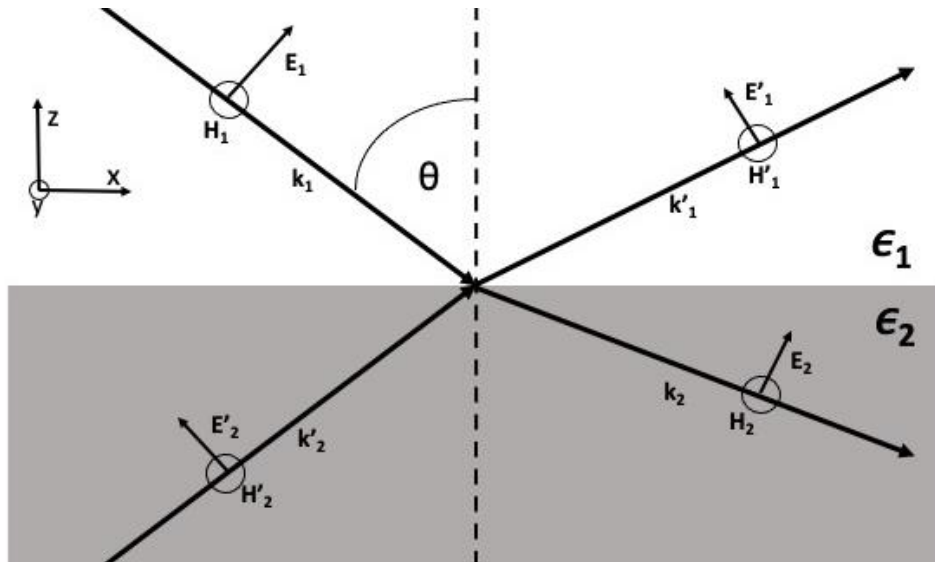
Figure 16: Propagating (k_x) Transverse Magnetic Field Electromagnetic Wave. The electromagnetic wave has no magnetic field

components in the x or z-direction and conversely no electric field component in the y-direction in the TM-mode solutions. The

dielectric permittivity (ϵ_1) is assumed to be non-absorbing and the surface with dielectric permittivity (ϵ_2) is assumed to be a

metal for the appearance of propagating surface plasmons.

The TM mode solutions can be applied to two different areas, $z > 0$ and $z < 0$ as shown in

Figure 16. For the first area, $z > 0$, the solutions are

$$H_y(z) = A_2 e^{i\beta x} e^{-k_2 z} \qquad (1\text{-}125)$$

$$E_x(z) = iA_2 \frac{1}{\omega \epsilon_0 \epsilon_2} k_2 e^{i\beta x} e^{-k_2 z} \qquad (1\text{-}126)$$

$$E_z(z) = -A_1 \frac{\beta}{\omega \epsilon_0 \epsilon_2} e^{i\beta x} e^{-k_2 z} \qquad (1\text{-}127)$$

The wavevector (k) of these solutions have a negative value so that as $z \to +\infty$, the electric

field decays. For the solutions where $z < 0$, the wavevectors will have a positive value. This

means that as $z \to -\infty$, the electric-field in the z-direction decays from the maximum at the

surface $(z = 0)$. The TM mode solutions for $z < 0$ follows the same logic as above

$$H_y(z) = A_1 e^{i\beta x} e^{k_1 z} \qquad (1\text{-}128)$$

$$E_x(z) = -iA_1 \frac{1}{\omega \epsilon_0 \epsilon_1} k_1 e^{i\beta x} e^{k_1 z} \qquad (1\text{-}129)$$

$$E_z(z) = -A_1 \frac{\beta}{\omega \epsilon_0 \epsilon_1} e^{i\beta x} e^{k_1 z} \qquad (1\text{-}130)$$

The necessary continuity of H_y and ϵE_z at the surface requires $A_1 = A_2$ and the z-component

wavevectors to have the following relationship

$$\frac{k_2}{k_1} = -\frac{\epsilon_2}{\epsilon_1} \qquad (1\text{-}131)$$

This leads to the dispersion relation for surface plasmons once the wave equation is applied to

H_y. A more detailed derivation for the dispersion relation is included in Appendix G but for

now, the dispersion relation is

$$\beta = k_0 \sqrt{\frac{\epsilon_1 \epsilon_2}{\epsilon_1 + \epsilon_2}} \qquad (1\text{-}132)$$

The logic for TM modes can be applied to TE modes but the continuity requirements force $A_1 = A_2 = 0$ for TE polarization. This means there are no surface plasmons for TE polarized incident light.

In the dispersion relation (1-132) for the system shown in Figure 15, we can assume that the permittivity of the metal (ϵ_2) with regards to the frequency of incident light is a complex function, $\epsilon_2(\omega) = \epsilon_2'(\omega) + i\epsilon_2''(\omega)$. The complex permittivity is defined by the Drude Model which is derived in Appendix D.

$$\epsilon_2(\omega) = 1 - \frac{\omega_p^2 \tau^2}{1 + \omega^2 \tau^2} + i \frac{\omega_p^2 \tau}{\omega(1 + \omega^2 \tau^2)} \qquad (1\text{-}133)$$

The dispersion relation in (1-132) works for both complex and real permittivity but to approximate the surface plasmon frequency, we are going to assume no absorption. This means that $\epsilon_2'' = 0$ and an additional assumption is that the surface plasmon frequency is at a frequency significantly higher than the relaxation time (τ), allowing the real component of the metal surface permittivity to be approximated as

$$\epsilon_2'(\omega) = 1 - \frac{\omega_p^2}{\omega^2} \qquad (1\text{-}134)$$

Plugging this value back into the dispersion equation results in a surface plasmon frequency (ω_s) to be derived

$$k_s = k_0 \sqrt{\frac{\epsilon_1 \epsilon_2}{\epsilon_1 + \epsilon_2}} \qquad (1\text{-}135)$$

$$k_s = k_0 \sqrt{\frac{\left(1 - \frac{\omega_p^2}{\omega^2}\right)\epsilon_1}{\left(1 - \frac{\omega_p^2}{\omega^2}\right) + \epsilon_1}} \qquad (1\text{-}136)$$

This equation has a wavevector of zero where $\omega_p^2 = \omega^2$ and an asymptote at $\left(1 - \frac{\omega_p^2}{\omega^2}\right) = -\epsilon_1$.

We will focus on the asymptote as the zero occurs at the bulk plasma frequency and the

asymptote condition is the surface plasmon frequency.

$$1 - \frac{\omega_p^2}{\omega^2} = -\epsilon_1 \qquad (1\text{-}137)$$

$$1 + \epsilon_1 = \frac{\omega_p^2}{\omega^2} \qquad (1\text{-}138)$$

$$\omega_s = \frac{\omega_p}{\sqrt{1 + \epsilon_1}} \qquad (1\text{-}139)$$

The surface plasmon frequency can be reduced if the metal surface is in vacuum/air to

$\omega_s = \frac{\omega_p}{\sqrt{2}}$. The surface plasmon will not be radiative because from (1-136), we can see that the

wavenumber of the surface plasmon will always be larger than the incident light wavenumber.

There is no way to conserve the momentum of the light from the surface plasmon in the

current state during the transition to a photon for a smooth surface.

If the system is changed from a smooth, metal surface to a metal surface with a grating

constant (a) then the wavevector of the incident light can be increased by a factor of $m\frac{2\pi}{a}$

where m is an integer. The light is incident at an angle (θ_0) and the x-component wavevector

can be expressed as

$$k_x = k_0 sin(\theta_0) \pm m \frac{2\pi}{a} \qquad (1\text{-}140)$$

This new modified wavevector can then be equated to the wavevector of the surface plasmon with the dielectric medium having a value of 1

$$k_x = k_0 sin(\theta_0) \pm m \frac{2\pi}{a} = k_0 \sqrt{\frac{\epsilon_m}{\epsilon_m + 1}} = k_s \qquad (1\text{-}141)$$

This equivalency importantly allows for the incident light to excite the surface plasmons as well as allows the surface plasmons to propagate into the dielectric medium as emitted light. The coupled plasmon-photon in this grating system can be tuned to specific frequencies or angles. The grating can be thought of as a periodic, ordered roughness but if the roughness is random, like in collections of nanoparticles, then the surface can be approximated as having any required integer value needed to induce coupling.

Before going into the localization of surface plasmons, it is necessary to discuss the amplification of the electric fields of the incident light by the non-radiative surface plasmons. We continue with the previous nomenclature from Figure 15 with the electric field of the dielectric ($\vec{E}_1$) and the electric field of the metal surface ($\vec{E}_2$). The relation between the perpendicular and parallel components of the electric field intensities can be expressed using their relation to the respective wavevectors and refractive indices at the interface of the two mediums ($z = 0$)

$$\frac{\left|\vec{E}_1^{\perp}(0)\right|^2}{\left|\vec{E}_1^{\parallel}(0)\right|^2} = \frac{|k_x|^2}{|k_{z1}|^2} = \frac{|n_\perp|^2}{n_\parallel^2} = \frac{|\epsilon_2|}{\epsilon_1} \qquad (1\text{-}142)$$

$$\frac{\left|\vec{E}_2^{\perp}(0)\right|^2}{\left|\vec{E}_2^{\parallel}(0)\right|^2} = \frac{|k_x|^2}{|k_{z2}|^2} = \frac{|n_{\perp}|^2}{n_{\parallel}^2} = \frac{\epsilon_1}{|\epsilon_2|}$$ (1-143)

The condition of $z = 0$ and the continuity of the electric fields through the setup requires the

equivalency

$$\vec{E}_1^{\parallel}(0) = \vec{E}_2^{\parallel}(0)$$ (1-144)

The total electric field intensity in either medium then is the summation of the perpendicular

and parallel components

$$\frac{\left|\vec{E_1}(0)\right|^2}{\left|\vec{E_2}(0)\right|^2} = \frac{\left|\vec{E_1^{\perp}}(0)\right|^2 + \left|\vec{E_1^{\parallel}}(0)\right|^2}{\left|\vec{E_2^{\perp}}(0)\right|^2 + \left|\vec{E_2^{\parallel}}(0)\right|^2} = \frac{|\epsilon_2|}{\epsilon_1}$$ (1-145)

If we consider that for the incident EM-wave to induce a SP, then $|\epsilon_2| \gg \epsilon_1$. This means that

most of the electric field inside the metal is parallel to the surface from (1-143) and most of the

electric field outside the metal is perpendicular to the surface (1-142). Additionally, the external

electric field is significantly higher (1-145).

Now that the electric field distribution between inside the metal surface and outside the

surface is explained, we move to show the energy contained in the respective electric fields.

The ratio between the power of the incident electric field (P_{inc}) compared to the power

absorbed by the SP (P_{abs}) is defined as the coupling efficiency (η). The power absorbed by the

metal surface with a given surface size (S) is

$$P_{abs} = \int_0^{\infty} \frac{1}{2} \omega \epsilon_0 \, \epsilon_2'' \left|\vec{E}_2(z)\right|^2 S dz$$ (1-146)

$$P_{abs} = S \frac{\epsilon_0 \epsilon_2''}{2} \omega L_{z2} \left|\vec{E}_2(0)\right|^2$$ (1-147)

Using the definition of the wavevector in free space (1-100), we can rewrite the above, enabling

further reduction later in the coupling efficiency equation. The substitution yields

$$P_{abs} = S \frac{\epsilon_0 \epsilon_2''}{2} c k_0 L_{z2} \left| \vec{E}_2(0) \right|^2 \tag{1-148}$$

Where skin depth (L_{z2}) is the distance that the incident wave penetrates the metal surface and

is defined as

$$L = \frac{1}{2k''} \tag{1-149}$$

The power of the incident electric field with incident angle (θ_{inc}) on the surface is similarly

defined as

$$P_{inc} = S \frac{\epsilon_0 c}{2} \sqrt{\epsilon_1} \left(\left| \vec{E}_0 \right|^2 \right) cos(\theta_{inc}) \tag{1-150}$$

We can use the coupling efficiency relationship to determine an intensity relationship of the

electric field inside the metal.

$$\eta = \frac{P_{abs}}{P_{inc}} = \frac{I_2}{I_0} \tag{1-151}$$

$$\frac{\left| \vec{E}_2(0) \right|^2}{\left| \vec{E}_{inc} \right|^2} = \frac{\eta \sqrt{\epsilon_1} cos(\theta_{inc})}{\epsilon_2'' k_0 L_{z2}} = \frac{I_2}{I_0} \tag{1-152}$$

To determine the intensity relationship outside the metal surface, we use the electric field

intensity relationship given by (1-145) and substitute this value into (1-152)

$$\frac{\left| \vec{E}_2(0) \right|^2}{\left| \vec{E}_{inc} \right|^2} = \frac{\eta \sqrt{\epsilon_1} cos(\theta_{inc})}{\epsilon_2'' k_0 L_{z2}} \frac{|\epsilon_2|}{\epsilon_1} = \frac{I_1}{I_0} \tag{1-153}$$

The intensities of the absorbed electric fields are both localized very close to the surface of the

metal surface defined previously by the skin depth and are usually in the range of 10's of

nanometers.

Finally, the localization of surface plasmons on metal nanoparticles builds on the

previous SP work. The generalized localized surface plasmon (LSP) derivation utilizes a metal

sphere of permittivity (ϵ_2) in a dielectric medium (ϵ_1) with a diameter much smaller than the

incident light wavelength ($d \ll \lambda$). Solving the Laplace equation for this setup, as shown in

Appendix D, results in a polarization dependence of

$$\alpha = 4\pi a^3 \frac{\epsilon_2 - \epsilon_1}{\epsilon_2 + 2\epsilon_1} \tag{1-154}$$

The permittivity of the metal is a complex value, and the polarization has a maximum value as

the real component of the metal approaches $-2\epsilon_1$. The LSP modes are all radiative as the

curved surface allows the coupling of the LSP's to photons similarly to the SP's on roughened

surfaces. Using the solution for the external electric field of the polarized metal sphere, we can

say that the electric field on the surface of the sphere is

$$E(a) = 2\frac{\epsilon_2 - \epsilon_1}{\epsilon_2 + 2\epsilon_1} E_0 + E_0 \tag{1-155}$$

$$E(a) = \frac{3\epsilon_2}{\epsilon_2 + 2\epsilon_1} E_0 \tag{1-156}$$

 If we use the condition of $\epsilon_2' = -2\epsilon_1$, we can then determine the maximum electric field value

$$E(a) = \frac{3\epsilon_2}{\epsilon_2''} E_0 \tag{1-157}$$

Then the electric field intensity ratio from the localized surface plasmon is just the absolute

value of the square of (1-157)

$$I_{LSP} = \left| \frac{3\epsilon_2}{\epsilon_2''} \right| |E_0|^2 \tag{1-158}$$

The smaller the absorption factor (ϵ_2'') is for a metal, the larger the amplification of the incident

electric field by the nanoparticles. The local enhancement factor due to the localized surface

plasmon then is a ratio of the incident intensity and I_{LSP}

$$F_{LSP} = \frac{I_{LSP}}{I_0} = \frac{|E(a)|^2}{|E_0|^2} \tag{1-159}$$

1.4.2 Electrical Enhancement

The enhancement factor of SERS, in a properly devised setup, is dominated by the

electromagnetic enhancement of the nanoparticle assemblies. In the simplest terms, the SERS

enhancement factor has two sources, the amplification of the local electric field intensity by

LSP's and the enhancement of the emitted radiation by the metal nanoparticle. The amplified

local electric field intensity enhancement factor was previously determined in (1-159). The

enhancement of the emitted radiation by the metal nanoparticle follows a similar ratio of

$$F_R = \frac{I_R}{I_0} = \frac{|E_R|^2}{|E_0|^2} \tag{1-160}$$

The SERS enhancement factor then is simply the product of both enhancement factors

multiplied as it accounts for both the LSP enhancement and the re-emitted radiation

enhancement

$$F_{SERS} = \frac{|E_R|^2}{|E_0|^2} \cdot \frac{|E_{LSP}|^2}{|E_0|^2} \tag{1-161}$$

The final approximation for the SERS enhancement effect relies on the frequency of the

incident light and the Raman-shifted light being close to each other allowing $E_r \approx E_{LSP}$ and

thus

$$F_{SERS} = \frac{|E_{LSP}|^4}{|E_0|^4} \qquad (1\text{-}162)$$

1.4.3   Chemical Enhancement

Researchers still debate the existence of a chemical enhancement effect in the

amplification of the Raman signal in SERS. The chemical enhancement, also known as the

charge-transfer mechanism, essentially is the changing of the polarization factor of a SERS

system by the adsorption of different analytes to the nanoparticle assemblies. The polarization

can be changed by an incomplete binding of the analyte to the nanoparticles usually seen in

similarly charged molecules to the nanoparticles. A second pathway to changing the

polarization factor is if the molecular energy levels of the analyte overlap with the nanoparticle

energy levels. The final pathway for chemical enhancement is like the one above and involves

the matching of the Fermi energy level between the laser and the highest occupied molecular

orbital or the lowest unoccupied molecular orbital of the modified metal/analyte energy levels.

1.4.4   Metal Selection

Now that the sources of signal enhancement and the idea of surface plasmons were

explained, the final step in using SERS is to determine the metal that the surfaces will be

composed of. The typical SERS material are termed the coinage metals; Silver (Ag), Gold (Au)

and Copper (Cu). They all have their advantages and disadvantages, but the primary two metals

used are gold and silver. Copper is generally not used because of its high reactivity to

environmental conditions, the toxicity of copper nanoparticles, and limited effective excitation range compared to silver or gold.

The first parameter of the metal selection process is dependent on the wavelength of light that is used in the experiment. To generate a surface plasmon and thus an enhancement in the Raman signal, the metal must be strongly absorbing for the chosen wavelength. There are overlaps in the absorbance spectrum for the three coinage metals in the range of UV light to IR. If we consider metal films where there is no transmission of light, the breakdown of reflected (R) vs absorbed (A) light can be written as

$$100\% = R + A \tag{1-163}$$

It is easy to see that the absorbed light is just $100\% - R$ so if we use the optical constants from Christy & Johnson [9] listed in Appendix E and the definition of reflectivity with respect to the real refractive index (n) and the extinction coefficient (κ):

$$R = \frac{(n-1)^2 + \kappa^2}{(n+1)^2 + \kappa^2} \tag{1-164}$$

It is possible to graph the reflectivity value and gain an understanding of where the absorption peaks are for the noble metal films, i.e., where the reflectivity has the lowest value.
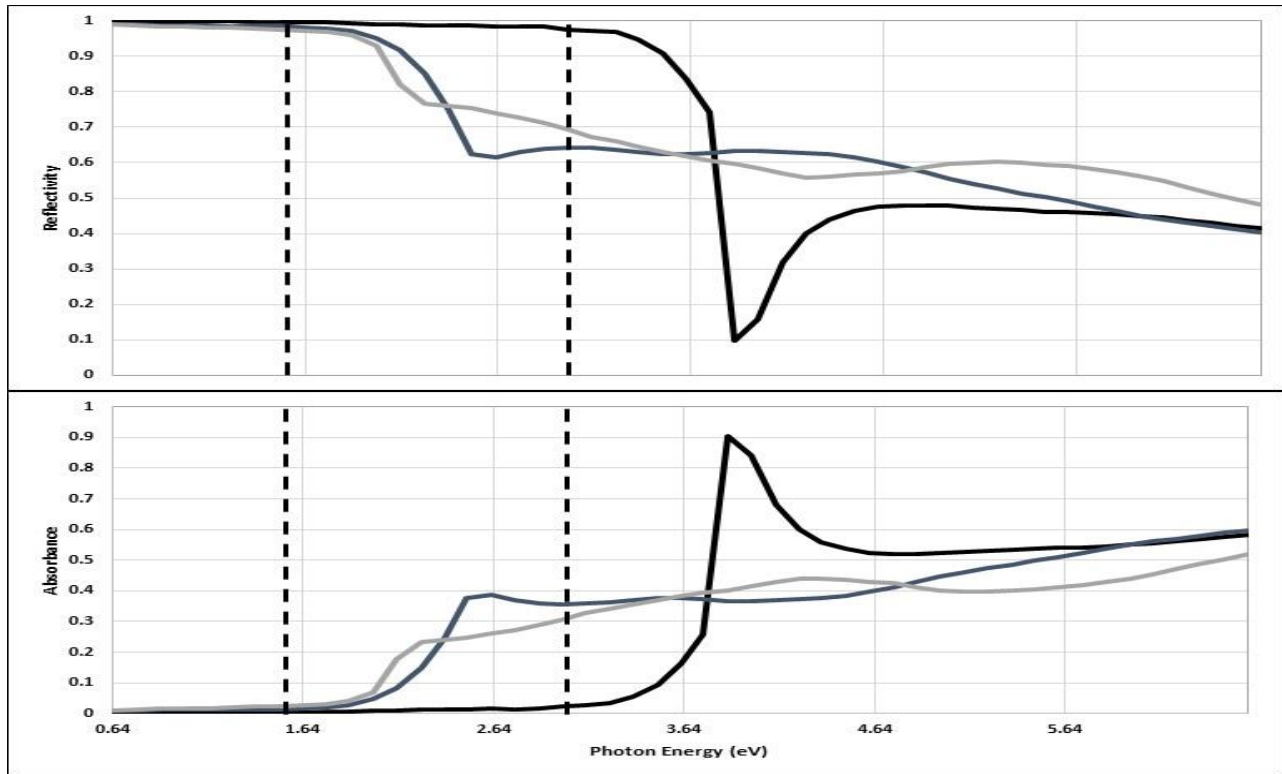
Figure 17: Reflectivity and Absorbance of Noble Metals. Reflectivity (top) and Absorbance (bottom) with respect to photon energy (eV) of Silver (Black), Gold (Navy), and Copper (Silver) films. Note the lack of absorbance for Silver in the visible range compared (area between dashed lines) to Gold and Copper.

The absorbance of bulk silver films is almost zero in the visible light range in Figure 17 while gold shows an absorbance peak around 2.63eV or 471nm. This broad absorption of blue light is the reason that gold has its coloring, a high reflection of yellow/green light. Gold appears to be the superior plasmonic surface in the bulk state like a smooth film but the plasmonic response for a metal can be changed by modifying the size of the surface.

In the size regime where $\lambda \gg r$, with r being the radius of a particle, it is possible to cause a redshift of the plasmonic response. By tailoring the size of the nanoparticles, it is possible to change the LSPR to overlap the wavelength of the incident light.
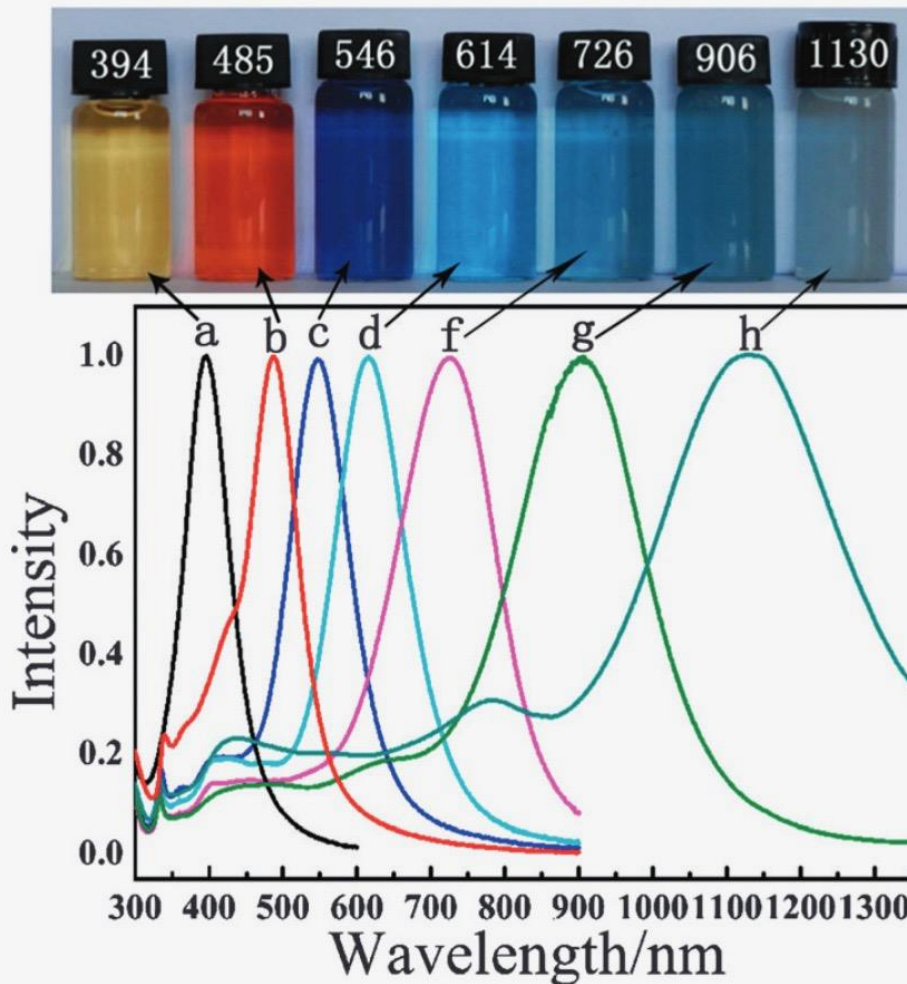
Figure 18: UV-Vis Comparison of Absorption Spectra for Ag Nanoparticles of Varying Sizes. The nanoparticles are first created from the reaction of a Ag-seed solution (a) with Silver Nitrate (AgNO₃), Ascorbic Acid (AA), and Sodium Citrate to produce nanoplates ranging from 25nm (b) to 200nm (h). The intensity listed is the absorption intensity of the incident light [10].

Since the bulk plasmonic response redshifts with regards to the increasing size of the nanoparticles, the respective metal choices for the nanoparticles must account for the incident wavelength. The wavelength of the setup in the lab is 532nm meaning that the choice of metal must have a bulk SPR that is a shorter wavelength than the laser to match the redshifted nanoparticle LSPR size to the laser wavelength. By looking at the absorption spectra of the

noble metals with respect to wavelength for copper [11,12], gold [13–16], and silver [17–20], we can see that silver is the best metal for both SERS and later on, TERS, for the setup using a 532nm laser.
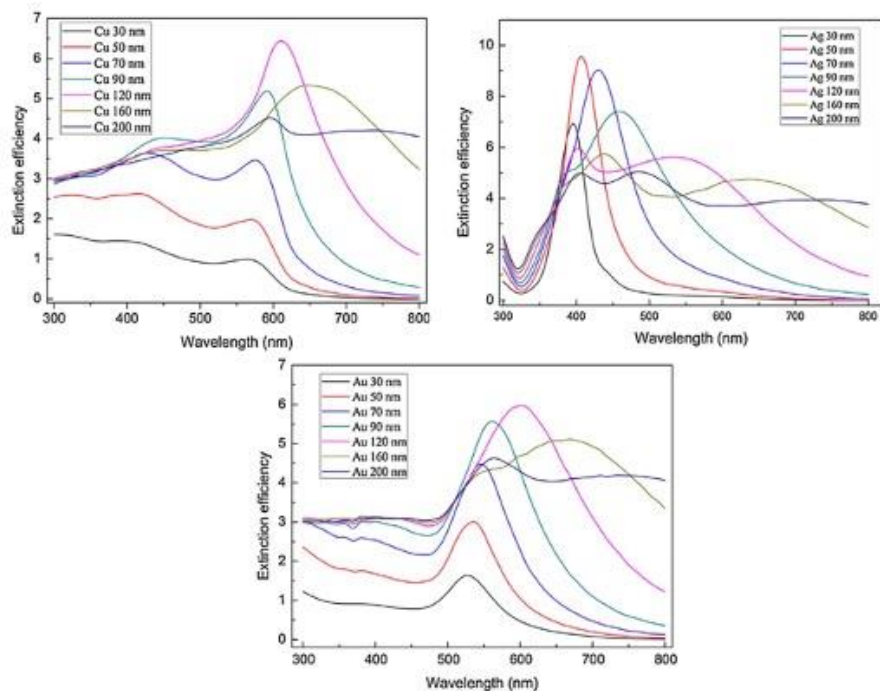
Figure 19: Extinction Efficiency Comparison of Copper, Gold, and Silver Nanoparticles of Various Diameters. The extinction efficiency is the ratio of the summation of the scattering and absorption cross-sections with the geometrical coefficient of the specific sized nanoparticle. Copper (top left) shows a high extinction efficiency around from 400-600nm, Gold (Bottom) shows a high extinction efficiency from 550-800nm, and Silver (top right) shows a higher extinction efficiency from 400-550nm than both Copper and Gold.

1.5   Tip-Enhanced Raman Spectroscopy

The idea of Tip-Enhanced Raman Spectroscopy (TERS) is built upon SERS. Definitionally, TERS is a SERS setup with a reduced amplification area compared to the area illuminated by the laser. The reduced area is generally the etched tips of wires or coated AFM probes brought into the near field as shown in Figure 20. The tip functions like an antenna for the incident field and

54

generates an extremely confined, amplified electric field. The very confined and localized amplified electric field allows researchers to observe forbidden optical modes [21–23] as well as determine the thickness of thin films or probe defects in thin films such as graphene [24–28]. The TERS setup most importantly, allows for the repositioning of the tip and the targeting of specific points on a surface at the sub-micron level.
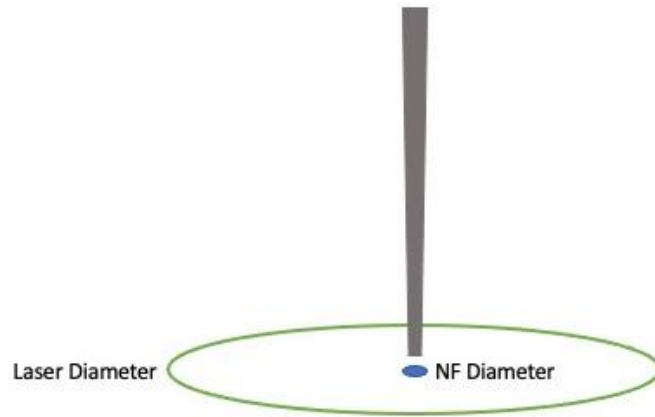
Figure 20: Near-Field vs Far-Field Electric Field Enhancement Diameter. The diameter of the laser upon illumination of the target analyte is the far-field illumination diameter and generates the far-field Raman response. The near-field Raman response is generated by the interaction of the analyte under the metal tip brought within the near-field limit.

The determination of the enhancement factor from a TERS setup is a straightforward process involving the near field found in the tip-enhanced signal and the far field contributions and their respective areas [29].

$$\frac{I_{NF}}{I_{FF}} = \frac{I_{TERS} - I_{FF}}{I_{FF}} = \left(\frac{I_{TERS}}{I_{FF}} - 1\right) \tag{1-165}$$

This is known as the contrast and the enhancement factor is the contrast multiplied by a ratio of the two contributions areas

$$F_{TERS} = \left(\frac{I_{TERS}}{I_{FF}} - 1\right)\frac{A_{laser}}{A_{tip}} \qquad (1\text{-}166)$$

The system setup for a TERS system is generally determined by the system that is adapted into a TERS configuration. The tip control and movement systems are generally the same, but the important consideration is the laser pathway for the TERS system as some setups have opaque surfaces on which the target molecules sit. The laser or the tip will sit perpendicular in all setups as shown in Figure 21. The variety of TERS systems is only limited by the ability to illuminate the surface while the tip is within nanometers of that surface.
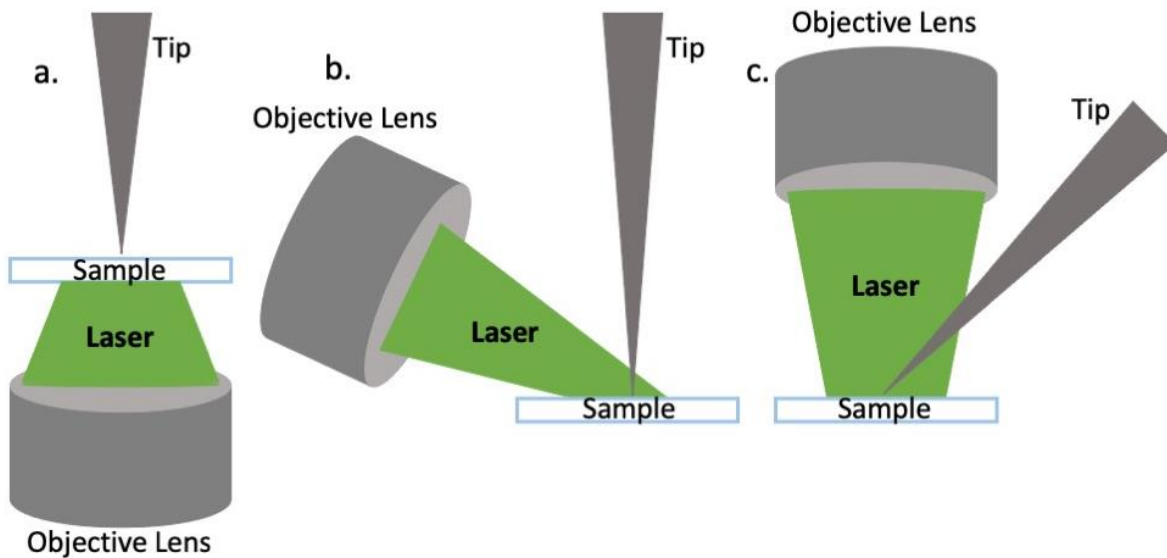
Figure 21: Generalized TERS System Setups. Setup a is used for samples placed on a transparent surface which allows the illuminating laser and subsequent Raman signal through. Setups b and c are for opaque surfaces which require either the laser or the tip to not be perpendicular to the sample surface.

The surfaces in a TERS setup may also be modified to provide an additional enhancement by coating the surface, generally with gold due to its previously mentioned bio-compatibility and environmental stability over other metals [30–33]. The enhancement factor

for TERS systems as calculated in (1-166) range between 10^3-10^7 [34–36]. This enhancement factor is lower than the enhancement factor of a SERS setup (10^7-10^{11}) [37]. The TERS setup enhancement factor is still high enough for single molecule analysis though and is not dependent on complex shape and randomized groupings that characterizes SERS systems.

The applicability of TERS systems to different environments also gives it an advantage over SERS systems in that a TERS system can be used in fluids without damaging the tip. Various groups have used gold tips or gold coated tips to analyze biological samples under water or similar fluids and have demonstrated appreciable signal enhancements [38–40].

2.   Physical System Setup

The TERS microscope physical setup that I constructed for use in the lab will be discussed in this section. This physical setup includes the laser beam pathway, the microscope assembly, and the spectrometer components. This section does not include the Quartz Tuning Fork (QTF) assembly or the tip creation process, these are saved for Chapter 3 and 4 respectively. The microscope setup can be given a generalized overview as shown in Figure 22 and each component will be explained in detail in this chapter as well as the next chapter for the tip assembly.
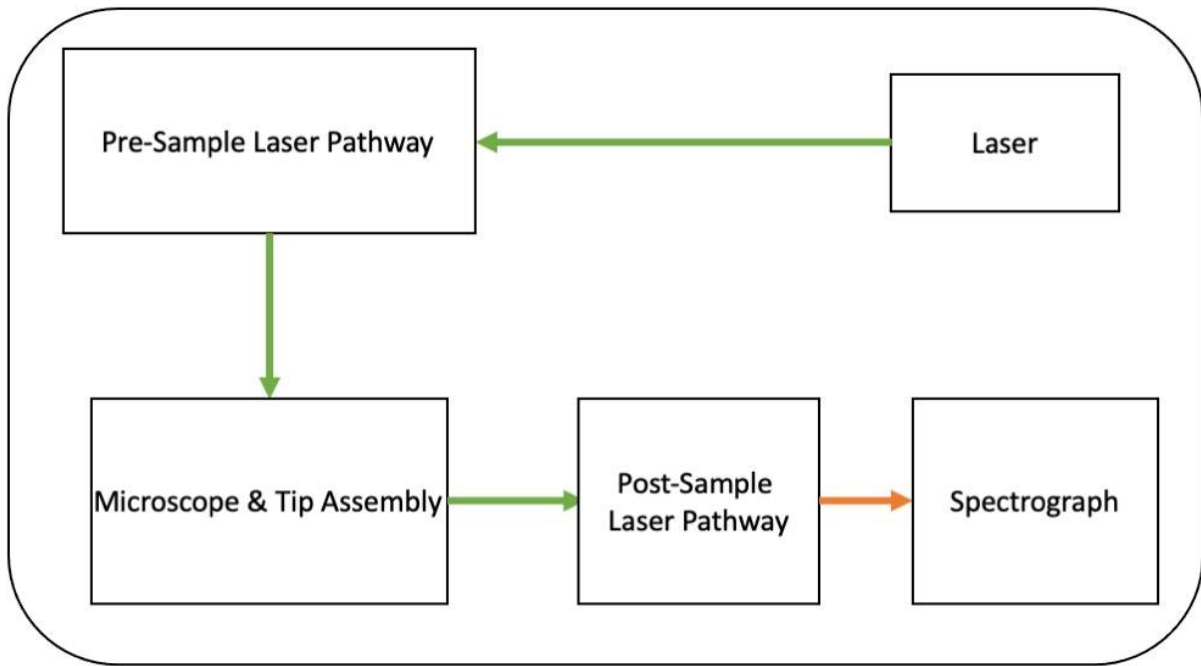
Figure 22: Rudimentary, Assembled TERS System Setup in Laboratory. The figure shows the generalized pathway of the illuminating laser before the interaction with the sample in the microscope and tip assembly component of the system. After the interaction, the arrows show the progression of both the incident laser and resulting Raman signal through to the post-sample pathway. Afterwards, the signal is filtered and presented to the spectrograph for analysis.

2.1 Pre-Sample Laser Pathway

The system utilizes a 50mW, 532nm wavelength, neodymium-doped yttrium aluminum garnet (Nd:YAG) laser by Coherent, Inc. This specific wavelength is advantageous in that it can be used for both biological and non-biological materials without suffering a severe degradation in performance. The use of UV lasers for biological samples causes a stronger fluorescence when compared to 532nm lasers while infrared lasers are not as easily absorbed by silver when compared to the 532nm laser, resulting in a significantly lower electric field amplification needed for the TERS effect. This laser is supported by an optical scissor lift stand that allows

movement in the vertical axis to bring the laser to the approximate height of the center of the input lens in the microscope housing. The laser power of 50mW is too intense of a source for use in SERS or TERS biological applications due to the high Ohmic heating caused by such an intense, enhanced electromagnetic field found in those systems, the excessive heating causes carbonization of the biological samples. The ohmic heating affects all sample types with non-biological samples being more resistant to heat generally when compared to fragile biological samples. To compensate for the intensity, the laser system incorporates a rotating wheel of different optical density (OD) filters of values OD-1 and OD-3 which attenuate the beam from 50mW to 5mW or 50μW respectively. Since Raman signal intensity is proportional to laser intensity, the lower power results in a much lower signal intensity. In addition to the rotating OD filters, there is an additional stack of two OD-1.8 filters in combination with the OD-1 filter that serve to drop the 50mW of laser power to 1.25μW so that during the focusing of the laser on the sample and alignment of the tip, the laser does not overwhelm the camera that shows the objective image.

The attenuated laser goes through a series of alignment mirrors to bring the laser into the proper position to pass through a convex lens that serves to expand the thin laser beam. This expansion allows the laser beam to fill the entirety of the input field lens on the microscope housing that will then pass that beam into the objective lens. It was important to maneuver the convex lens so that the expanded beam past the lens focal point filled the input field lens so that the objective lens has a full light cone in the working area. The alignment mirrors allowed for the alteration of the laser beam going into the microscope assembly so that

the resulting light on the sample was circular and helped to account for any misalignment of mirrors in the optical pathway.
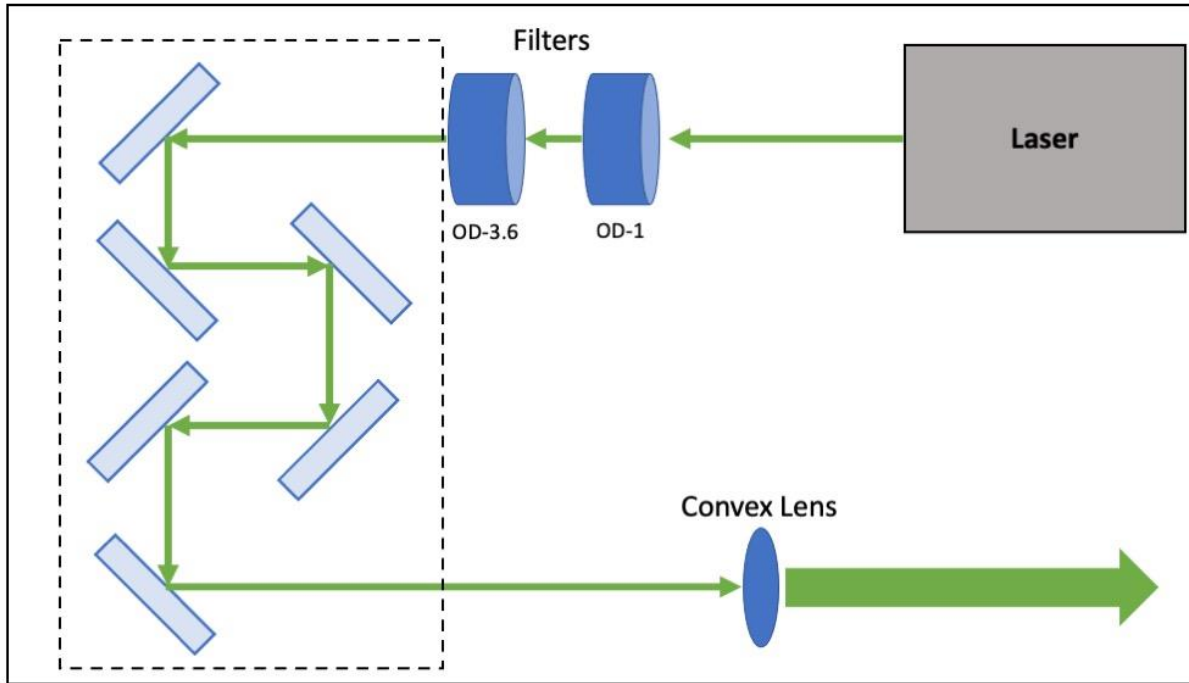
Figure 23: Pre-Sample Laser Pathway of TERS System. The current setup shows the alignment physical setup with the OD-3.6 filter in combination with the OD-1 filter. The alignment mirrors are inside the dashed box and work to correct alignment errors between the laser and the sample due to system errors. The convex lens ($f = 15cm$) works to expand the beam to the size of the input lens on the microscope assembly.
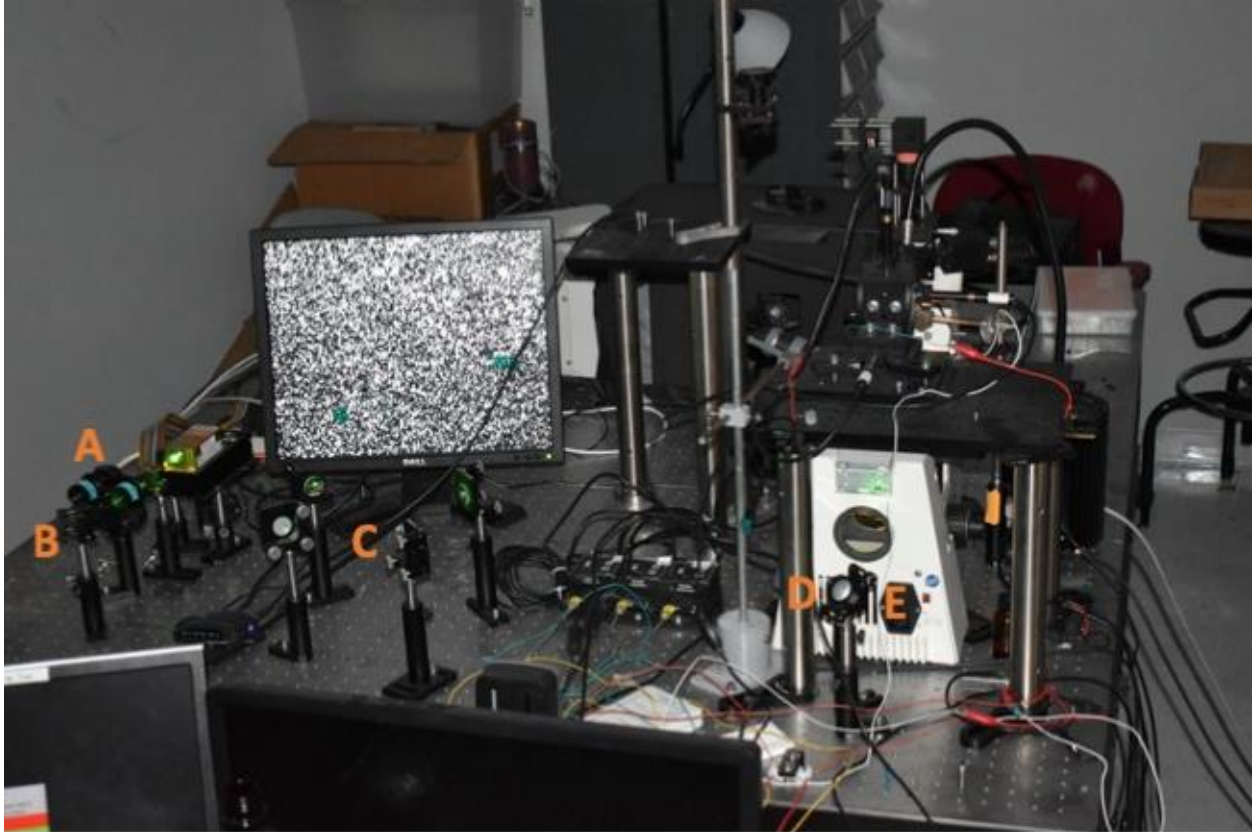
Figure 24: Illuminated Pre-Sample Laser Pathway with Laser On. The microscope assembly is visible inside and on top of the white housing assembly. The OD filters are seen (A), the mirror used to move the laser into the positioning mirrors (B), the positioning mirrors (C), final mirror to move the laser into the microscope assembly (D), and the hidden convex mirror behind D (E) are all part of the pre-sample laser pathway.

2.2   Microscope Assembly

In this TERS system, the microscope assembly is an inverted fluorescence microscope arrangement. The system, an Axiovert S100, allows for laser illumination from the bottom of the sample as well as a space overhead for easy access to the sample area and further illumination with a separate lamp for positioning. The expanded laser from the pre-sample optical pathway is corrected by the input field lens that modifies the beam path, creating a

straighter beam and corrects for aberrations, such as a non-circular beam caused by

misalignment in the mirrors, in the beam pathway as shown in Figure 25.
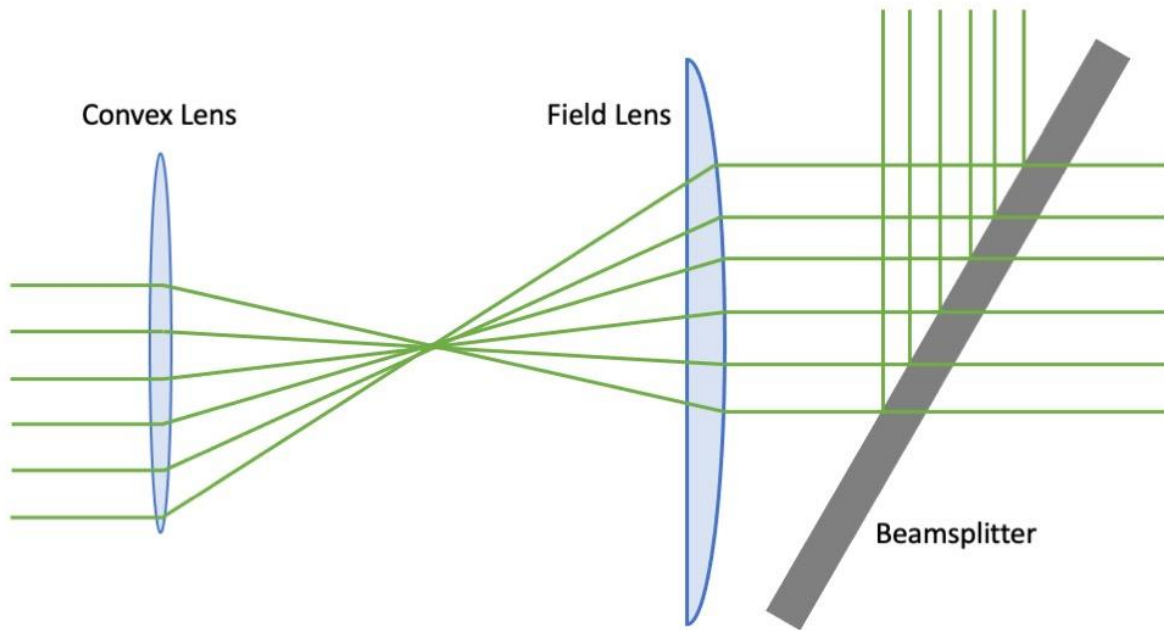
Figure 25: Misaligned Laser Pathway Correction by Field Lens. The field lens works to straighten out the laser to allow the most

amount of light to hit the sample through the objective lens. The field lens also corrects for improper alignment of the laser into

the convex lens as demonstrated above. The beamsplitter reflects a portion of the light perpendicular to the pathway and

transmits the remaining amount of light.

The microscope housing utilizes a beamsplitter to reflect the laser to the sample and transmit

the scattered light from the sample to the post-sample optical pathway. The positioning

assembly floats above the microscope housing on optical pillars to reduce noise to the system.

Inside the microscope house is a movable mirror that moves the post-sample light into an

attached camera. The mirror and camera serve to redirect the light from the sample before it

gets to the post-sample optical pathway. The interruption allows for the imaging of the surface

and sample and is used during the focusing of the laser on the surface, maneuvering the tip,

and maneuvering the stage around in the XY plane. The stage is manipulated in this XY plane using gross and fine adjustment knobs attached to the XY stage that allow the movement on the micron scale with careful use.
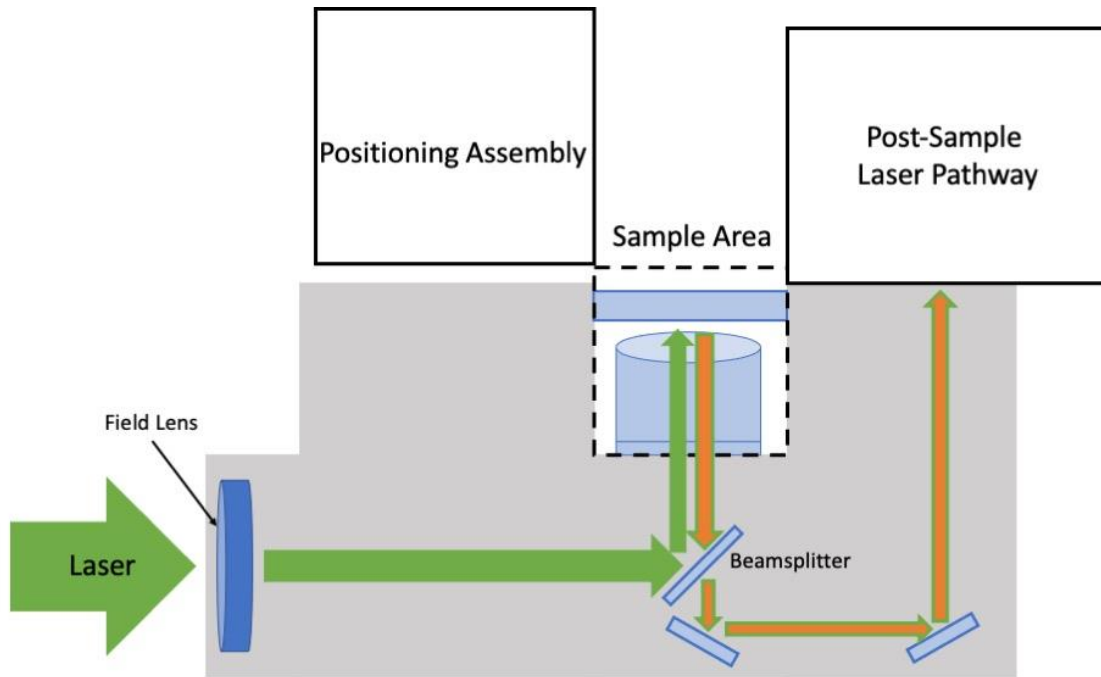
Figure 26: Microscope Housing Assembly showing beam pathway. The beam splitter serves to reflect a portion of the incident and scattered light while transmitting the remaining amount of light from their respective sources. The sample area (dashed) contains the objective lens and the sample on a microscope slide with a hole drilled in sealed by a coverslip. Between the objective lens and sample slide is a layer of immersion oil with a refractive index = 1.2.
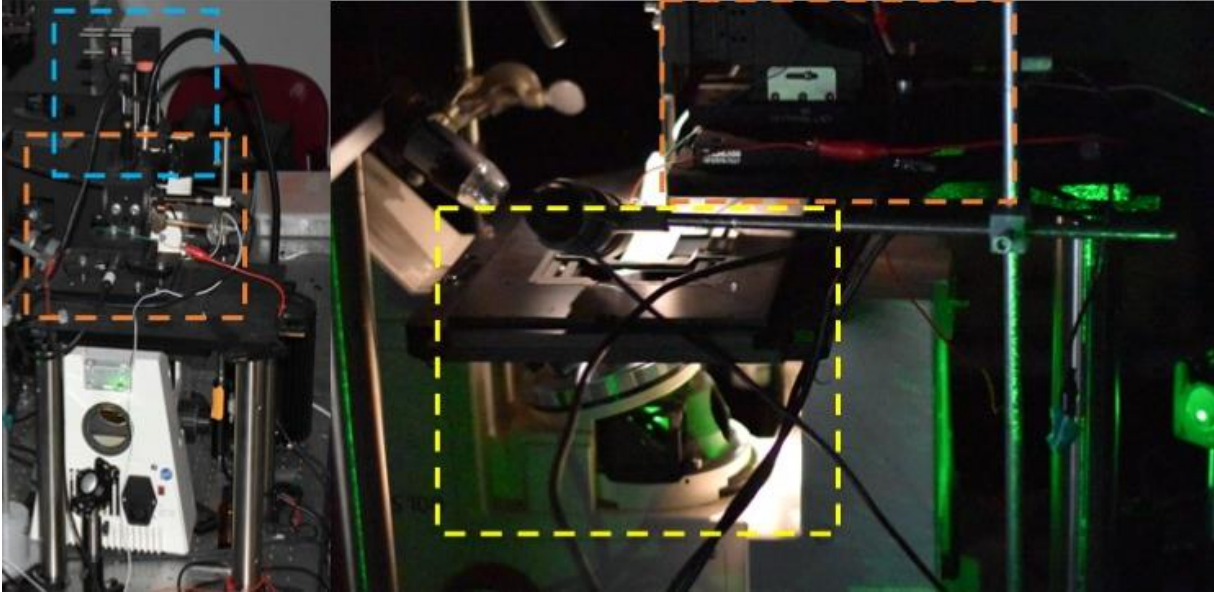
Figure 27: Physical microscope housing assembly setup with sample area. The positioning assembly (orange dashed) is visible in both images and includes both the gross and fine positioning motors. The sample area (yellow dashed) is shown in the second image illuminated with the laser but without an objective lens. The beginning of the post-sample laser pathway (blue dashed) is shown in the background of the first image and is the mirror grouping that moves the vertical laser back down and parallel to the table surface.

2.2.1 Sample Area

The sample area for the system includes the objective lens and the assembly that the sample resides in. The objective lens is a Zeiss C-Apochromat 63x oil immersion lens for use with immersion oil of refractive index = 1.2, The immersion oil has a refractive index of 1.33 as it was initially designed to be used in water immersion applications. This difference in refractive index causes a slight bending of the beam from center when the beam is aligned to the center of the field lens, but this deviation from center is accounted for using the previously mentioned alignment mirrors. The objective lens has a labeled working distance of 0.28mm when using a coverslip with a thickness of 0.17mm and the objective housing is manipulated in the z-

64

direction using a coarse and fine manual adjustment knob that serves to bring the sample in focus.

The beam moves from the immersion oil into the sample assembly. This corresponds to a microscope slide that has a circle cut out of the center that functions as a well to deposit the sample. The well is capped off by a coverslip using neutral vacuum silicone grease to attach the coverslip to the underside of the microscope slide. The immersion oil does not spread out to the edges of the coverslip so there is no threat of contamination of the oil due to the vacuum grease and the grease is very thick at room temperature, so it does not spread out. This allows the coverslip to be pressed tightly against the microscope slide and keeps the coverslip from being skewed from parallel with the microscope slide. The sample is deposited on the top of the coverslip inside the well and can be either solid or liquid if it does not spread to the edges of the well as this will cause potential contamination with the vacuum grease. To prevent this contamination, a smaller sample must be used when compared to the size of the well and it the sample is deposited in the middle of the well. If there is contamination, it is simple enough to peel the coverslip off and place a new coverslip off to attempt correct sample deposition again.

2.2.2   Gross Positioning

The gross positioning of the tip assembly is handled by a set of ThorLabs Z712B stepper motors. There is one stepper motor for each cartesian axis that push against the XYZ linear stage that holds the tip. These motors have a step resolution of 40nm and a travel range of 12mm. The motors are used to position the tip into the Van der Waals force interaction range of the tip with the surface, usually in the range of 10-45nm [41,42]. The interaction between

65

the Van der Waals forces and the tip produces a change in the resonant frequency of the tip explored in Section 3.

2.2.3   Fine Positioning

The fine positioning of the tip relative to the surface sample is achieved via piezoelectric actuator in the designated z-axis of the setup, perpendicular to the analyte surface. The stated maximum range of the piezoelectric actuator, a PiezoDrive SA050510, is 14μm when operated through a voltage range of -30V to +150V. The actuator movement is driven by the applied voltage from a PiezoDrive PD200 Amplifier configured to an output of 0V to +100V for automated movement controlled by external hardware. The manual for the actuator states that if the motor is driven from 0V to 150V instead of the preferred range, the total movement is reduced by 25%. This results in a total driving range of 10.5μm but this is further modified by the reduced voltage driving range that the amplifier is configured to. The piezo actuator stack is configured for movement in only one direction, and we assume the movement to be linear to the amount of voltage applied. This was shown to be an accurate assumption as a previous study had shown the forward movement to be linear and the return movement to be a slight quadratic response over the range of 0V to +100V [43]. Using this assumption, the total driving range of the configured piezo actuator would be 7μm. The piezo amplifier works by upscaling an applied voltage from an input signal into the output voltage that goes to the piezo motor. The maximum input voltage at the piezo amplifier of the setup through the myDAQ output is +5V. Using the linear assumption once again, the input voltage of +1V yields a theoretical movement of 1.4μm.
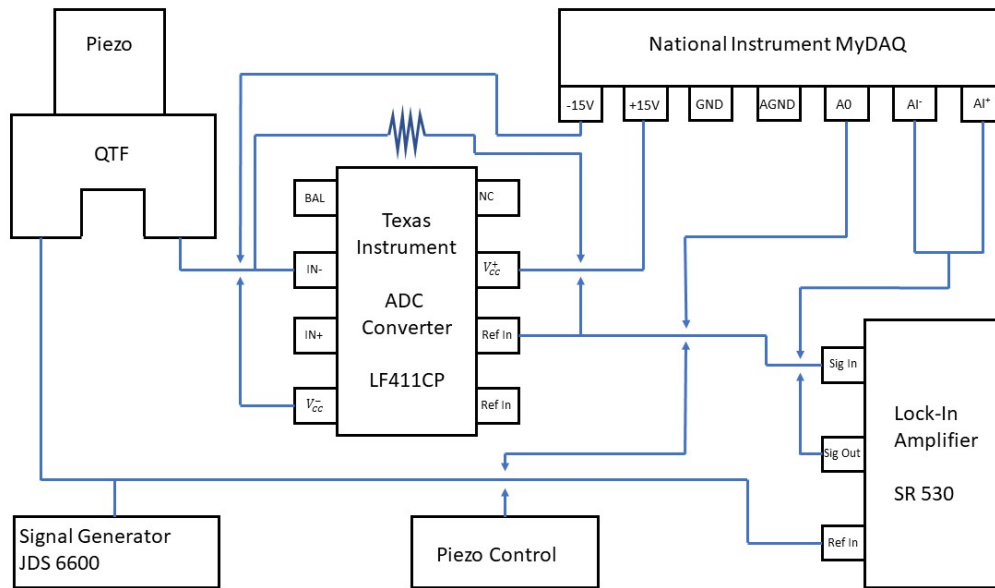
Figure 28: Circuitry Related to Fine Positioning System. The MyDAQ hardware connects to the LabVIEW software for hardware integration and is the port for input or output signals. The ADC Converter is used to amplify the signal from the QTF-tip assembly and is further explained in Chapter 3. The piezo control is wired into the MyDAQ hardware and amplifies the input to drive the piezoelectric actuator.

The piezo actuator stack pushes against a rigid, printed, resin bridge that the tip setup is attached to resulting in some attenuation of the setup due to the material not being perfectly reactive to the movement of the piezoelectric stack and thus, absorbing some of the movement each time resulting in less than a 1:1 piezo to bridge movement ratio. The mass of the bridge also causes an attenuation of the theoretical movement but this can be considered negligible as a previous study by NASA showed that a mass of 9kg showed an approximately 50% reduction in movement range for a piezoelectric actuator stack while the resin bridge has a total weight measured in grams [44].

67
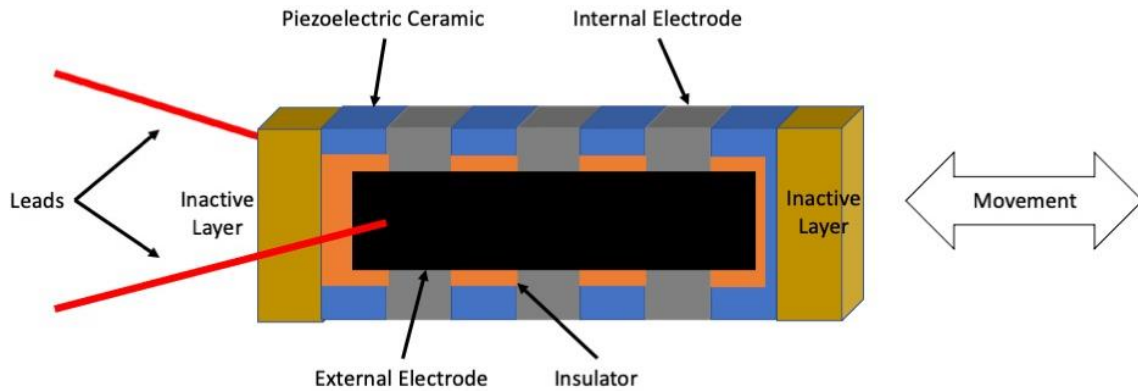
Figure 29: Piezoelectric Stack Actuator with Linear Movement. The inactive layers are in contact with the base and the object being moved by the piezoelectric actuator. The external electrode (black) connects all the internal electrodes (gray) in parallel. The leads (red) are connected to an amplifier to generate the voltage needed to cause appreciable movement in the piezoelectric ceramic (blue). The stack actuator can press forward and relax backwards as one effective crystal. The entire actuator is then sealed in non-conductive tape to isolate the electric components from the environment.

The positioning of the stack is calculated in the software using the assumption that the increases of voltage yield perfect theoretical movements calculated from the manuals. The difference between the expected and real movement range of the piezo could not be measured with sufficiently sensitive equipment to detect any discrepancy. A future refinement would be to use a technique such as an optical interferometric measurement to measure the expansion and contraction of the piezo-tip assembly over 100 cycles to determine a mean discrepancy between the expected and real ranges with sub-nanometer resolution.

2.3   Post-Sample Laser Pathway

The signal from the sample is passed through the microscope assembly and enters the post-sample laser pathway. This pathway consists of a series of mirrors that work to align the beam like in the pre-sample laser pathway before putting the signal beam through a convex

lens and a filter. As the beam exits the microscope assembly, it is pointing vertically towards the

ceiling and needs to be reoriented to parallel to the table surface as well as being close to the

table surface. The beam passes through three mirrors that work to do this, but the beam is

slowly diverging from a center bright spot. The diverging of the beam is caused by the beam

pathway being significantly longer than the designed pathway of the objective lens but it is not

a significant spreading of the beam in practice. The diverging beam passes through a series of

four mirrors that allow for the adjustment of the beam before the convex, focusing lens and

filter and into the spectrometer. The convex lens ($f = +15cm$) is positioned so the focal length

is just inside the spectrometer entrance slit. The focusing light travels through a longpass filter

designed to cut off wavelengths at or shorter than 532nm, the wavelength of the laser. This

serves to prevent burnout of the sensor and allow the weaker Raman scattered light to be

observed.
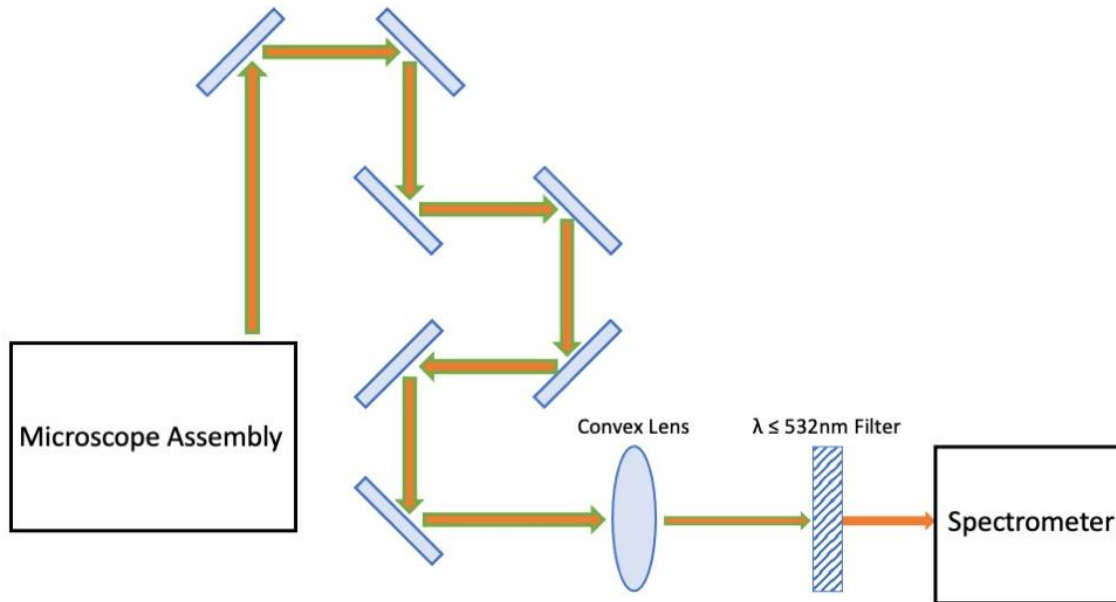
Figure 30: Post-Sample Laser Pathway. The signal beam exits the microscope assembly and is reflected off the first three mirrors to bring the beam near to the table surface for reduction in the jitter of the optical hardware. The next four mirrors function like in the pre-sample laser pathway to correct alignment issues with the beam and optimize the beam into the spectrometer. The convex lens ($f = +15cm$) focuses the dispersed beam through the filter, that eliminates the laser wavelength, and into the spectrometer assembly.
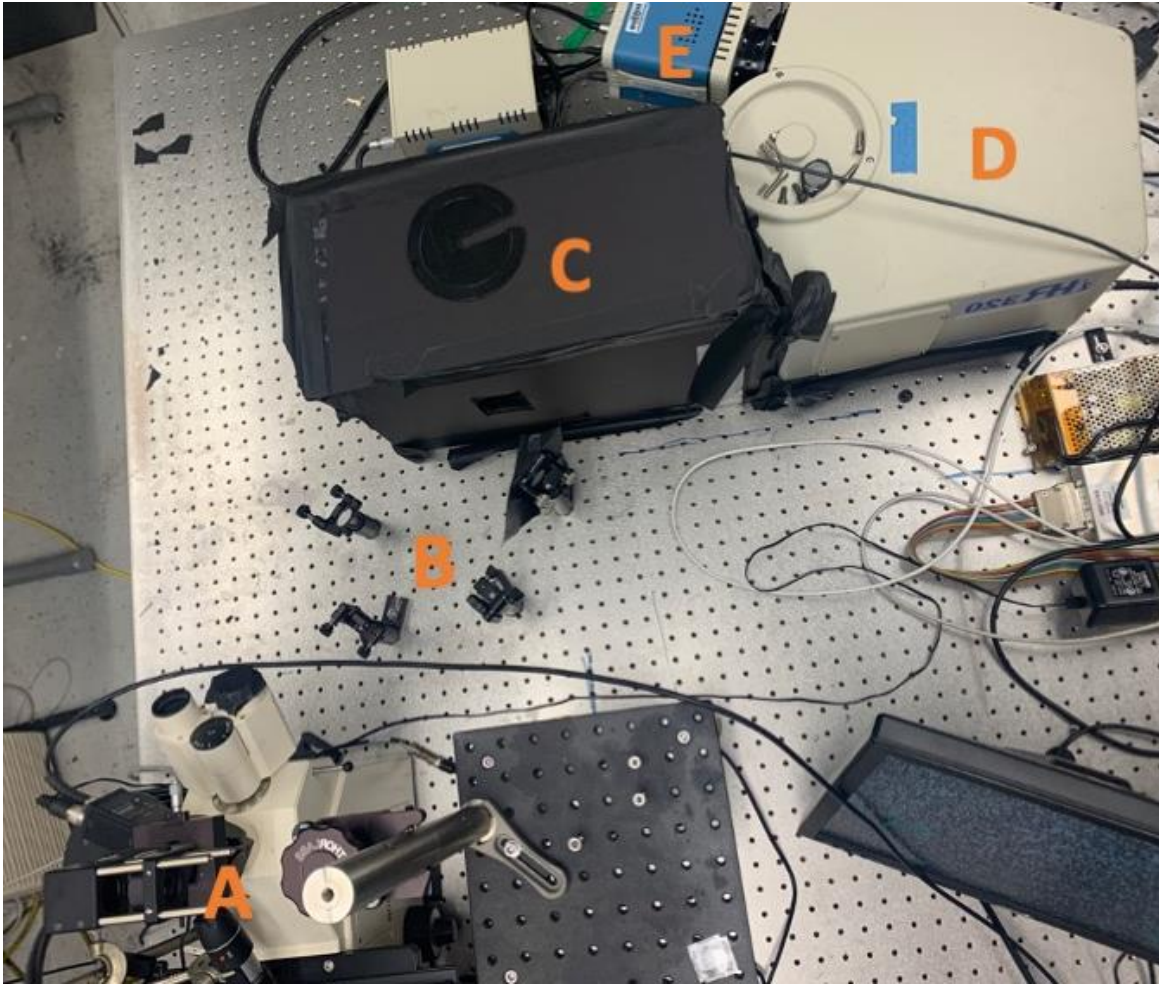
Figure 31: Physical post-sample laser pathway. The laser enters the post-sample pathway in the mirror group (A) that takes the vertical laser pathway and rearranges it to be parallel with the table and close to the table surface. The positioning mirror group (B) allows for pathway correction of the laser entering the camera housing. The final mirror, focusing lens, and laser filter are inside the sealed housing (C) and the laser passes into the diffraction grating housing (D) before the spectrum is recorded at the CCD camera (E).

2.4   Spectrometer

The filter signal exits the post-sample laser pathway and moves into an iHR 320 spectrometer. The spectrometer has a spectral range of 250-950nm and a resolution of 0.2nm. The filtered signal hits a mirror and then is reflected off a diffraction grating into another mirror

which finally reflects the diffracted signal into the attached charged-couple device (CCD) camera. The camera, a back-illuminated CCD camera, determines the incident photon count per pixel and converts this data into a signal intensity per pixel, which results in a system spectral resolution of 0.18nm.

The spectrometer has a box constructed in front of the entrance slit that serves to cut off as much stray ambient light as possible such as from the laser or any of the hardware lights. The CCD camera has a Peltier cooling system that allows the camera to operate at -80°C, this serves to reduce the effect of thermal noise in the image. The raw data is passed from the CCD camera to a separate workstation running Horiba Jobin Yvon imaging software that converts the data into the required signal intensity count spectrum.
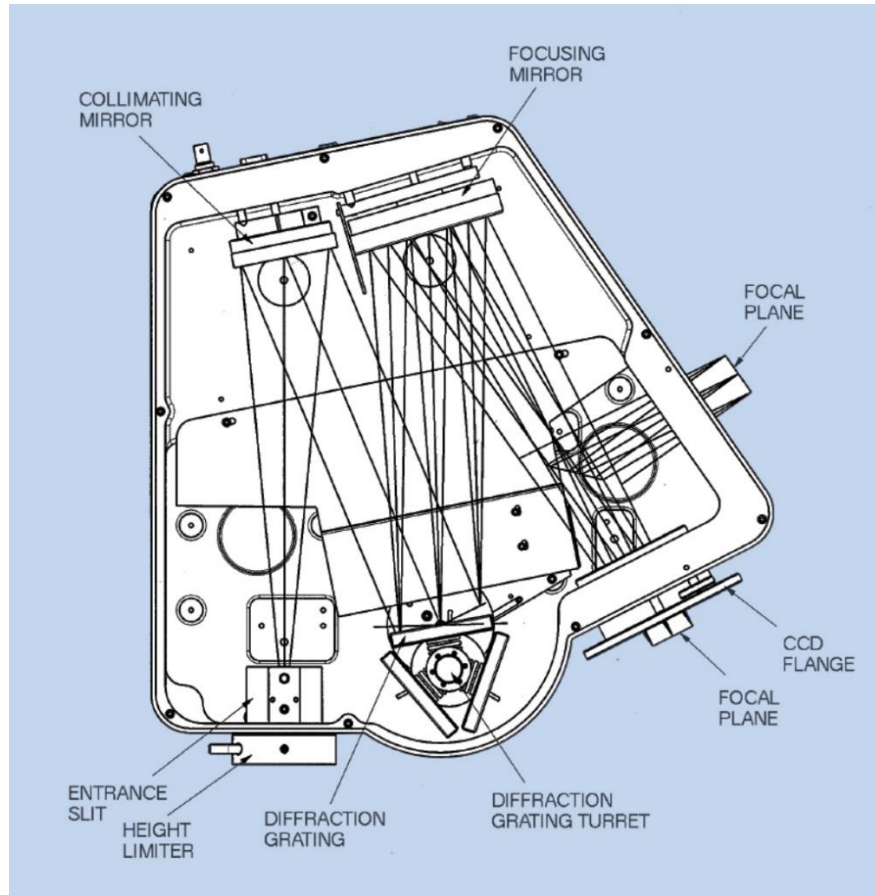
Figure 32: Beam path diagram of iHR 320 Spectrometer. The spectrometer used has an effective spectral range of 250-950nm and the CCD camera has an effective range of 200-1100nm [45].

3.   Tip Assembly

The tip assembly involves the QTF, the circuitry needed to amplify the output signal from the QTF-feedback system, and the parts used to hold the QTF-tip assembly. The function of the QTF was previously discussed in Chapter 2. We will then focus on the signal circuitry and the components used to hold the QTF-tip assembly.

3.1   Signal Circuitry

The foundation upon which the microscope is built upon is the use of a QTF as a sensor to prevent the silver tip from contacting the surface by detecting the surface through a change in the resonant frequency of the QTF. The QTF consists of two quartz prongs that have electrodes that are electrically separated in each prong.

Figure 33: De-Canned Quartz Tuning Fork. The quartz prongs have electrodes inside that are electrically isolated from one another. These electrodes are then connected to a metal leg.

The quartz substrate has a known natural resonant frequency of 32,768Hz [46], in the tuning fork configuration, at which point the prongs experience the largest deformation from the rest point. Because one electrode is connected to an input voltage, the change in the position of that prong in which the driven electrode is incased causes a charge separation. The charge separation is largest at the resonant frequency and thus the largest induced current is caused at this point due to the vibration of the prongs having the largest amplitude [47].

The output current from the QTF is converted to a voltage value using a transimpedance amplifier circuit shown below in Figure 34. The amplifier circuit consists of a feedback resistor

and an operational amplifier also known as an op-amp. In this setup, the incoming current is passed solely through the feedback resistor which corresponds to an output voltage using Kirchhoff's Current Law:

$$V_{div} - V_{out} = I_{in}R_f \qquad (3\text{-}1)$$

For an op-amp, there is no current being passed through it. The op-amp is powered through a supply, in this case ±10V from the myDAQ controller, and uses these power supply sources to balance out the modified output voltage with the voltage difference between the positive and negative pins on the op-amp, thus $V_{div} = 0$. The maximum output voltage in the system is equal to the maximum power supply voltage, in this setup, 10V. It is then possible to calculate the maximum input current of the system before signal saturation if we ignore the sign of the voltage:

$$\frac{10V}{100k\Omega} = 100\mu A \qquad (3\text{-}2)$$

The input current then must be equal to or less than $100\mu A$ to produce a useful output voltage.
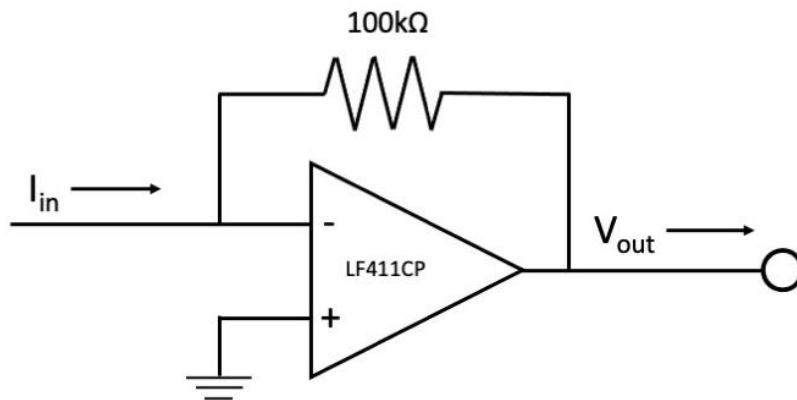
Figure 34: Transimpedance Amplifier Circuit. The amplifier circuit converts the incoming current into an outgoing voltage after amplification. The circuit utilizes a LF411CP op-amp as a signal voltage stabilizer.

The output voltage, through amplification, will contain signal noise so the output signal is sent to a lock-in amplifier for noise reduction in order to provide a more accurate feedback system. The lock-in amplifier, a Stanford Research Systems SR-530, compares the incoming signal with a reference signal. This reference signal has no system induced noise and is multiplied by the input signal that has a weak signal to noise signal ratio. Through multiplying and then integrating the product of the two sine waves over a defined period, a lock-in amplifier can filter out the signal noise. Since noise is random, the product of the input signal noise and the reference signal will average out over time to be zero while the product between the desired signal in the input signal and the reference signal will always be positive as they are the same sign always.

3.2   Tip Holder

The thought process behind the creation of a holder for the QTF was it had to be easily prototyped, repeatable, easy to place and remove from position, and stable when attached. With these goals in mind, it was easiest to use a resin printed holder. The resin printing allowed for printed resolution of 100μm for the holder which allowed for opposing parts to fit together easily. With the resin printer, a FormLabs Form 2 Resin Printer, the usual defects caused by thermal curing in PLA printers is not an issue, so the parts are more repeatably produced.
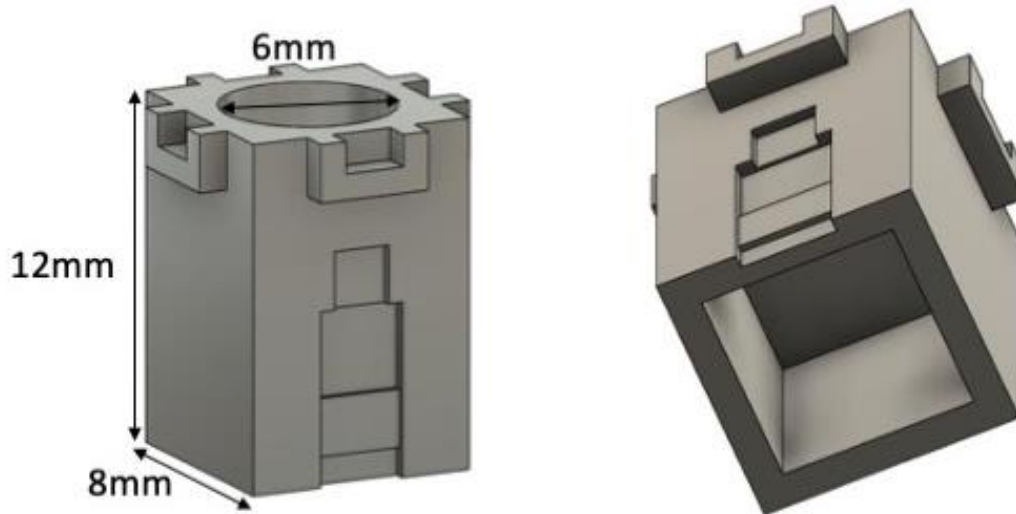
Figure 35: Quartz Tuning Fork Assembly Holder. The holder is printed in UV resin using a FormLabs Form 2 printer in house. The

tolerances are within 100 microns. The walls are 1mm thick and the circular impression in the left diagram is 2.1mm deep to

house the circular magnet snuggly. The QTF is glued into the groove with the ends of the prongs hanging past the edge of the

holder. The superglue, once hardened, prevents any movement of the QTF base which could retard the tip resonance.

The ability to easily mount and dismount the holder from a larger, permanent rig necessitated

the holder to use magnets to attach to the larger setup. The depression for where the magnet

is glued into the QTF holder can be seen in Figure 35 and is 2.1mm deep so that the magnet

does not protrude above the holder's top surface. The magnets used to couple the setups are

simple, circular magnets with an outer diameter of 6mm and a height of 2mm.

An important part of the QTF holder setup is the wings at the top of the setup in Figure

35. These wings correspond to a related feature on the larger assembly and serve to keep the

holder aligned in one of four positions at the cardinal positions. They also serve to provide a

method of resisting minor bumps during the attaching of the holder to the larger assembly.

Finally, for the ease of prototyping and reducing the material needed to print, the interior is hollowed out with the walls only 1mm thick.
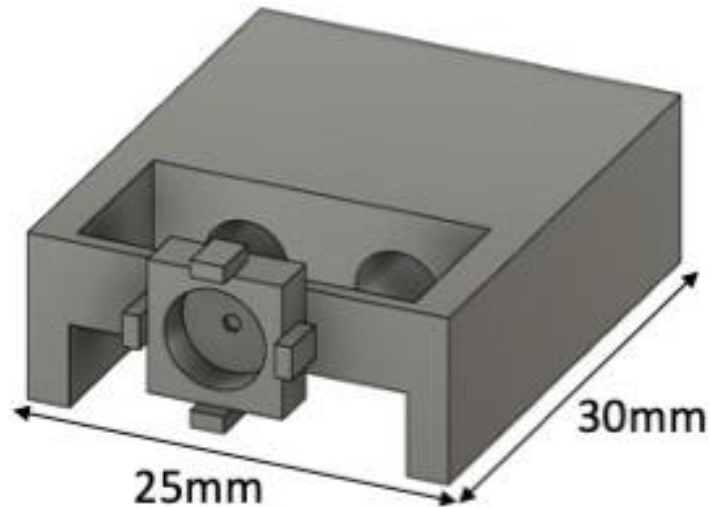
Figure 36: Piezo Holder Diagram. The piezo fits in the open area behind the protruding square. The bridge that the piezo holder pushes on is 1mm in thickness. The two circles visible in the setup are tunnels for the voltage wires of the piezo stack to go through.

The QTF holder magnetically attaches to the piezo holder, shown above in Figure 36. The piezo stack slots into the empty area behind the thin bridge which is printed to be just smaller than the piezo stack. The stack puts slight pressure on the bridge at 0V and presses on the bridge as a voltage is applied across it. An identical magnet to the one glued into the QTF holder is slotted into the depression on the bridge and is what allows the QTF holder to be magnetically attached. The fins sticking out of the front in Figure 36 are what slot into the wings in Figure 35 to provide stability and final alignment.

4. Tip Creation Process

The most important part of a TERS system is the tip where the signal amplification occurs, without this it is just a Raman system with no real enhancement. Several options were explored for tip production before the right solution was found. The tips would have to be durable enough for handling and attaching to the holders, spectroscopically neutral to not introduce artifacts into the signal, and cheap enough to allow for effective prototyping. The ideal tip production process does not rely on chance to produce a tip and should work to ensure the lowest levels of contamination during the process. Several research groups have recently published AFM-TERS systems using silver-coated AFM probes to produce the enhancement needed for TERS studies [48–53]. Traditionally, the more studied metal-AFM probe was gold due to the inherent chemical stability of gold [54–57].

The TERS tip assembly and tip production is a slowly evolving process that over time yielded a reliable tip production process. Through this process, three main stages were researched: pulled glass tips, coated copper tips, and etched silver wire tips.

4.1 Pulled Glass

The first attempt at making a suitable tip for TERS focused on using a pulled capillary glass tube coated in silver nanoparticles (AgNP). The glass would function as the matrix to build the AgNP matrix on and would allow for the attachment of the glass pipettes to a XYZ Micrometer Stage. With the glass tubes pulled to the desired thickness, the ends were sealed using a heated tungsten wire to create a sterile tip. The process resulted in tapered, sealed glass tips that would then be placed in a concentrated AgNP solution and allowed to dry. This

would leave a thin layer of AgNP's adhered to the surface of the tip with a diameter in the tens of micrometers.

This creation process was abandoned in the project due to the irreproducibility of the AgNP attachment to the glass tips, the large width of the tips, the reliance on the manual micrometer for the tip approach, and the very large mass of the tips for use in automated approaches to the surface. It was the first major step in the total process of the tip creation but would be better served using the AgNP's in their original purpose, as a SERS substrate.

4.1.1 Creation Parameters

The glass tubes, with an outer diameter of 1mm and an inner diameter of 0.5mm, were placed inside a Sutter Instrument Company Model P-2000 Laser Micropipette Puller to create the unsealed tips. The P-2000 manual listed the following system parameters with the effects of the change in the parameters.

Table 12: Laser micropipette puller system parameters. The different parameters govern the diameter of the end of the tip as well as the length of taper for the tip.

Parameter	Increase	Decrease
Heat	Smaller tip diameter Longer taper	Large tip diameter Shorter taper
Pull	Smaller tip diameter Longer taper	Larger tip diameter Shorter taper
Time	Shorter taper	Longer taper
Velocity	Smaller tip diameter	Larger tip diameter

The sealing process of the tips generally created a tip that was 5 times the diameter of

the tip before sealing. The puller system used a custom program of different specifics related to

the parameters above in Table 12. The Heat parameter has two components; the Heat term in

the program was the output power of the laser and was recommended to be set to 350 of 999

and the Filament term was the longitudinal distance heated by the laser and was chosen to be

6.5mm to prevent the uneven heating of the glass, corresponding to a value of 4 in the

program. The Pull parameter and Velocity parameter are related and have two components;

Velocity is the speed of the constant pull applied by the system and corresponds to a glass

temperature once the glass begins to soften and the Pull term is the force of the hard pull

generated by the system once a set period is reached. Finally, the Time parameter has a Delay

term that describes the time between when the laser is activated, and the hard pull is activated

with a value over 128 causing the pull to happen after the laser is turned off.

Table 13: Tip pull system program parameters.

Heat	Pull	Velocity	Time	Filament	Tip Diameter After Sealing (μm)	Tip Diameter After Sealing (μm)
295	0	25	200	4	10	50
295	0	50	200	4	2.5	10
295	0	35	200	4	5	25
295	0	65	200	4	2	5
295	0	65	250	4	13	50
295	0	65	215	4	2.5	12.5

295	0	65	230	4	2	12.5

The tips were cleaned after the sealing process to eliminate any contamination before coating

with the AgNPs. The cleaning process was:

1. Swirl tips in boiling Cole-Parmer Micro-90 glass cleaner diluted following label

   instructions

2. Swirl in air for 3 seconds to remove excess cleaning solution

3. Swirl in Milli-Pore water for 10 seconds

4. Swirl in air for 3 seconds to remove excess water

5. Allow to air dry

The tips were coated in AgNPs layer by layer after the cleaning process. Each tip was

submerged in a $5\mu L$ of the AgNP solution inside a microcentrifuge tube and then placed inside a

vacuum oven. The oven was then placed under vacuum at ambient temperature for 15 minutes

to allow the water in the AgNP solution to evaporate, leaving behind a thin layer of AgNP's on

the glass tip. This process was followed for 6 layers which finally resulted in a tip that had over

50% AgNP coverage.

4.1.2   Silver Nanoparticle Synthesis

The nanoparticles used to coat the sealed glass pipettes were made using a modified

two-step process by Aherne et. al. [58]. The two-step process involved creating a silver-seed

solution before slowly adding silver nitrate over time to create triangular nanoprisms. The

solution, in the original process, was concentrated through centrifugation while in the modified

process the solution is concentrated using rotary evaporation. The modified nanoparticle

synthesis process is as follows:

- Add the following ingredients together:

    o 5mL Trisodium Citrate (10mM)

    o 1mL Sodium Borohydride (10mM)

    o 0.25mL Poly(styrene sulfonate) (500mg/L)

- Using an automated syringe pump, add the following to the total solution:

    o 5mL Silver Nitrate (0.5mM) at 2 mL/min

- Using a mixing bar to continuously stir solution once 2.5mL of Silver Nitrate ($AgNO_3$) is

    dispensed.

The unmodified process has the same ingredients but differs in the start of the mixing with the

unmodified process mixing the solution from the beginning. This seed solution, goldenrod in

color, was then added to a mixture of deionized (DI) water, Ascorbic Acid (AA), and $AgNO_3$ at

various amounts with the goal of creating a deep violet nanoparticle solution.

Table 14: Silver Nanoparticle Synthesis Process from Silver Seed Solution.

Trial Number	DI Water Volume (mL)	Ascorbic Acid (10mM) Volume (μL)	Seed Volume (μL)	$AgNO_3$ Volume(mL)/Rate	Final Color
1	5	75	400	3 @ 1mL/min	Deep Purple
2	5	100	400	1.7 @ 1mL/min	Purple/Violet

3	5	100	400	2.4 @ 1mL/min	Deep Purple
4	10	200	800	3.4 @ 1mL/min	Reddish-Purple
5	10	200	800	3.4 @ 2mL/min	Reddish-Purple
6	10	200	800	4.0 @ 2mL/min	Burgundy
7	5	100	400	1.7 @ 1mL/min	Violet
8	10	200	800	4.0 @ 1mL/min	Reddish-Purple
9	10	250	800	4.0 @ 1mL/min	Reddish Purple
10	10	150	800	4.0 @ 1mL/min	Burgundy
11	10	200	800	3.4 @ 1mL/min	Burgundy
12	10	200	800	3.4 @ 1mL/min	Purple
13	10	200	800	4.0 @ 1mL/min	Reddish-Purple
14	25	500	2000	8.5 @ 2mL/min	Reddish-Purple
15	5	100	200	1.7 @ 1mL/min	Deep Purple
16	50	1200	1600	13.0 @ 2.5mL/min	Violet

All solutions were capped with trisodium citrate (10mM) 30 seconds after the last of the $AgNO_3$ was added to the solution at a ratio of 1mL for every 8.475mL of the AgNP solution. The solutions were left on the counter for the two-week Winter vacation to determine solution stability with only the last solution being stable at room temperature during this time. The

recipe is sensitive to environmental temperatures, attempts at synthesis were most successful at 70-73 Fahrenheit.

Figure 37: Synthesized Ag nanoparticle solution showing stability. The prepared solutions are shown comparing their color from Purple to Burgundy to Violet from left to right. The solution on the right has shown stability for over four months at inside a refrigerator at the time of the photo.

The recipe was further modified by concentrating the AgNP solution using a rotary evaporator instead of centrifugation with filters. The lab did not have a centrifugation setup with the necessary filters. The rotary evaporator works by lowering the pressure of a vessel while also raising the temperature of a water bath the vessel sits in. This works to lower the boiling point of the solution without significantly raising the energy of the system which would cause the nanoparticles to aggregate too quickly and crash out of the system. The goal of the evaporation process in this synthesis is to concentrate the solution without causing further aggregation of particles so the color of the solution should stay the same. The concentration process began with a goal of a 10:1 reduction in volume while maintaining a violet color.

Table 15: Ag Nanoparticle Evaporative Reduction Process. Each row is the next step in the evaporation process with the starting solution being solution #16 in Table 14. The AgNP solution is inside a 1000mL round-bottom flask to maintain a large solution surface area.

Pressure (mbar)	Water Bath Temp (°C)	Coolant Temp (°C)	Rotation (rpm)	Time (min)	Initial Volume (mL)	Final Volume (mL)	Color
40	45	5	0	90	66	60	Violet
150	45	5	15	120	60	43	Violet
100	50	5	15	120	43	31	Violet
115	50	5	15	105	31	30	Deep Violet
70	50	5	0	135	30	9	Almost opaque Violet
105	60	5	15	60	9	6	Almost opaque Violet

The nanoparticle solution was generally opaque unless very thinly spread inside the container, after which it was a deep violet. The periods without rotation during the process were the result of the inability of the rotary evaporator to drop pressures below 100mbar while rotating. The apparent evaporation limit is around 2:1 at 50°C without dropping the pressure of the system below 100mbar. The resulting nanoparticle solution showed signal enhancement

effects and color stability six months after concentration when kept at ambient room temperatures in the building which swing between 65°F and 85°F depending on the season.

4.2 Silver-Coated Copper Wire

The next attempt to produce reliable, low-cost TERS tips was the use of an etched copper wire coated in silver nanoparticles. The copper wire would serve as a substrate for the AgNP's to adhere to and could be trimmed down if it was too long of a wire unlike the pulled glass tips. The wire was attached to a quartz tuning fork (QTF) after etching and coating with the AgNP's. This assembly, an etched wire superglued to a QTF, is the standard assembly used in this microscope and allows for z-axis positioning as explained earlier. The attachment of the wire to the QTF with superglue proved to be difficult as the mass added by the glue could further retard the resonance response of the QTF-tip assembly, the handling of the tip during the attachment process could damage the tip, and the non-uniformity of the tip lengths and attachment points resulted in tips that could be 0.5mm longer than others; making the approach process harder. The copper wire proved to be too heavy of a substrate and was prone to heavy corrosion after the etching process, so it was abandoned as a tip candidate after months of testing and improving the process.

4.2.1 Etching Process

The etching process consisted of a simple electrolytic setup. There were studies performed using an electrochemical bath to etch gold [59–62] and since the chemical reaction process for copper is very similar to gold [63], a similar etching process for copper can be performed with hydrochloric acid (HCl). The etching process involves dipping the copper wire

into a solution that causes a meniscus to develop around the wire. The chemical reaction of copper being dissolved into the etching solution when a current is run through the solution generating copper chloride ($CuCl_2$) and reducing the diameter of the wire. As the diameter gets smaller, the tip starts to develop at the meniscus and the weight of the remaining copper in the solution will cause the tip to break off at the air interface. This leaves a very sharp tip right above the surface of the solution. As noted, previous studies utilized HCl to etch the gold as the gold wire is much more chemically inert. Copper is not as chemically inert, so a solution of sodium chloride (NaCl) was used instead as it still provided the necessary Cl^- ions for the reaction but is much safer. A voltage of 5V was applied to the solution through a stainless-steel loop electrode and the copper wire. The etching process is slower with NaCl than with HCl so it took around 4 minutes to perform the etching compared to 15s for the HCl in the previously cited literature. The process yielded tips with diameters of 5-10 microns with an initial starting diameter of 320 microns.
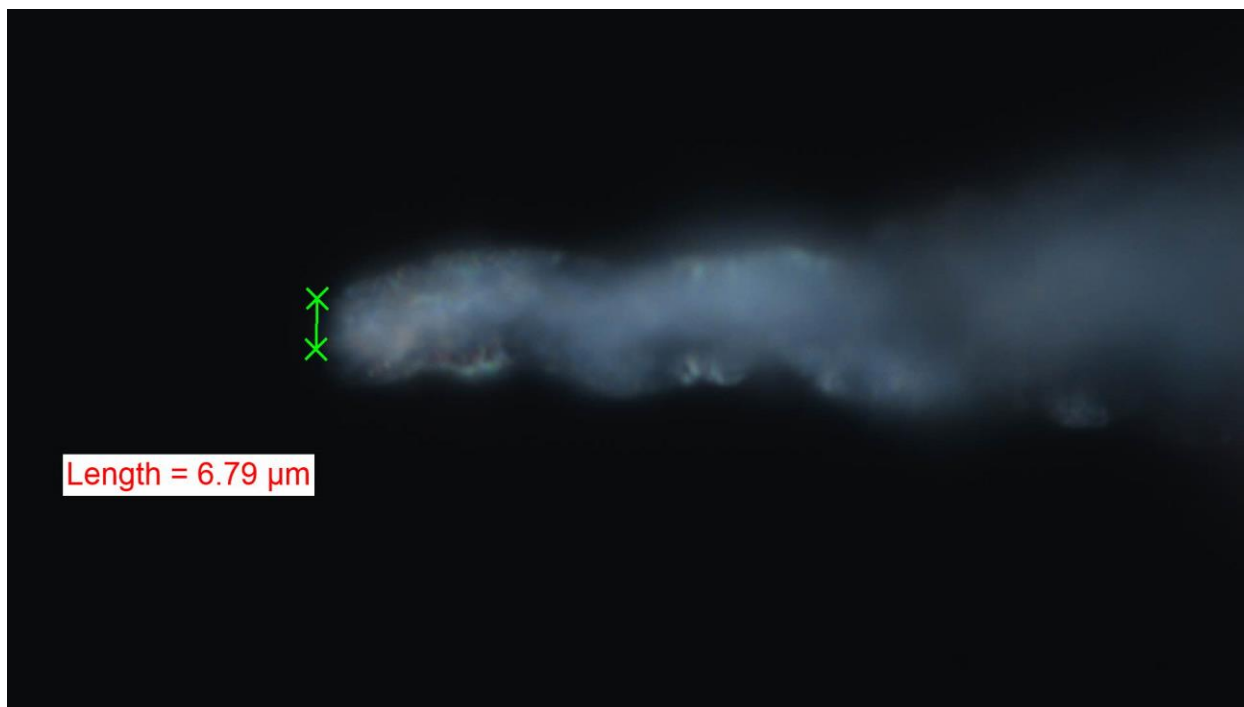
Figure 38: 7 Confocal Microscope Image of Micron diameter Etched Copper Tip. The tips show surface irregularities due to bubble formation during the electrolytic etching process.

4.2.2   Coating Process

The coating process for the copper tips is a simple procedure compared to the pulled glass tips. The etched copper tips were washed several times in Millipore water to remove any traces of the saltwater solution. They were then dipped in a solution of Millipore water and silver nitrate ($AgNO_3$). This aqueous solution of $AgNO_3$ would begin to precipitate silver nanoparticles onto the copper tip substrate, producing a thin layer of silver nanoparticles.

4.3   Etched Silver Wire

The final type of TERS tip developed was that of an etched silver wire. Silver wire was chosen to reduce the weight of the tip on the QTF compared to the copper wire. Several research groups developed procedures to etch silver wire electrochemically [64,65] for use in

scanning tunnel microscopy. These tips could function as TERS tips as well and used ammonia as the electrolyte coupled with a platinum-iridium wire loop. The final tips produced by those groups had diameters under 100nm. Their production process yielded tips that were very fragile and would not survive any accidental contact with the surface, so a different method was used yielding blunter tips.

The wires used had a smaller unmodified diameter, 50 microns, compared to the copper wires and were more chemically stable in the humidity of the building. The tips were etched in 15M nitric acid (HNO_3) until the weight of the remaining silver caused the tip to break off, similarly to the copper tip process. The nitric acid was chosen because the original silver substrates where SERS was first demonstrated involved silver substrates roughened by exposure to nitric acid. The tips would be etched by the nitric acid and would have an inherent roughness caused by the acid. No voltage was applied to the nitric acid, resulting in a slower etching process usually around 3 minutes. The total time required to etch the tips was influenced by the amount of wire immersed in the acid as that would result in a higher mass, breaking off the tip earlier than a lighter wire would. This process resulted in tips around 1.5 microns in diameter with a very long taper, resulting in a very sharp tip.
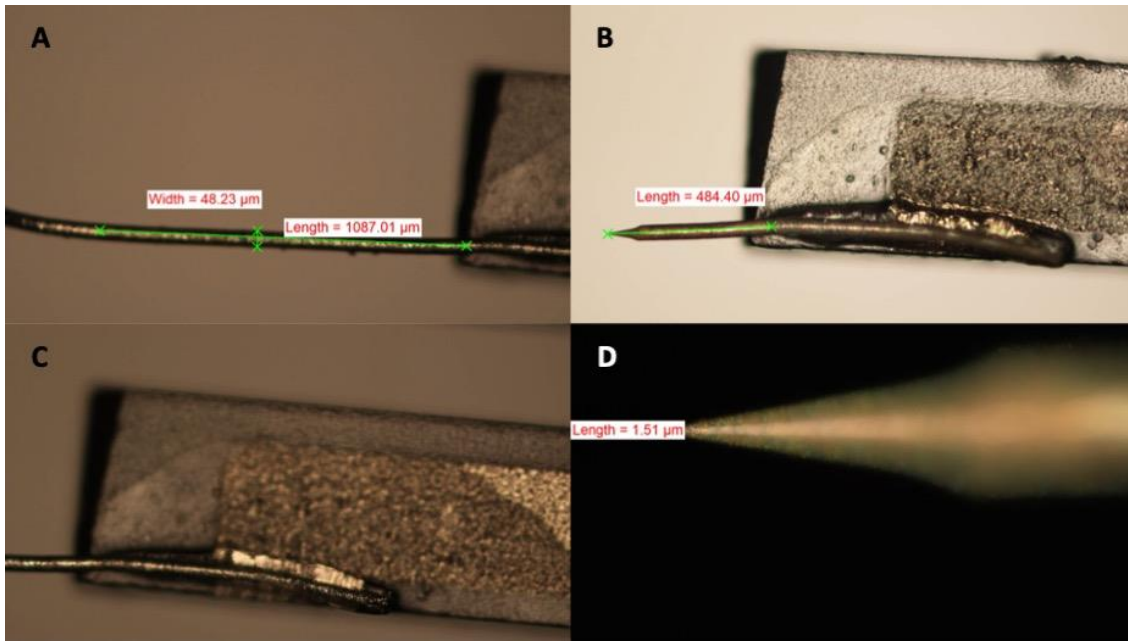
Figure 39: 1.5 Micron etched silver wire. The unetched wire is shown in A with a diameter of 48 microns and a total length exceeding 1mm. The wire is shown etched in B with the attachment point in C showing a thin layer of cyanoacrylate. The final etched tip diameter is around 1.5 microns as shown in D with a taper length around 50 microns.

During the tip etching process, a common issue appeared fouling the tip assemblies. The nitric acid was outgassing during the process, resulting in a thin layer of nitric acid on the setup. The layer caused corrosion on the leads of the assembly and caused a serious degradation of the signal.
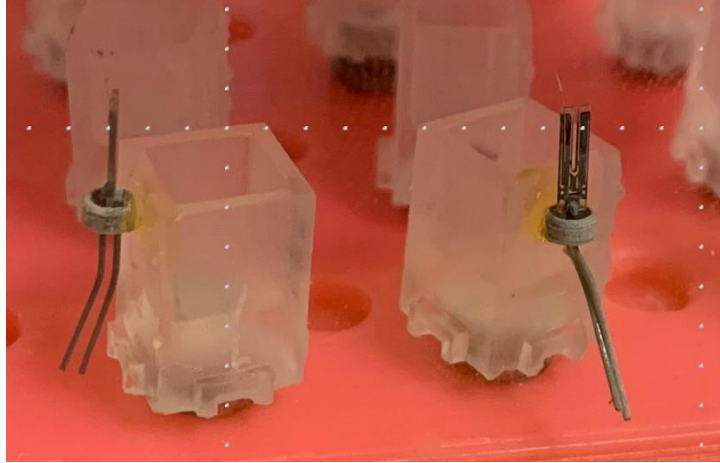
Figure 40: Nitric acid corrosion evidence on QTF assembly. The yellow discoloration of the cyanoacrylate and gray discoloration on the QTF assembly shows evidence of the nitric acid damage.

The QTF tip assemblies were magnetically attached to a damaged positioning holder that was then bolted to a one-directional micrometer as seen in Figure 41. This micrometer allowed for a stable submersion of the tips into the nitric acid which would yield a smoother surface.

Figure 41: QTF etching setup. The one-directional micrometer allows for the tips to be submerged into nitric acid at a controlled rate and at a stable depth. The tips were magnetically attached to the underside of the gray setup piece. The etching setup was a damaged early model and was thus sacrificial.

The solution to corrosion damage was to use sacrificial QTF assemblies to adhere the tips for etching instead of the final assemblies. These sacrificial QTF assemblies were previously

damaged and reused for each etching cycle as they were no longer usable for resonance response testing due to the corrosion from the acid fumes and because they were not to be used for the final assembly, we were able to attach a tip to each prong instead of just one wire per QTF. After the etching, the assemblies were dunked in deionized (DI) water several times to remove any remaining nitric acid. The cleaned tips were then adhered to the final QTF to produce the tip assembly.

## 5.	System Coding

The core of the microscope setup is the ability to bring the TERS-active tips into the range of tens of nanometers for the strongest amplification of the Raman-scattered light. The stepper motors and the piezo actuator are both controlled digitally through a custom coded program. There are several different options for the program coding such as C or C+ coding but the language chosen for this project is LabVIEW. This program was chosen because of the wide range of hardware interface drivers such as the myDAQ Student Data Acquisition Device and the native, easy to use graphic user interface (GUI). These diverse hardware interface drivers allow for an easy plug and play option for the different motors and sensors required in this build. The basics of the programming language as well as a breakdown of the command codes will be shown later in this section.

### 5.1	Resonant Frequency Sweep

The first process digitally controlled is the determination of the resonant frequency for the QTF setups. The resonant frequency is found by scanning a range of frequencies with a

signal input from a signal generator. The model in this setup, a Joy-it JDS6600 Direct Digital

Synthesis Signal Generator [66], can be controlled by proprietary software available online. This

software allows for standard single value signal generation as well as a frequency sweep

function through one of two independent outputs. The output signal's amplitude, frequency,

offset, and duty can be controlled easily in the control panel as seen in Figure 42. When

performing the frequency sweep function, the time is also modifiable, and a period of 600

seconds was chosen so that the signal analyzer was able to accurately analyze the signal from

the signal generator.
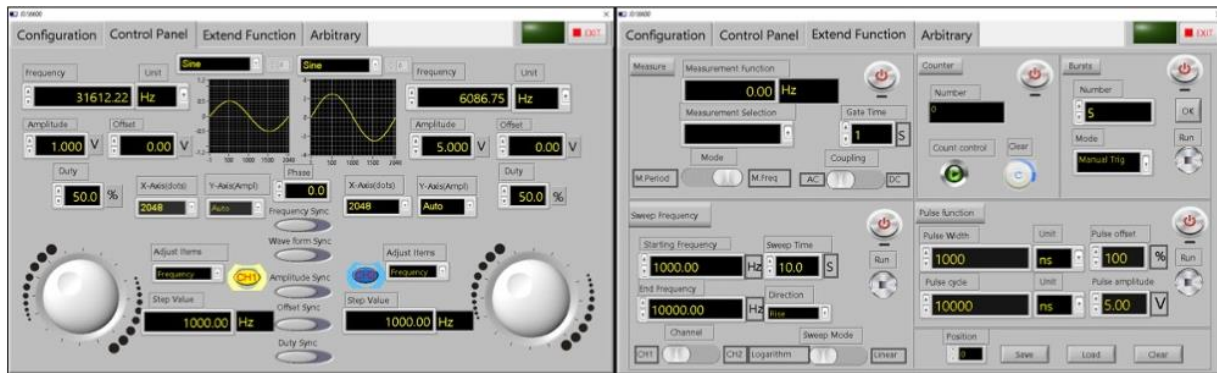
Figure 42: JDS6600 DDS Signal Generator Control Panel. The standard signal generator control panel (left) is used to generate a
single valued output signal while the signal generator function control panel (right) was used to perform customizable frequency
sweeps to determine resonant frequencies.

The output signal from the signal generator goes directly into the QTF assembly through

one prong and the second prong is directly connected to one of the myDAQ analog inputs. This

analog signal frequency and magnitude has a Fast Fourier Transform (FFT) performed on it and

the corresponding values are shown in an updating graph as shown in Figure 43. The graph

shown in the control panel is a peak hold value for each FFT frequency point so that the data

will only be overwritten if a larger magnitude value is displayed. An important note is that the

frequency analyzer has a magnitude with units of dBVrms with a reference value of 1V that all recorded values are compared against. The final resolution of the setup with a frequency sweep of 40000Hz is 12.5Hz, thankfully this results in a data point at 32,762.5Hz which is close to the QTF native, in vacuo resonant frequency of 32,768Hz.

The frequency sweep to determine the resonant frequency of the QTF-tip assembly is necessary because as mass is added to the QTF, the resonant frequency is downshifted. As each tip is handmade, the added mass is not identical for each tip and thus, the resonant frequency is different for each tip. As the QTF has a very high Q-factor, effectively how sharp the resonance response is, and so the width of the resonance frequency is very narrow. This resonance constraint is why we cannot assume the resonant frequency is close to 32,768Hz and proceed with the experiment; the narrow window requires the exact resonance frequency to be known so the later Van der Waals force interactions are observed by the further retarding of the QTF-tip resonant frequency. This shift in resonant frequency results in a smaller amplitude of vibration between the prongs and a lower voltage reading through the system.
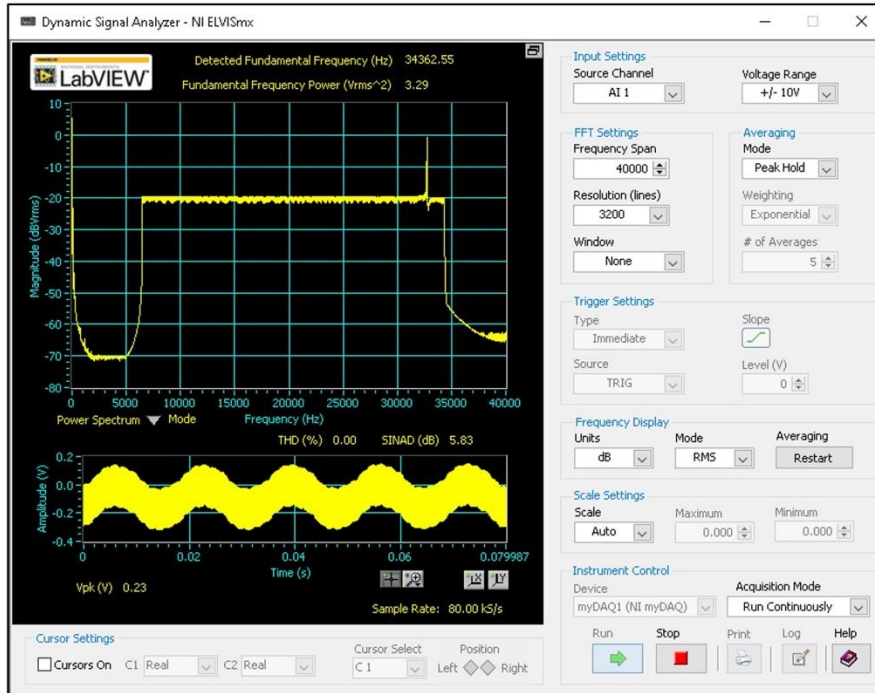
Figure 43: LabVIEW Dynamic Signal Analyzer Control Panel. The maximum resolution is shown for the FFT calculations. The resonant frequency occurs near the highest magnitude value on the top graph and generally occurs around 32762.5Hz in this FFT graph for an unmodified, in vacuo QTF.

5.2   LabVIEW Coding

LabVIEW is a visual programming language created by National Instruments and is widely used in laboratory equipment command and control programs. The program uses a front panel for GUI's and a back panel that contains the graphical programming language needed to run the GUI's or perform different commands and functions. It is possible to directly use the C-family of coding languages inside LabVIEW and those languages are generally faster than LabVIEW when performing an identical command, but the familiarity and intuitiveness of LabVIEW made it the programming language of choice for this project.

5.2.1 Functions

The basic tools used in LabVIEW to build a program and are known as functions. These functions only appear on the back panel and cannot be edited as they are the basic building blocks. Functions can be combined to perform more complex actions on a set of data and are used to also output data to an indicator, indicator terminal, or to another function. The functions exist in a palette of similar function and have a yellow background with black designs when looking at them on the block diagram screen.
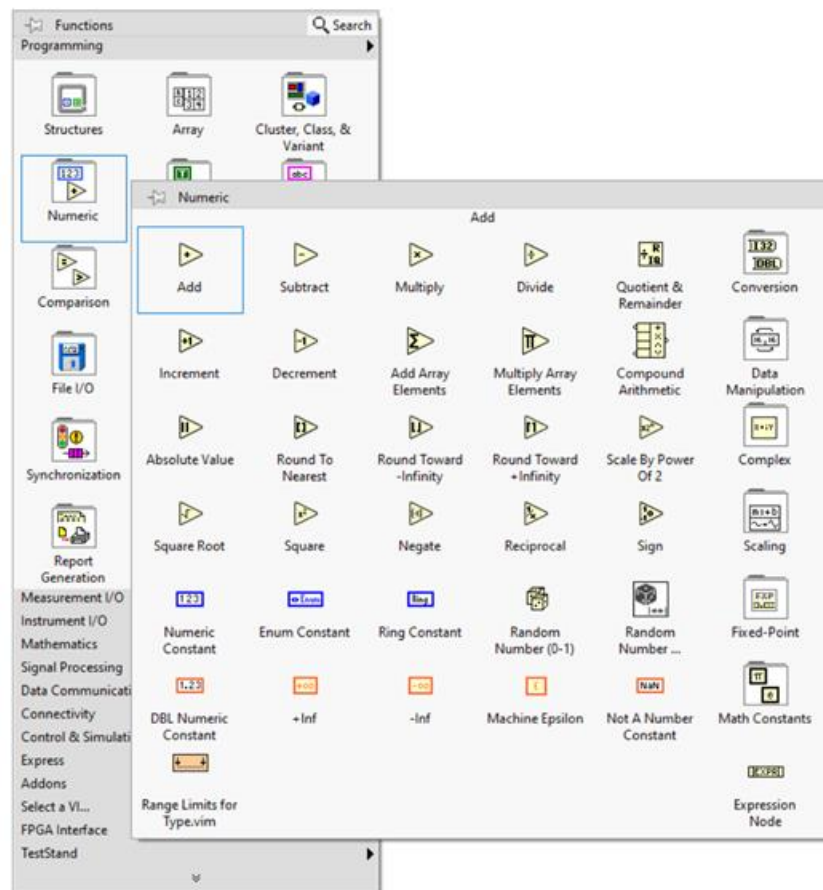
Figure 44: LabVIEW Functions Palette. The function palettes are collections of similar purpose functions. Here the basic numeric functions are shown and are represented by the yellow background with black foreground images.

5.2.2 Terminals

In LabVIEW, data can be transferred in several different types through terminals. These terminals allow data to be passed to functions, structures, or Virtual Instruments (VI) from different interactive input options on the front screen such as knobs or buttons. Terminals can also be used to show output data such as through graphs, LED's, or buttons on the front panel screen from functions, structures, or VI's.

The data passed to or from the terminals comes in four different types: numeric, Boolean, string, or cluster data types. The simplest data type of the four is a piece of Boolean data, a simple true or false. The Boolean data represents either condition with a 1 for true or a 0 for false and is fundamental to logic functions in the software such as was a new value generated for a button press. String data is named for the string or sequence of American Standard Code for Information Interchange (ASCII) characters that can either be displayed on the front panel or can be used to attach a description for data that can be sorted.
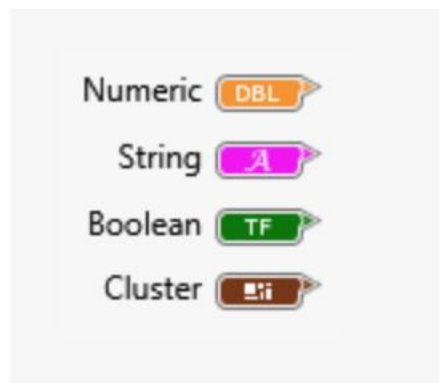
Figure 45: LabVIEW Terminal Data Types. The visual programming aspect of LabVIEW is utilized by the different colors that the four types of data are represented with. This allows for easy discernment of input or output data types. Numeric data may also be colored blue for integers.

Cluster data is a more complex data type to represent compared to Boolean or String

data. A piece of cluster data is comprised of multiple types of data, each with their own color

types to represent what is contained in the cluster on the back panel. Any cluster comprised of

only numeric data is brown, mixed data types are represented by pink cluster lines, and error

data types are yellow. Cluster data groups can be created or undone through specialized

functions or structures and allow for data to be packaged with an identifying piece of string

data and moved to a corresponding case inside a structure; this process is the core of the

created program at the heart of the TERS microscope assembly.

The numeric data type has the most variability in representation of the four types of

data. This data type is used at the most basic levels of any program, but the various types of

numeric data are not interchangeable between each other in functions. If a terminal, function,

or array requires an integer input or generates an integer output, then a single-precision

floating point numeric data type will not work. The different types of data are seen in .

Table 16: LabVIEW Numeric Data Terminal Designations. Floating-Point data is represented on the back panel by orange

number boxes and connector lines while integer data is represented by blue number boxes and connector lines. Complex data

has both real and imaginary components while signed data has either positive or negative designation in addition to the integer

value.

Terminal Design	Numeric Data Type	Storage Size (Bits)	Decimal Digits
SGL	Single-Precision, Floating Point	32	6
DBL	Double-Precision, Floating Point	64	15
EXT	Extended Precision, Floating-Point	128	15-20

CSG	Complex Single-Precision, Floating-Point	64	6
CDB	Complex Double-Precision, Floating-Point	128	15
CXT	Complex Extended-Precision, Floating-Point	256	15-20
FXP	Fixed-Point	64	User Configured
I8	Byte Signed Integer	8	2
I16	Word Signed Integer	16	4
I32	Long Signed Integer	32	9
I64	Quad Signed Integer	64	18
U8	Byte Unsigned Integer	8	2
U16	Word Unsigned Integer	16	4
U32	Long Unsigned Integer	32	9
U64	Quad Unsigned Integer	64	19
X	128-bit Time Stamp	128	19

5.2.3   Structures

The next step in complexity for coding in LabVIEW is the use of structures. These structures are representations of an execution loop that may contain functions inside. The structures perform commands on the components inside itself once conditions are matched to designated parameters. The structures available in LabVIEW are While Loops, For Loops, Sequence, Case, Event, Timed Structures, Diagram Disable, or Conditional Disable Structures.

The most basic structures to programming are While Loops and For Loops. A While Loop executes a block of code (in LabVIEW this is represented by placing the code inside the border of the While Loop structure) until a stop condition is met as shown in Figure 46. The stop condition, a Boolean data type, ends the execution loop. Data can be inputted into each iteration for the While Loop as well as the loop can output data.
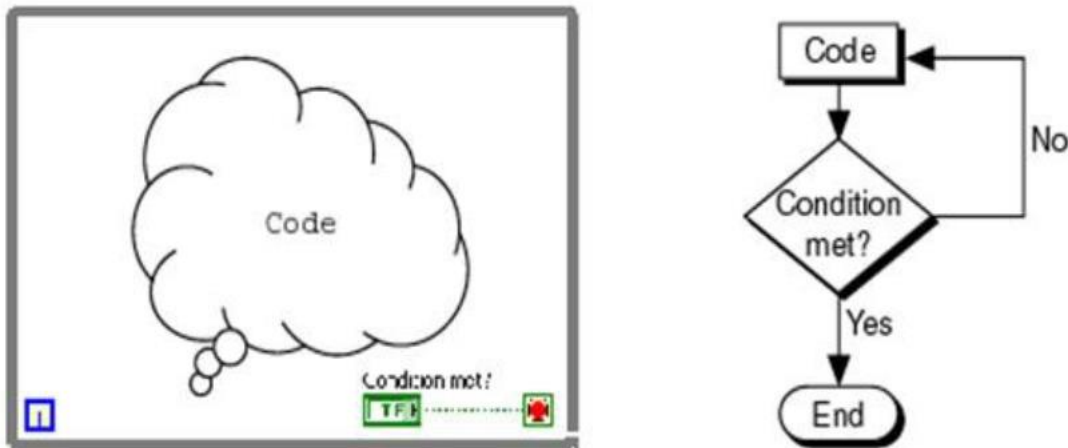
Figure 46: While Loop Representation and Flowchart. [67]

A For Loop operates similarly to a While Loop except the number of loop executions is designated by an iteration count. The For Loop executes the block code sequentially until the designated iteration count is achieved or until a programmed stop condition is achieved, whichever happens first.
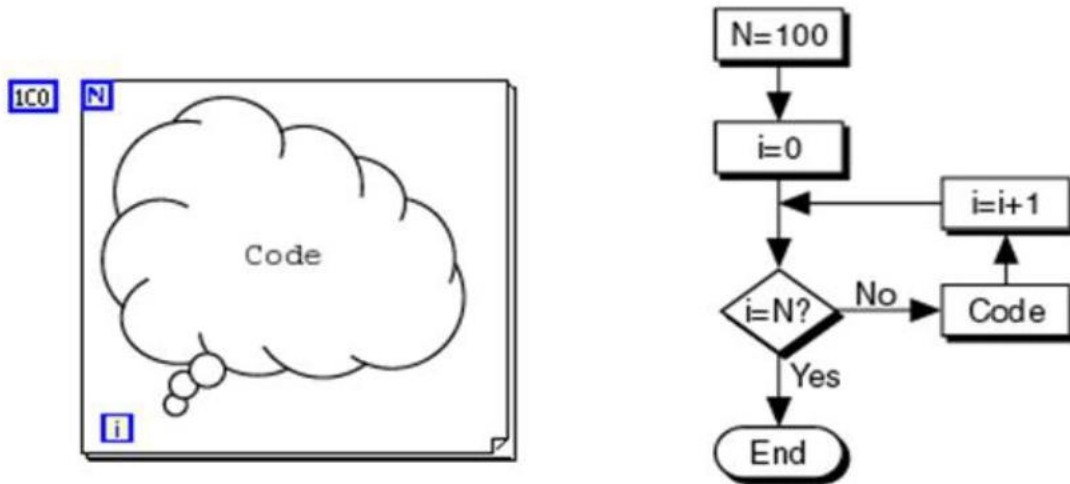
Figure 47: For Loop Representation and Flowchart. [67]

The Sequence Structure comes in three types: Flat, Stacked, or Timed Sequence

Structure. The Flat Sequence Structure (FSS) is shown on the back panel as a series of frames

like on motion camera film rolls. The program executes the code inside each frame from left to

right sequentially and data will be passed from one frame to the next until the end of the

structure. For a Stacked Sequence Structure (SSS), the operating principles are the same. The

frames are numbered and stacked on top of each other but do not pass data from previous

frames without a designated function to move it to the corresponding numbered frame. A

Timed Sequence Structure functions exactly like a FSS but utilizes a designated elapsed time as

the condition to move to the next frame in the structure. The program does not use any of the

Sequence Structure types.

A Case Structure is normally a structure contained inside another structure such as an

Event Structure. The Case Structure executes the contained code once the conditional case has

been satisfied such as with a Boolean condition or a specified numerical value is the input. The

103

Case Structure will have a unique case for each possible input condition the system may be

exposed to and performs one iteration for each input. An example of a Case Structure inside an

Event Structure can be found in Figure 48.

The Event Structure can be thought as the executive functioning of the microscope

program. The Event Structure is comprised of different Case Structures and waits until a

designated conditional event is detected shown below in Figure 48. The Event Structure then

executes the corresponding block of data and can be programmed to wait for this conditional

event either for a designated period before timing out or for an indefinite period.
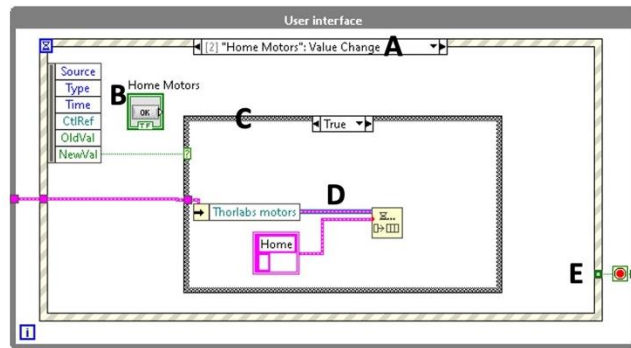
Figure 48: Event Structure Diagram. The Event Structure here is inside a While Loop and contains different Case Structures. The

event name (A) corresponds to the Front Panel input terminal (B). Once a new value is registered, the Case Structure (C) executes

the contained code (D) which is passed through a Cluster data array and passed through a queue function. The Boolean stop

condition (E) is present in every Event iteration in this program.

The Diagram Disable Structure and Conditional Disable Structure serve similar purposes

in LabVIEW by allowing for portions of the code to be disabled depending on conditions. In the

Diagram Disable Structure, only code inside the "Enabled" case will execute. The Conditional

Disable Structure functions the same way except there is a designated condition that disables a

portion of the code.

5.3   Front Panel

The published portion of a LabVIEW program and the part that the user interacts with is

known as the Front Panel. This panel can be a mixture of input terminals such as buttons or

knobs and output terminals such as graphs or video windows. The Front Panel contains no

functions but may contain sub-VI's, either user created or provided by different hardware

manufacturers.
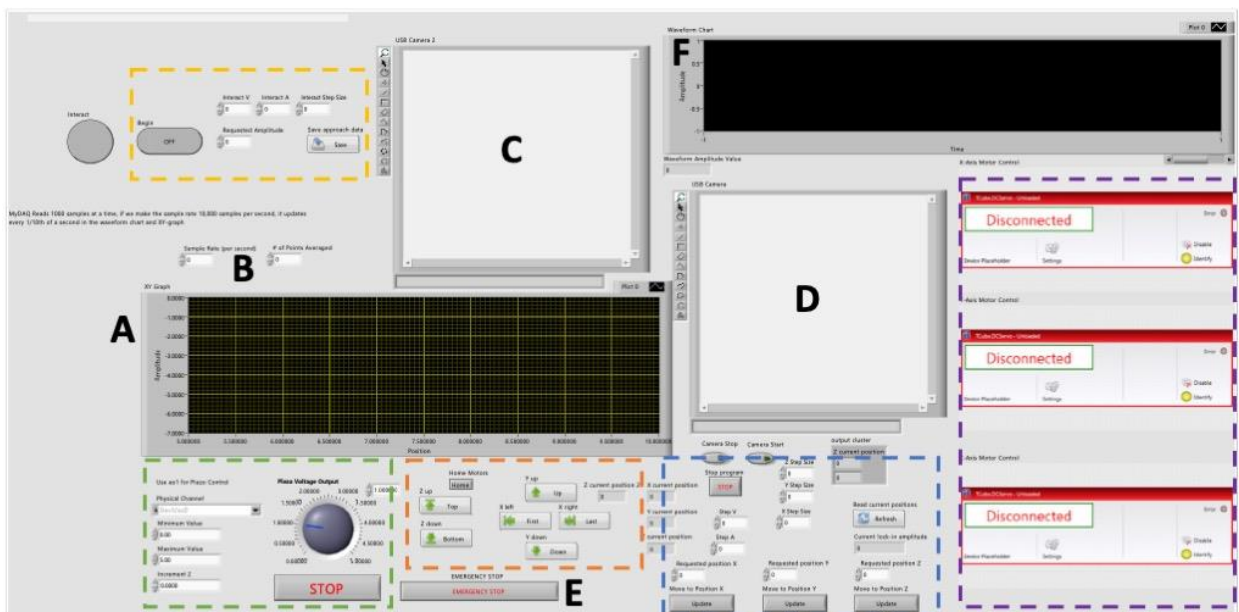
Figure 49: LabVIEW Front Panel. The graph representing the relationship between the QTF circuit voltage amplitude and the

position of the QTF in the z-axis (A) has the same data input as the graph showing the relationship between the amplitude and

the elapsed time (F). The read sample rate and number of sample points averaged together (B) are the source data for (A) and

(F). The two connected camera outputs in the setup are displayed in (C) and (D). The motor emergency stop (E) sits below the

stepper motor control terminals (dashed orange) and near the piezo actuator control (green dashed). The customization

parameters for the stepper motors as well as the position readings and move to specified position inputs are all grouped

together (blue dashed). The stepper motor manufacturer control sub-VI's (purple dashed) are onscreen as a redundancy in

control of the stepper motors. Finally, the automated feedback and movement control for the stepper motors (yellow dashed)

are in a separate area of the front panel.

5.4   Back Panel

The Back Panel in LabVIEW is the primary coding space in the programming language. In this space,

5.4.1   LabVIEW Introductory Coding

The microscope positioning and control program is an ordered program with various subcomponents that are independent of each other. A queue system is used to convey data across different control components. This queue system is generated by queue functions with an input of a cluster data consisting of a piece of string data and a piece of numeric data. The string data is used to sort the cluster data using named references (seen as iii in Figure 50) for each While Loop and the queue message handling system. The output of the queue function generates a thicker pink line seen in Figure 50. With this system, the various Boolean conditions such as button presses can be recorded, the attached conditional case can be executed, the output of that case sorted, and the data moved to a sub-component While Loop. The queue system is not a one-way process, so data generated in these While Loops such as read sample data points can be exported back into the queue system with the required String data markers to be moved to a different subcomponent.
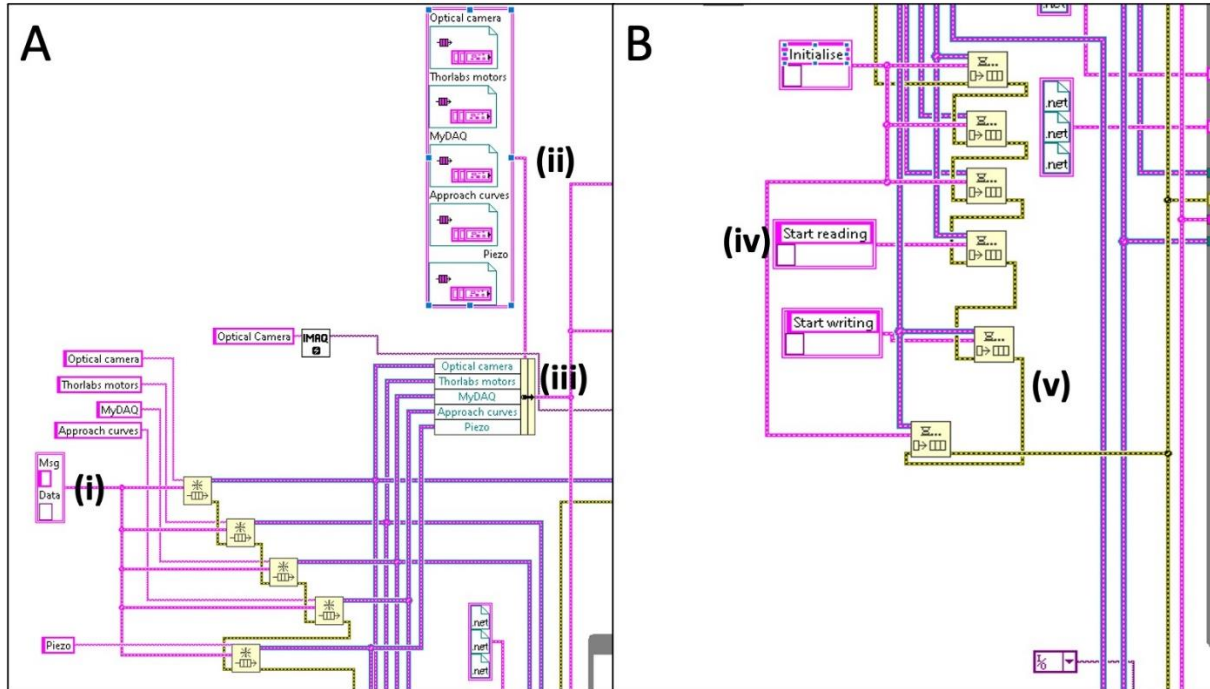
Figure 50: Cluster Data Queue System. The cluster data (thin pink line) contains a string identifier and a piece of data as defined in (i). The cluster data configuration parameters are defined in (ii) to be shape the output of the queue system data array (iii). An example of the queue message and data cluster array (iv) is shown in (B) while the error data lines (v) are all connected sequentially so that any error message will be passed forward until the end of the program.

5.4.2 Interface Controls

As the microscope positioning program is an interactive program, there must be input terminals on the Front Panel for the user to interact with. These interface controls are a series of named While Loops containing named Event Structures that then contain true/false Boolean Case Structures. These While Loops have no defined timeout period and serve to keep the program running, awaiting a change in one of the buttons on the Front Panel such as the buttons inside the dashed orange box in Figure 49.

5.4.3 Camera Coding

The first programming subcomponent is the While Loop structure for the Optical

Cameras. The While Loop has two Case Structures inside, a Start case and an Exit case. The Exit

case does not have a Boolean button attached to it but will stop the camera data acquisition

and display when the entire program is exited. The Start case relies on the Boolean "Camera

Start" button on the Front Panel which then activates a second, contained While Loop that

continuously reads and displays the camera data. This data comes from the Vision Acquisition

Assistant sub-VI that is an add-on to the standard LabVIEW programming suite. This assistant

makes it substantially easier to control cameras and output their signal to a terminal, but it is

possible to wire each individual parameter to the camera. The dual camera input exceeds

LabVIEW's ability to discern different data from the same USB plug so two different USB

terminals were used on separate USB buses to prevent the data from being lost. The visual data

acquisition and processing can be a processing sink so the "Camera Stop" button was added as

a contained Boolean off switch to free up system resources. This button would only turn off the

cameras which can then be turned back on using the "Camera Start" button again.
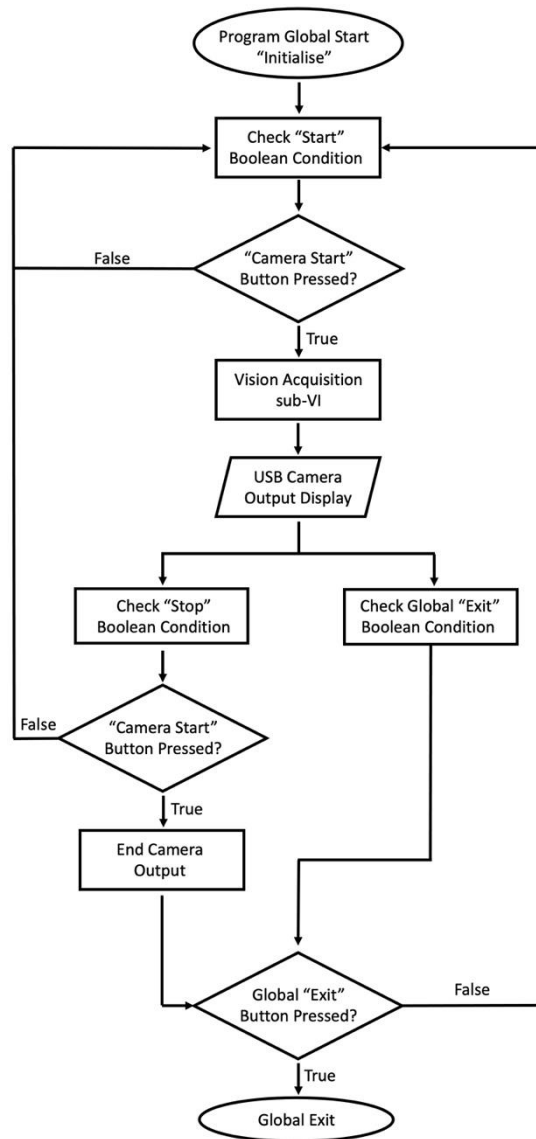
Figure 51: Optical Camera Coding Flowchart. The camera coding utilizes a series of start and stop Boolean buttons that control the Vision Assistant sub-VI. This sub-VI sets parameters for the USB camera and converts the input into a Front Panel video feed.

5.4.4   Motor Control

A program designed to control different types of motors is useless without motor control coding. The largest section of coding is used to control the stepper motors and the piezo actuator. The movement parameters of the stepper motors, shown in Figure 52, are

109

determined by a series of input terminals on the Front Panel. These terminals input numeric

data into the motor While Loop structure that is received by the respective function to

generate motor movement or to read the positioning of the motors. The motor While Loop

contains a series of named Case Structures that perform the action.
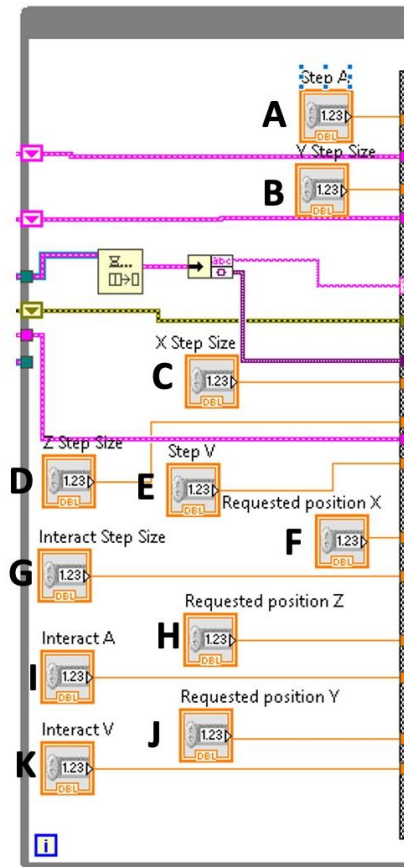
Figure 52: Motor Control Parameters Diagram. The stepper motor movement acceleration (A) and velocities (E) settings are shared by all three stepper motors. The respective axes step sizes (B,C,D) as well as requested positions (F,H,J) are all independent of each other and are displayed in centimeters. The interact parameters (G,I,K) are used by the automated approach in the z-axis using the feedback mechanism of the QTF.

The simplest cases are the initialization, spelled "Initialise" due to the system originally being

designed on a British English computer, and the "Exit" case. These cases, like for the optical

cameras, turn on the motors or shut down the motors, thus preventing further movement.

These cases are satisfied by either the startup of the program for "Initialise" or the pressing of

the end program button for "Exit".
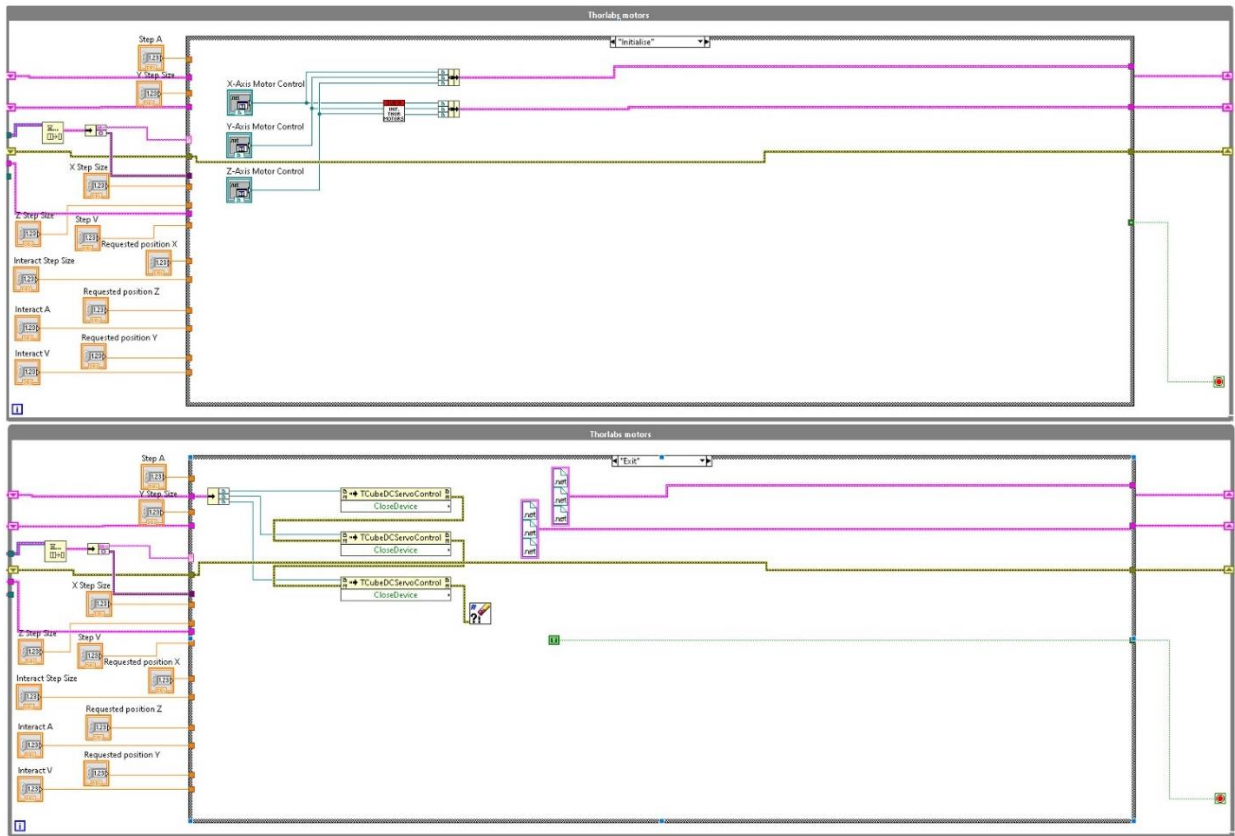
Figure 53: Initialize and Exit Administrative Case Structure. These two command Case Structures perform the initial start up of the stepper motor While Loop during the program initialization and shut down the stepper motors when the "Program Stop" button is pressed on the Front Panel.

The next two cases inside the While Loop are "Read Position" and "Emergency Stop".

The emergency stop case is used in place of the stop program for instances where damage is

111

going to occur to the setup with continued motion of the assembly. This emergency stop does

not stop all data from being collected and was put in that provides another safeguard in the

system to stop damage to either the QTF assembly or more importantly, the optical

components.
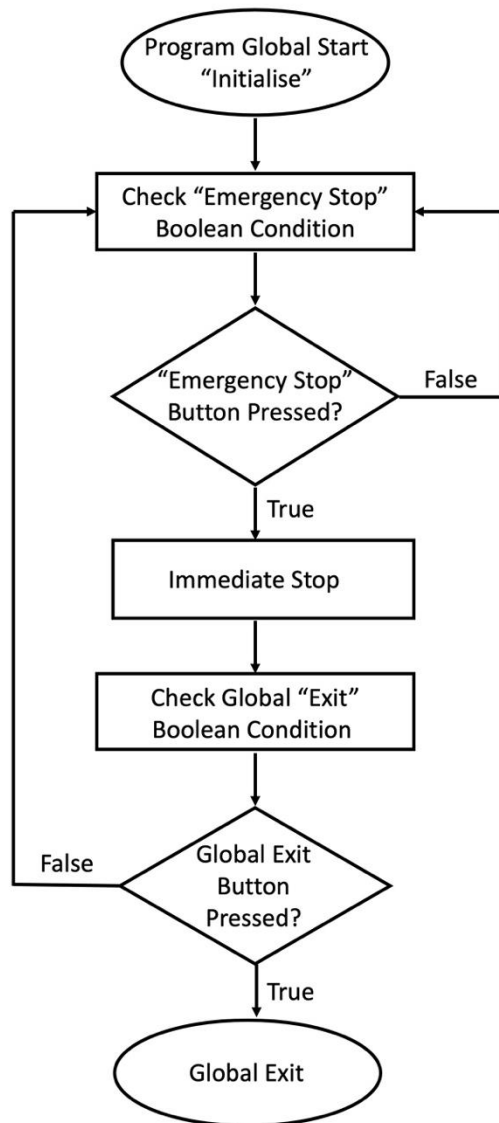
Figure 54: Emergency Stop Command Code Flowchart. This code sends an override stop command to each of the stepper motor

drivers without ending the program.

The "Read Position" button causes the case structure to immediately read the position of each

motor and send that data to output terminals that display the position in centimeters to the

Front Panel. An important note for determining position is that the encoder count is different

from the position. The encoder count must be divided by a conversion factor, shown in Figure

55 to be 24576, to generate the correct position. This conversion factor is for an older model

stepper motor, the ThorLabs Z6 series, as the software could only officially communicate with

Z6 or Z8 series motors and I had only Z7 series. The movement and encoding parameters were

identical between the Z6 and Z7 series according to ThorLabs and so the conversion factor for

Z6 series were used as there were no published conversion factors for Z7 series and the

software thought it was a Z6 motor attached.
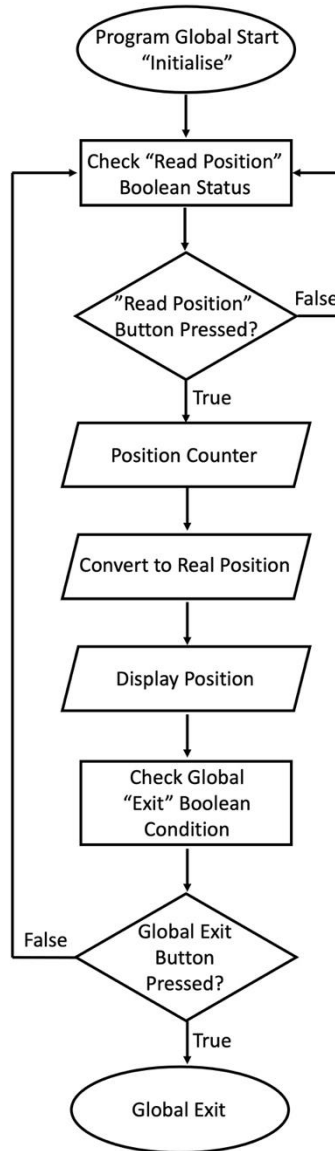
Figure 55: Read Position Command Code Flowchart. The virtual position of the stepper motor must be converted to a real position by dividing the virtual position by 24576. This value is then displayed and the code either exits or waits for the command again.

The next type of case required in the process of controlling the stepper motors is the "Home" case. This case allows the program to home all three motors simultaneously. The purpose of homing the different motors is that it allows the system to sync the physical location with the location that the software believes the motors are at. If a motor has a reported

114

position irregularity, the software will update the correct position after the motor is fully

extended and then fully retracted before moving to the correct position of 0mm. The homing

process is handled by the "Home" function provided by ThorLabs for use in their stepper

motors.
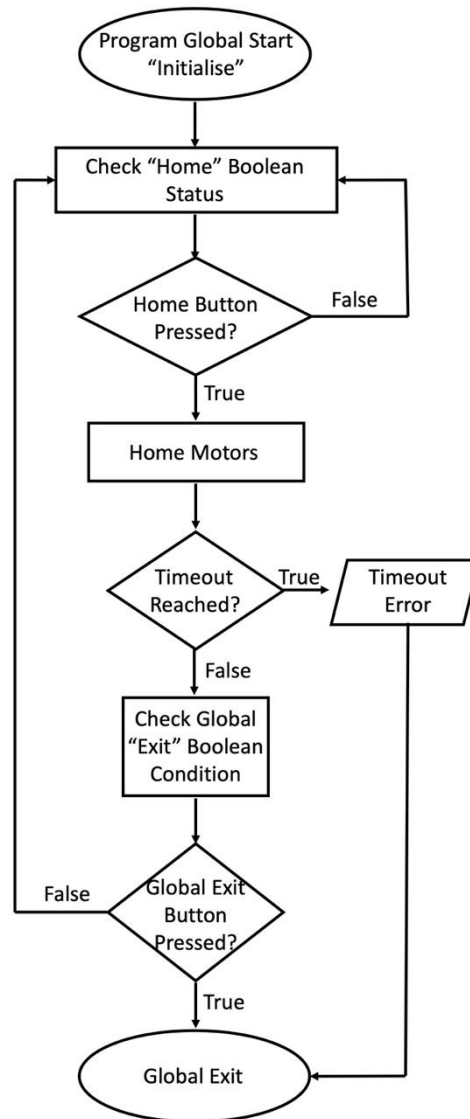
Figure 56: Home Command Code Flowchart. The "Home" command utilizes a pre-made function from ThorLabs that runs the

wired motor through the homing process. The command is wired individually to all three motors to provide homing in every axis

simultaneously.

The series of cases generalized in Figure 57 involve the operator-controlled motion of the stepper motors known as "Jog" cases. The process of completing the movement of a motor is the same for each stepper motor except the wiring will correspond to the correct terminal of the cluster array. The step size of the jog motion, the positive x-direction in this example, is determined using the Front Panel input terminal wired to (C) in Figure 52. The Front Panel input terminal displays the chosen step size in millimeters, but the motors allow for controlled, accurate step sizes of 40nm. The step size function is then wired to a function that is used to determine the movement parameters of the jog motion. Here, the velocity and acceleration Front Panel Input Terminals are used to define their respective parameters. These parameters are in units of (mm/s) and (mm/s^2) for velocity and acceleration respectively. The parameter setting function then exports these values into the "MoveJog" function that initiates the movement of the wired stepper motor. The most important distinction in this function is the "Forward" and "Backward" parameters that determine the movement direction of the corresponding stepper motor. One final note for the jog commands is there is a timeout period of 0 seconds meaning the program does not wait before allowing a second jog command to be sent to the motors.
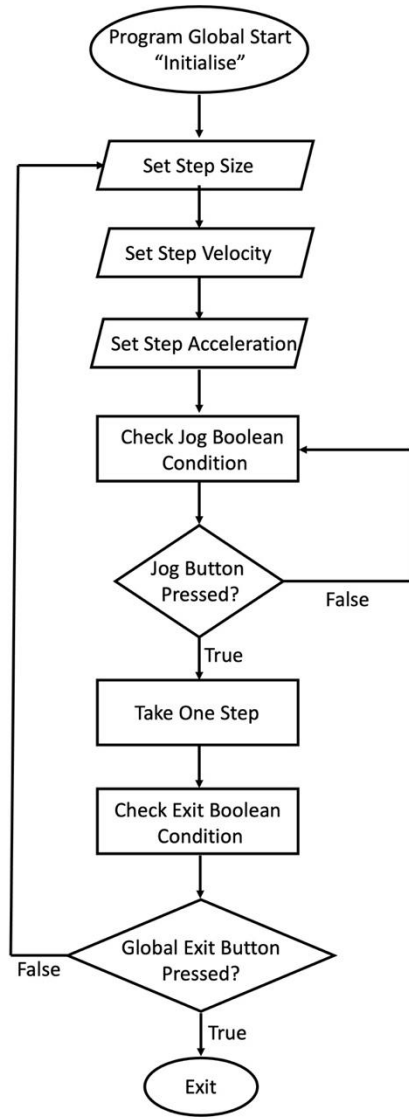
Figure 57: Jog Command Code Flowchart. The program, upon initialization, sets the jog command movement parameters of velocity, acceleration, and actual step size. The program executes one jog step per button press and then waits to run the command again or exits if the condition is satisfied.

The last general movement case for all motors is the "Move to Position" case. This case uses the "Requested position" Front Panel Input Terminals to set a desired position in millimeters. This position is fed into the "SetMoveAbsolutePosition" function provided by ThorLabs and the function exports the position into a "MoveTo" function also provided by

117

ThorLabs as seen in Figure 58-63 for each of the three Cartesian directions. This case has a

similar timeout of 0 seconds like the jog cases which allows for the immediate fine-tuning of

desired positions as well as simultaneous movement of multiple stepper motors to new

positions.
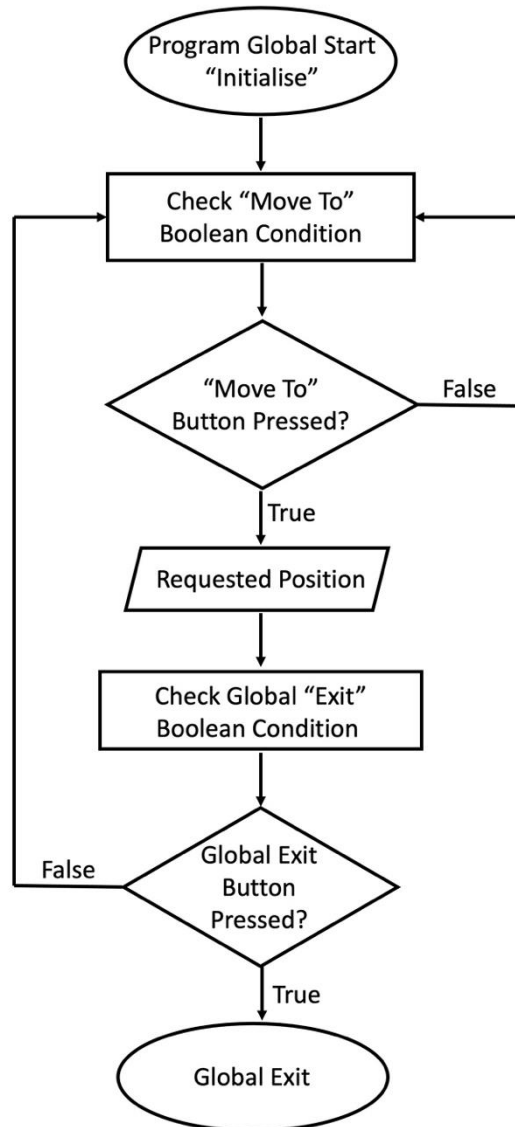
Figure 58: Z- Jog Command Code Flowchart. The "Move to Position" case structure uses an input terminal data value to input

into a set move position function. This function outputs to an absolute position function that is the input for the move to

function for the motor.

The most important programmed cases are the final two cases, "Begin" and "Interact".

The "Begin" case handles the Piezo motor control, determination of the final position of the

QTF-tip assembly, and the building of the Z-Position vs Amplitude graph. The piezo control Back

Panel diagram consists of a minimum and maximum voltage setting connected to a Front Panel

knob. This knob is also wired to an input to determine the incremental voltage steps each turn

of the knob creates. The min/max voltage values are also wired into a function that sets the

parameters of an analog output voltage signal. This in turn, is connected to a function that

creates the analog signal with the output voltage determined by the output from the Front

Panel knob voltage. The setup is wired to generate a new voltage value every 10ms which

allows the knob to be a control for the output voltage value. The output voltage value is also

used to determine the position of the piezo by multiplying the voltage value by 0.0014 and then

subtracting that from the stepper motor position. The subtraction happens because the stepper

motor positive direction is opposite of the positive direction of the piezo stack. As previously

mentioned in Section 2.2.3, the piezo has a maximum travel distance of 7μm. The myDAQ

hardware can only output a maximum value of 5V so this means there is ratio of 1.4μm/V for

movement per output volt. Since the program uses millimeters as the default scale, 1.4μm =

0.0014mm and this value is multiplied by the output voltage value, resulting in the distance of

movement by the piezo.
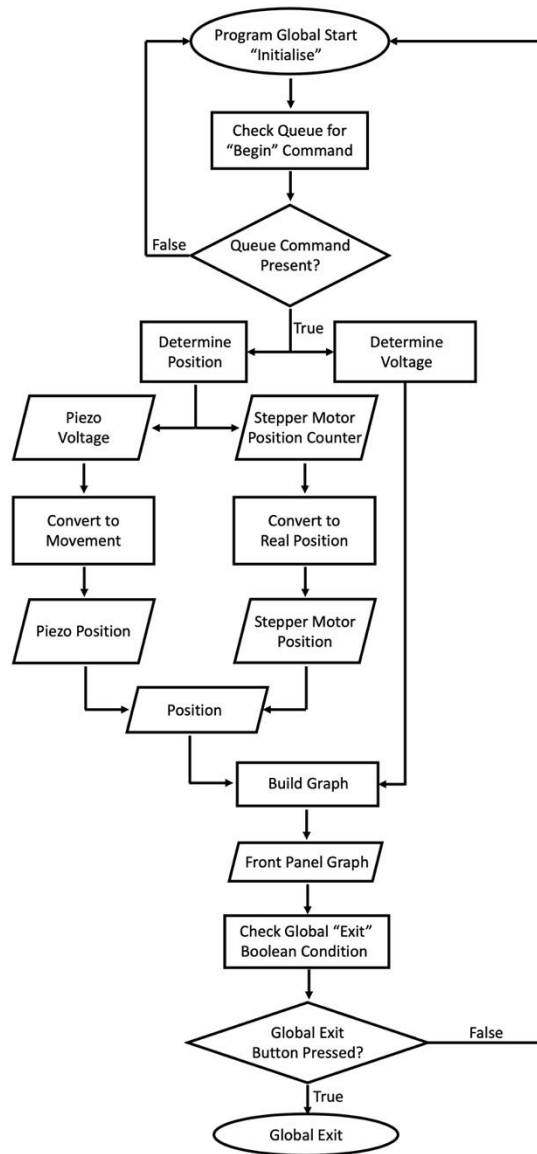
Figure 59: "Begin" Command Code Flowchart. The command executes a series of functions to convert the motors virtual position and the piezo voltage into real positions. These are combined and fed into a create graph function with the input voltage readings from the MyDAQ hardware. The graph is displayed on the Front Panel and is constantly updating every 10ms unless the global exit command is activated.

The "Interact" case is a little more straightforward than the "Begin" case. The "Interact" case is used to control the automatic movement of the stepper motors until a desired feedback voltage value from the QTF-tip assembly is reached. This case is functionally a "Jog Z-" case with

120

an added Boolean conditional for the feedback voltage value. If the requested amplitude on the Front Panel is smaller than the feedback voltage, the system takes a jog step in the negative z-direction and compares the values again. The voltage values are negative because the signal input into the myDAQ is wired to the negative terminal. This step size, determined by the "Interact" family of input terminals on the Front Panel, can be as small as 40nm but the system will generate movement with step sizes set to 25nm with less movement precision. Once the feedback value is larger than the desired amplitude, the jogging is stopped, and a more controlled movement can be manually performed with the piezo control knob input values.
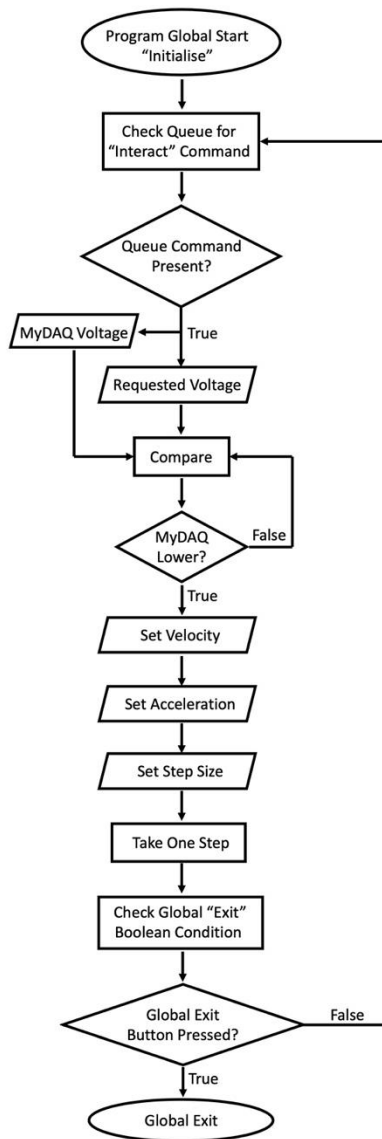
Figure 60: "Interact" Command Code Flowchart. The "Interact" command is a continuously running command in the current

setup. It compares the MyDAQ input voltage with the requested voltage amplitude and will take steps of a set value until the

requested voltage amplitude is higher than the input voltage.

5.4.5   Data Handling

The voltage values utilized by the "Interact" and "Begin" commands originate in the

MyDAQ data collection While Loop structure. The structure creates the Analog-In port to read

the voltage values from the QTF-tip assembly at the program startup when the queue

command "Initialise" is read from the queue. This case establishes the read type, continuous, and the sample buffer size, set to 1000 seconds of data.
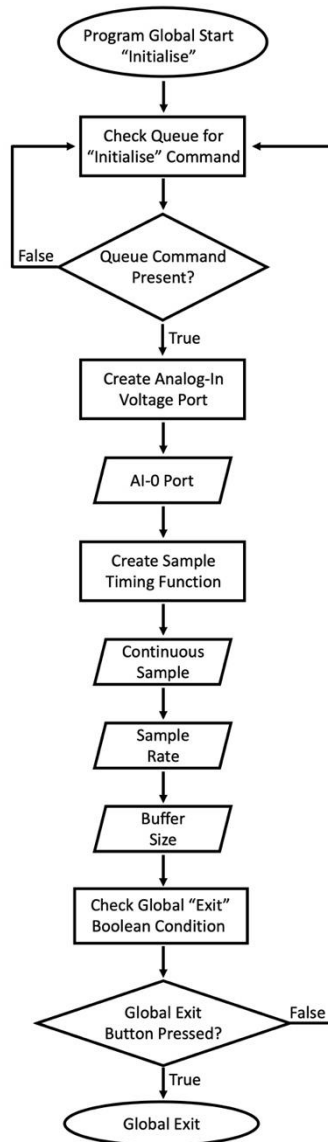
Figure 61: MyDAQ "Initialise" Command Code Flowchart. The "Initialise" command condition causes the execution of the program to create an Analog-In voltage port and establish the sample timing parameters of that port before checking for an exit condition or creating the analog-in port again if no exit command is present.

The second step in the data collection process is the "Start Reading" case structure. This step involves the initialization of the newly created Analog-In voltage port. This structure does not read the data but allows further cases to be able to access this data.
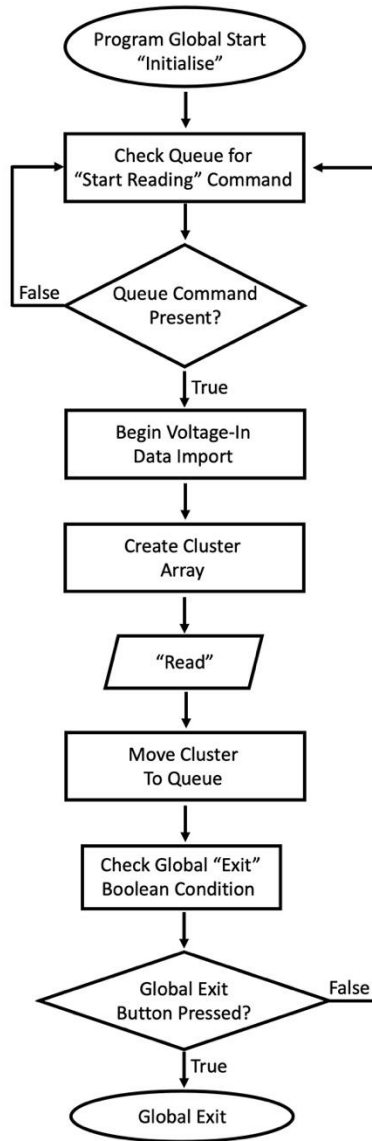
Figure 62: MyDAQ "Start Reading" Command Code Flowchart. The "Start Reading" command begins the process of importing data from the Analog-In voltage port. This loop also creates the cluster array "Read" and puts this array into the queue to begin the processing of the data from the newly established pipeline.

124

The final and most complicated case structure in the data collection process is the "Read" case. This structure reads a designated number of samples and averages them; this average is exported to a Front Panel output terminal. The data average is also exported to three build cluster array functions with the label designations: "New Amplitude", "Interact", and "Begin". The last two cluster arrays are then placed into the queue bundled with the While Loop reference name "Thorlabs motors" so that the cluster labels will activate cases inside the motor control While Loop. The "New Amplitude" cluster label is bunded with the reference name "Approach curves" to be placed into the queue with the "Approach curves" While Loop as the target location of the cluster label, activating a case there.
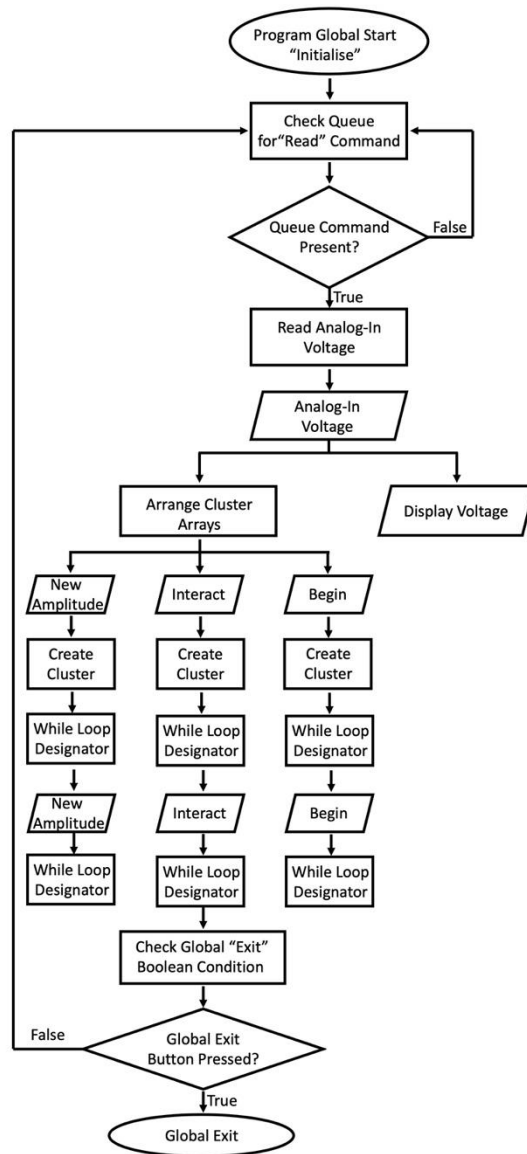
Figure 63: MyDAQ "Read" Command Code Flowchart. The "Read" command from previous "Start Reading" case causes this case to begin the reading of the Analog-In data values, averaging those values, and placing this data inside different cluster arrays. These cluster arrays are named "New Amplitude", "Interact", and "Begin" and then bundled with a While Loop designator function before being placed into the queue for export to the respective While Loops.

5.4.6 Display Areas

The simplest While Loop structure in the Back Panel is the "Approach Curves" case. This case structure receives data from the "MyDAQ data collection" While Loop, graphs the voltage

126

amplitudes as a function of time, and displays the measured voltage amplitude on the Front

Panel. This graph is displayed on the Front Panel as the "Time v Amplitude" graph. This graph

and output value display are important in the final steps of determining the resonant frequency

from the approximation determined by the FFT resonance response function from Section 5.1.
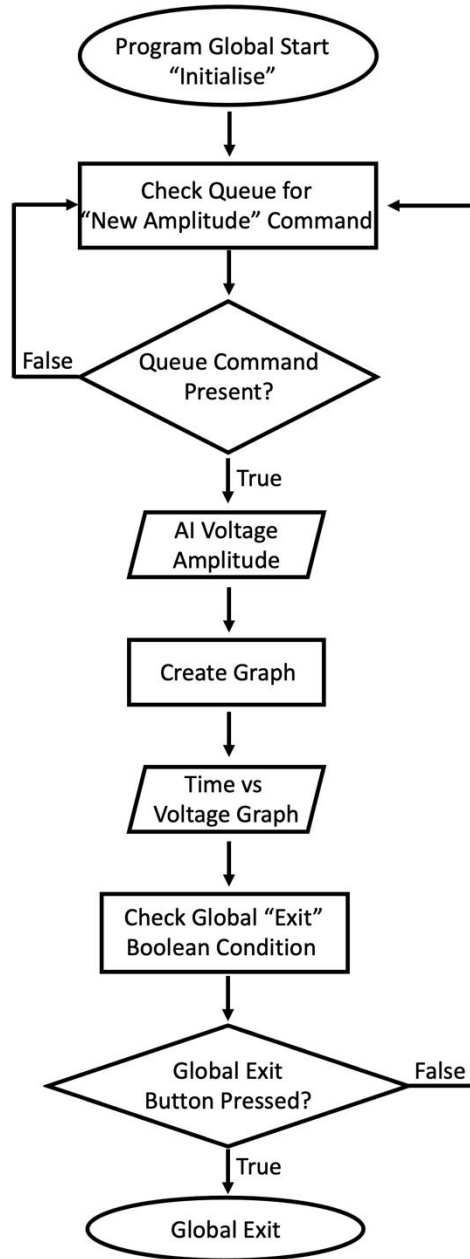
Figure 64: Approach Curve "New Amplitude" Command Code Flowchart. This While Loop imports voltage data from the MyDAQ

data collection Loop and displays this as a graph of Time v Amplitude and as an output value on the Front Panel.

6. Performance

The TERS assembly's performance is defined by the enhancement factor induced by the proximity of the TERS-active tip to the surface. The enhancement factor for a surface adsorbed analyte is a ratio of the different intensities, regular Raman and TERS, multiplied by the ratio between the two areas as shown below.

$$\text{EF} = \left(\frac{I_{TERS}}{I_{Raman}}\right) \times \frac{A_{Raman}}{A_{TERS}} \tag{6-1}$$

It is important to note that the TERS surface area is just the area directly under the tip as this is the only spot being enhanced by the tip.

6.1   Experimental Procedure

The anticipated performance parameters of the TERS system in approach requires a rigorous experimental procedure during the tip creation and the approach process. The tips are all handmade and are subject to variations during the creation process, but the procedures help to alleviate some of the disparities between the tips. The experimental procedure involves the etching of a tip separately, the modifying of a canned QTF, the combining of these two processes to create a QTF-tip assembly, the approach process, and finally the measuring and data analysis process. The first component of the experimental procedure is the tip etching process which uses a sacrificial QTF assembly as the HNO_3 solution used produces corrosive vapors that degrade the QTF prongs and leads which causes a reduction in resonance response.

Tip Etching Process:

1. Cleanly snip approximately 1cm of Silver wire (99.99%, 50μm diameter) with wire cutters

2. Adhere wire to sacrificial de-canned QTF assembly using super glue so majority of wire hangs past QTF prongs

3. Allow 24 hours to fully cure

4. Pour approximately 250mL HNO_3 (15M) into 250mL beaker

5. Magnetically attach QTF-tip assembly to submersion setup

6. Carefully lower the QTF-tip assembly until the wire is submerged in the HNO3; want approximately 25% of the overhanging wire is in the acid solution

7. Allow QTF-assembly to remain in solution until the submerged section breaks off or disappears into solution

8. Immediately raise the QTF-tip assembly and carefully remove acid beaker away from submersion assembly

9. Remove QTF-tip assembly carefully to prevent contact with the sharpened tip

10. Immediately dunk the QTF-tip assembly into DI water several times to remove any HNO_3 left on QTF-tip assembly

11. Allow assembly to air dry

The QTF modification process can happen concurrently with the tip etching process in bulk and is as follows:

QTF Assembly Production Process:

1. Measure resonance response of canned, in vacuo QTF by soldering leads to wires connected to frequency generator and MyDAQ analog in port -1

2. De-solder leads from wires

3. Breaking the QTF out of the can using gentle pressure applied by a pair of pliers just below the base of the can where the leads exit; squeeze gently and rotate slightly, repeating until there is an obvious separation between the outer can and the QTF base

4. Measure resonance response of de-canned QTF by soldering leads to wires connected to frequency generator and MyDAQ analog in port -1

5. De-solder leads from wires

6. Adhere QTF to QTF holder using an adequate amount of superglue or similar hard-curing adhesive; allow 24 hours to fully cure ambiently

7. Measure resonance response of de-canned, attached QTF by soldering leads to wires connected to frequency generator and MyDAQ analog in port -1

8. De-solder leads from wires

9. Adhere magnet (6mm diameter) into slot at the back of QTF assembly using super glue; allow 24 hours to fully cure ambiently; make sure magnet is orientated correctly to attract to the sled magnet's orientation by placing on that magnet and marking the side that will go into the slot with a sharpie

10. Measure resonance response of de-canned, attached, magnet attached QTF by soldering leads to wires connected to frequency generator and MyDAQ analog in port -1. A successful tip will maintain a resonance frequency within 100Hz of the native resonance response of the QTF

11. De-solder leads from wires

The next step in the experimental procedure is to combine the etched tip with the QTF-assembly to make the QTF-tip assembly used in the experiment, not the sacrificial setup used in the etching process.

QTF-Tip Assembly Production Process:

1. Place an extremely small amount of superglue to one prong on the QTF

2. With the sacrificial QTF-tip assembly on a surface, use a pair of very thin needle nose tweezers to grip the etched tip as close as possible to the tip without contacting the tip

3. Carefully snip the tip as close to the tweezers as possible with sharp wire cutters

4. The tip will generally temporarily adhere to one of the tweezer sides, use this adhesion to position the portion of the tip that is adhered into place on the prong with the super glue; a light amount of pressure will generally be needed to make the tip preferentially stick to the superglue over the tweezer side

5. Allow 24 hours to fully cure

6. Measure resonance response of de-canned, attached, magnet attached QTF-tip assembly by soldering leads to wires connected to frequency generator and MyDAQ analog in port -1

7. De-solder leads from wires

The approach process is the central series of tasks needed to properly make the TERS microscope setup work. This process is generally performed with the QTF-tip assemblies that have the most sensitive and thus strongest resonance responses. The approach process instructions are:

Tip Centering and Approach Limit Determination Process:

1. Solder wires onto leads

2. Start LabVIEW program

3. Home all motors

4. Fully extend z-axis motor causing the carriage to ascend to it's highest point; there larger margin of error by doing this when placing the QTF-tip assembly into position

5. Magnetically attach QTF-tip assembly to the sled bolted to the XYZ movement assembly

6. Stop LabVIEW program

7. Connect QTF-tip assembly wires; one to the frequency generator output that is shared with the lock-in amplifier reference input and one to the amplifier circuit input

8. Connect piezo actuator wires to their respective colored output wires from the piezo amplifier

9. Connect wires from Analog Out 0 and +1 to the input wires for the piezo amplifier; black wire to the AO 0 output and red wire to the AO +1 output

10. Start LabVIEW program

11. Set sample rate = 10,000 and "# of Points Averaged" = 1,000; this causes an update every 0.1s

12. Turn on frequency generator with parameters of 1V output and frequency at resonance peak according to FFT

13. Do a manual sweep around FFT resonance peak comparing amplitude values; the resonance peak should generate an amplitude between -8 and -9.5 and be the lowest amplitude value

14. Turn on supplemental white light to further illuminate the stage, position the light as close to normal to the stage surface without being blocked by the stage assembly

15. Start both cameras to obtain X-Z and Y-Z alignment

16. Maneuver tip using the X and Y jog functions to approximately the center of the objective lens

17. Begin process of lowering the tip using -Z jogging steps of a predefined value

18. Set piezo voltage to 2.5; allowing $3.5 \mu m$ of movement in either direction of z

19. Once the tip is within a few 10s of microns (tip details become visible when it enters the cone of focus for the objective lens, place the field of focus just above the surface to catch the tip early), enter a desired amplitude around +1 larger than the current read amplitude value

20. Enter the following parameters into the respective "Interact" input terminals: step size = 2.5e-5, velocity = 0.001, acceleration 0.01; at this point the program will begin taking steps

21. Turn on position monitor connected to objective lens camera

22. Once the desired amplitude is reached, the steps will stop and the piezo can be manipulated to either retract or extend the tip; an amplitude of approximately 1/3 to 1/2 of the starting amplitude value is the target (use positioning monitor to see tip approach the surface)

23. Set desired amplitude to -15 to prevent "Interact" steps from reengaging once tip is retracted

24. Mark this location both as the total z-position as well as the stepper motor z-value

25. Raise the assembly by 1mm

26. Proceed to the measurement/analysis steps

The measurement and analysis process must happen after the initial rough tri-axis positioning has happened. The data is recorded on a separate computer from the control

computer and must be exported as an Excel spreadsheet for ease of use, the native software is

Origin.

Basic Raman Signal Acquisition:

1. Move OD3 filter in laser pathway

2. Make sure door is closed and locked to prevent stray lights and accidents

3. Turn on outlet strip controlling laser, camera, and spectrometer power

4. Place mirror into vertical tower to move the image from the objective lens to the camera; rotate until surface comes into view

5. Use focusing knobs to bring the surface into view and then overfocus to just above the surface, use the Airy disk from the laser to show surface in focus and then right above surface

6. Use x-y stage manual adjusters to move target into beam

7. Remove objective lens mirror

8. Exchange OD3 filter with OD1 filter; beam is dangerous at this intensity

9. Turn on blue light lamp

10. Turn off positioning monitor, cover lock-in amplifier and piezo amplifier status lights, turn off supplemental lights, turn off room lights, and turn off LabVIEW computer monitor

11. Set acquisition parameters; low acquisition times with numerous acquisitions is preferred

12. Press start and turn off monitor; the room should be completely dark except for blue light

13. Once final acquisition is taken, turn on monitors and observe if there is an appreciable signal

14. Reposition sample, adjust acquisition parameters, and/or adjust focus as needed

Once the Raman signal is acquired for the target, the TERS signal acquisition process begins which requires fine positioning in all three directions to align the tip to the center of the laser beam.

TERS Signal Acquisition:

1. Once desired Raman response is reached, move to LabVIEW computer

2. Place OD-3.2 filter in pathway to essentially block laser from positioning camera

3. Adjust piezo voltage to 2.5V again

4. Use "Move to Position" to move the assembly to within $10 \mu m$ of previously recorded z-axis position

5. Turn on positioning monitor

6. Place objective lens mirror in position

7. Using small jogging steps in the x and y-planes, maneuver the tip into the beam

8. Set desired amplitude from the positioning process; assembly will begin taking jogging steps in the -z direction again

9. Once desired amplitude is reached, set desired amplitude to -15

10. Take a step in the +z direction of $1\mu m$; the shadow cast by the tip should be visible in the positioning monitor

11. Using small jogging steps in the x and y-planes, maneuver the tip into the beam again

12. Set desired amplitude from the positioning process; assembly will begin taking jogging steps in the -z direction again

13. Once desired amplitude is reached again, set desired amplitude to -15 again

14. Remove objective lens mirror

15. Remove OD-3.2 filter from pathway

16. Turn off positioning monitor, cover lock-in amplifier and piezo amplifier status lights, turn off supplemental lights, turn off room lights, and turn off LabVIEW computer monitor

17. Take an acquisition using the same parameters as the Raman measurement

18. Compare the two signals for enhancement; if not satisfied with the results proceed to Step 19, if satisfied then proceed to Step 20

19. Move the assembly up or down using the piezo controls to adjust the amplitude by values of ±1, taking acquisitions at each step repeating Step 18

20. Save and export as native Origin file or as an Excel file for analysis

6.2   Sulforhodamine B Results

The chosen analyte for proof of concept was Sulforhodamine B, a bright pink, fluorescent dye at normal concentrations. The compound is water soluble, stable at room

temperature, and non-aromatic in ambient conditions. This makes it an ideal analyte for the

TERS microscope because it is easy to handle, easily dries in ambient conditions, and produces a

very strong signal under illumination which allows for short acquisition times (10-80 seconds)

for an appreciable signal.
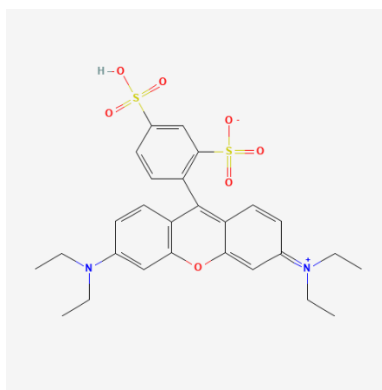
Figure 65: Sulforhodamine B Chemical Structure. [68]

Before the tip could be used in the experiment, it had to be tested every step of the

production process to make sure that there were no errors. The quality of the QTF-tip assembly

was determined by tracking the resonance frequency and the amplitude of the response. There

are a variety of factors that could degrade the resonance amplitude such as a QTF with a weak

response or adding too much mass to the system by extraneous gluing or a long silver tip.

Table 17: Resonance Frequency Comparison During Production Cycle for QTF-Tip Assembly. The table shows the resonant

frequency response from the canned QTF to the fully assembled QTF-tip assembly attached to the positioning apparatus. Note

the slight reduction in resonant frequency after attachment of the tip due to the added mass of the tip on the QTF.

	Canned	De-Canned	De-Canned, Attached	De-Canned, Attached, Magnet Attached	De-Canned, Attached, Magnet Attached, Tip Attached	Fully Assembled QTF-tip Assembly

Resonance Frequency (Hz)	32762.5	32762.5	32762.5	32762.5	32712.5	32706.0
Amplitude (dBVrms)	2.201	-1.030	-1.057	-0.448	-2.425	N/A

The tip showed a slight decrease in the real resonance frequency of the canned QTF (32,768Hz) compared to the fully assembled QTF-tip assembly that is magnetically attached to the positioning apparatus (32,706.0Hz). This is due to the added mass of the superglue and the tip on the QTF retarding the resonance frequency. By using the FFT approximation in the second to last column of 32,712.5Hz, it is much easier to manually sweep from that point to find the real resonance response in LabVIEW. The observed amplitude from the lock-in amplifier was a value of -10.5, almost the absolute minimum measurement of -10.65 that the lock-in amplifier can return. This was the most responsive QTF-tip assembly measured and thus was the most promising candidate for TERS enhancement.

Table 18: Comparison Between Two QTF-Tip Assembly Resonance Responses. Tip #55 is one of the successful tips used in the experiment while tip #32 is an example of what an unsuccessful tip resonance response looks like that failed in the final step. The QTF-tip assembly had too much glue used during the attachment process resulting in a severely retarded resonance.

	Tip #	Canned	De-Canned	De-Canned, Attached	De-Canned, Attached, Magnet Attached	De-Canned, Attached, Magnet Attached, Tip Attached	Fully Assembled QTF-tip Assembly
Resonance Frequency (Hz)	55	32762.5	32762.5	32762.5	32762.5	32712.5	32706.0
Amplitude (dBVrms)	55	3.0178	-1.030	-1.057	-0.448	-2.425	N/A

Resonance Frequency (Hz)	32	32762.5	32762.5	32762.5	32750	32500	32497.3
Amplitude (dBVrms)	32	2.4316	-1.2926	-4.5276	-2.2002	-6.2301	N/A

The graphs showing the two signal types comparison, TERS and Raman, are included in Figure 66 below. These graphs have a series of peaks, listed below in Table 19, with their respective amplitudes. The ratio between the amplitudes are also shown with an average of the ratios listed.

Table 19: TERS vs Raman Shift Peak Intensity and Position.

Peak (cm^{-1})	1169.5	1331.42	1478.99	1532.19	1562.80	1611.79
Intensity Count (TERS)	19372	24067	27368	28093	28242	31664
Intensity Count (Raman)	16807	20679	23309	23933	24145	26538
Ratio	1.1526	1.1638	1.1741	1.1738	1.1697	1.1932
Average Ratio	1.1712					
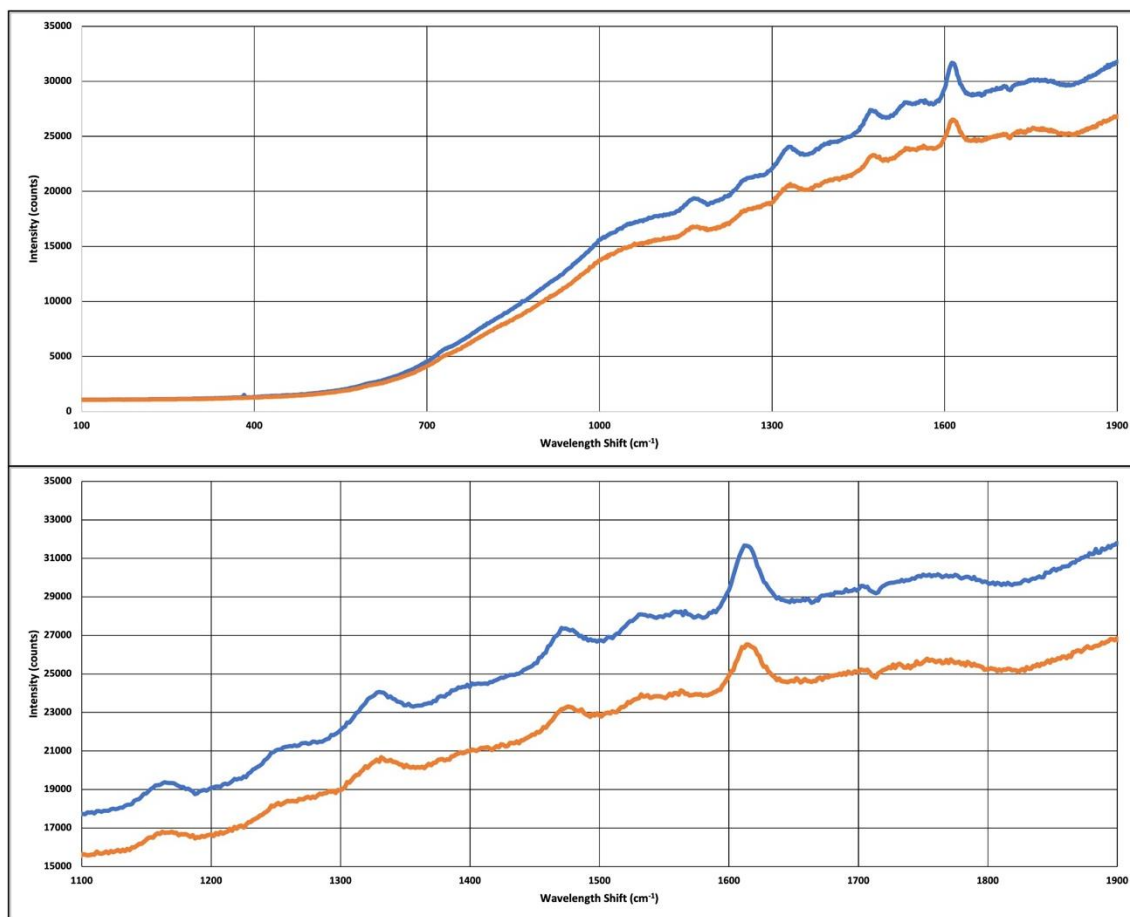
Figure 66: TERS vs Raman Shift Signal Intensity Graph. The two different graphs show the same signal with the top graph being an the entire working range of interest and the bottom graph being a more focused snapshot of the organic compound window generally 1100-1900cm^{-1}. The top line in both graphs (blue) is the TERS signal and the bottom line in both graphs (orange) is the general Raman signal. The acquisition time was 5s for both signal types.

The enhancement factor utilizes the ratio of the intensities times the ratio of the areas of enhancement as shown in (6.2). The ratio between the areas must be calculated and relies on several assumptions in the calculations. The laser beam at full, experimental brightness overwhelms the positioning camera so a linear approximation was assumed in measuring the radius of the laser beam. At a laser power of 0.05mW, the visible laser had a radius of approximately of 1µm. This approximation was from the viewing field having a radius of 25µm

142

as determined by the amount of the viewing field taken up by an unetched tip, in this case, the

entirety of the viewing field. It is important to note that the viewing field is not the entirety of

the area illuminated by the laser. When the laser power was moved to 0.5mW, the radius of the

laser spot was approximately 5µm. This shows a scaling of 5 times the radius for every 10-fold

increase in power, this leads to an illuminated area radius of 25µm for 5mW of power. This area

subject to the TERS enhancement is simply the radius of the tip in the focus field, conservatively

approximated here as 0.5µm as the etching process was refined further from the

measurements shown in Figure 39. These assumptions lead to the enhancement factor

calculations of:

$$\text{EF} = \left(\frac{I_{TERS}}{I_{Raman}}\right) \times \left(\frac{A_{Raman}}{A_{TERS}}\right) \tag{6-2}$$

$$EF = (1.1712) \times \frac{(25 \times 10^{-6}m)^2}{(0.5 \times 10^{-6}m)^2} \tag{6-3}$$

$$EF = 4280 \tag{6-4}$$

This enhancement factor, 4.28×10^3, is not in the range of the some of the previously

mentioned research groups enhancement factors of 10^5-10^7. Those groups utilized much

sharper tips, a radius in the range of 50-100nm while our tip had a radius of 500nm. If we

assume that the actual tip radius in the amplified field is much smaller than what we could

measure since the focal range of the objective lens is several microns tall, we could drop from

radius of 500nm to a 50nm radius. Using the same calculations in (6-3) would result in an

enhancement factor of 4.28×10^5. A silver tip synthesis process by Bin Ren et. al. created 50

reproducible silver tips with a radius of curvature of 58nm using an electrochemical etching

method in a bath of anhydrous ethanol and perchloric acid [69]. Another research group, Chen et. al., used an electrochemical etching process using a concentrated ammonia solution as the electrolyte bath [70]. This group was able to achieve a tip radius consistently under 100nm.

In summary, the enhancement factor demonstrated allows for the user to identify, by enhanced Raman signal, single molecules. This setup is designed to be used with biological samples deposited inside the liquid well and analyzed with a 532nm wavelength laser. The positioning system was shown to be able to move a fabricated tip within range for the TERS phenomenon to occur, in the range of 10-40nm. This designed system allows a user to take a functional Raman setup and upgrade that system to be able to perform TERS measurements on biological samples. This system could be used in low temperature, in vacuo conditions for example to produce a cleaner signal or it could be used in heated conditions to replicate body temperature studies for biological samples. The final confirmation of the success for the designed system is a price point comparison between this system and commercially available systems.

6.3   Cost Comparison

To be considered a low-cost alternative to a commercial TERS setup, the total cost of the system must be determined with the assumption that the user already has a functional conventional Raman setup or a SERS setup. This assumption includes a higher power objective lens, ideally 63x or higher, to allow for a more exact positioning of targeted regions of the sample under the QTF-tip assembly. All price points are for the exact components used in the setup unless that device is no longer available, then the next best device is chosen.

144

Component	Quantity Needed	Price (USD)/each
MyDAQ Acquisition Hardware	1	483.00 [71]
Thorlabs Z812B 12mm Motorized Actuator	3	717.41 [72]
KDC101 Brushed DC Servo Motor Controller	3	757.51 [73]
PiezoDrive 150V Piezo Stack Actuator (SA050510)	1	61.00 [74]
PiezoDrive PD200 60W Voltage Amplifier	1	1980.00 [75]
Stanford Research SR-530 Analog Lock-In Amplifier	1	2595.00 [76]
XYZ Aluminum Linear Stage	1	1148.00 [77]

The listed components are all the individual components necessary to create the TERS system.

A composite price breakdown of all the individual systems is listed below.

Table 21: Composite Price Breakdown of TERS System

Needed components	Cost (USD)
Acquisition Hardware	3078.00
Stepper Hardware	4424.76
Piezo Hardware	2041.00
Linear State	1148.00
Total:	10691.76

The total price point of $10,691.76 (USD) is not an insignificant amount of money but the parts are sourced individually which helps to drive down the price compared to a commercial setup. I have selected several similar TERS commercial setups to compare pricing.

System	Manufacturer	Price (USD)
LS AFM	AFMWorkshop	$58,945.00 - 145,500.00 [78]
WiTech Alpha 300 RS	Oxford Instruments	$378,210.00 [79]

It is apparent that the commercial systems are significantly more expensive compared

to the system I developed. The commercial systems will be much more precise and sensitive

than the developed system, but the developed system is not designed to compete with

nanometer resolution commercial systems as it sits above that resolution limit as an affordable

option for the first forays into tip-enhanced Raman spectroscopy applications. As a low-cost,

micron-scale resolution TERS system designed for a variety of applications, this project is a

success.

7.   Future Works

The microscope project has several potential upgrades that could improve the functionality of the setup. The first primary series of upgrades would be to improve the etching process to generate a sharper tip. This could be achieved by chilling the nitric acid, increasing the surface tension. This would allow the meniscus to climb higher up the intersecting wire, generating a sharper tip. The electrochemical etching processes previously mentioned in Section 4.3 could be adapted to produce significantly sharper tips at a higher cost.

The positioning components could also be upgraded. The stepper motors could be swapped out for newer motors that interface more natively with LabVIEW, resulting in more consistent, smaller steps than the 40nm resolution the system currently can make. For instance, the ThorLabs Z8 Series Motorized Servo Actuators have a step resolution of 29nm [80]. The sled bridge that the piezo actuator stack fits into could be machined from metal, by CNC or wire-erosion, to produce a thinner bridge. This bridge would deform less around the actuator which would allow for more consistent movements throughout the total range of motion. Finally, the voltage output to the piezo amplifier and the piezo amplifier itself could be reconfigured to allow for an output that allows for the full range of motion according to the piezo actuator manual.

The TERS microscope setup can be used in further proof of concept experiments using known reference samples. As stated in the proposal, a convenient reference sample would be paraffin wax. This reference sample would be useful for having the paraffin wax spectra present at different acquisition times resulting in different intensity counts so that if there is any

paraffin wax contamination in future biological samples, it becomes much easy to subtract the wax spectra from the biological sample spectra. A final proof of concept for the setup would be the analysis of propylene carbonate. This oil compound would be closer to the lipid surfaces of organic molecules and provides a much different test surface than dried Sulforhodamine B. The two potential reference samples have very distinct Raman spectra which will allow for easy identification.

The application of a single molecule identification system is limited by the imagination of the researcher. For example, if the presence of the X or Y chromosome in sperm cells is detectable by the amplified Raman signal in humans as it is in cows, then it could be possible to identify and sort sperm cells by the desired chromosome [81]. Another biological application could be using TERS systems to rapidly determine the presence of individual cancer cells in biopsied tissues [82]. A final biological application could be the target studying the location of antibodies on the surface of cells by the presence or lack of the antibody's TERS signal.

References

[1] A. Smekal, *Zur Quantentheorie Der Dispersion*, Naturwissenschaften **11**, 873 (1923).

[2] C. V. Raman, *A New Type of Secondary Radiation*, Nature **121**, 501 (1928).

[3] mars.nasa.gov, *SHERLOC for Scientists - NASA*,

https://mars.nasa.gov/mars2020/spacecraft/instruments/sherloc/for-scientists/.

[4] A. C. Albrecht, *On the Theory of Raman Intensities*, The Journal of Chemical Physics **34**, 1476

(1961).

[5] J. R. Ferraro, K. Nakamoto, and C. W. Brown, *Introductory Raman Spectroscopy*, 2nd ed

(Academic Press, Amsterdam ; Boston, 2003).

[6] Swanson, D.G., *Quantum Mechanics: Foundations and Applications* (Taylor & Francis, New

York, 2007).

[7] M. Fleischmann, P. J. Hendra, and A. J. McQuillan, *RAMAN SPECTRA OF PYRIDZNE*

ADSORBED AT A SILVER ELECTRODE, CHEMICAL PHYSICS LETTERS **26**, 4 (1974).

[8] M. G. Albrecht and J. A. Creighton, *Anomalously Intense Raman Spectra of Pyridine at a*

Silver Electrode, Journal of the American Chemical Society **99**, 5215 (1977).

[9] P. B. Johnson and R. W. Christy, *Optical Constants of the Noble Metals*, Physical Review B **6**,

4370 (1972).

[10]   T. Tan, C. Tian, Z. Ren, J. Yang, Y. Chen, L. Sun, Z. Li, A. Wu, J. Yin, and H. Fu, *LSPR-*

Dependent SERS Performance of Silver Nanoplates with Highly Stable and Broad Tunable

LSPRs Prepared through an Improved Seed-Mediated Strategy, Phys. Chem. Chem. Phys. **15**,

21034 (2013).

[11]   A. Henglein, *Formation and Absorption Spectrum of Copper Nanoparticles from the Radiolytic Reduction of Cu(CN) $_2^-$*, J. Phys. Chem. B **104**, 1206 (2000).

[12]   C. Silva, J. M. P. Coelho, A. Ruivo, and A. P. de Matos, *Infrared Nanosecond Laser Effects on the Formation of Copper Nanoparticles*, Materials Letters **64**, 705 (2010).

[13]   Y. Q. He, S. P. Liu, L. Kong, and Z. F. Liu, *A Study on the Sizes and Concentrations of Gold Nanoparticles by Spectra of Absorption, Resonance Rayleigh Scattering and Resonance Non-Linear Scattering*, Spectrochimica Acta Part A: Molecular and Biomolecular Spectroscopy **61**, 2861 (2005).

[14]   T. A. El-Brolossy, T. Abdallah, M. B. Mohamed, S. Abdallah, K. Easawi, S. Negm, and H. Talaat, *Shape and Size Dependence of the Surface Plasmon Resonance of Gold Nanoparticles Studied by Photoacoustic Technique*, Eur. Phys. J. Spec. Top. **153**, 361 (2008).

[15]   N. M. Saleh and A. A. Aziz, *Simulation of Surface Plasmon Resonance on Different Size of a Single Gold Nanoparticle*, J. Phys.: Conf. Ser. **1083**, 012041 (2018).

[16]   P. Chapagain, G. Guisbiers, M. Kusper, L. D. Geoffrion, M. Benamara, A. Golden, A. Bachri, and L. Hewavitharana, *Tuning the Surface Plasmon Resonance of Gold Dumbbell Nanorods*, ACS Omega **6**, 6871 (2021).

[17]   X. Wang and Y. Cao, *Characterizations of Absorption, Scattering, and Transmission of Typical Nanoparticles and Their Suspensions*, Journal of Industrial and Engineering Chemistry **82**, 324 (2020).

[18]   C. M. Cobley, S. E. Skrabalak, D. J. Campbell, and Y. Xia, *Shape-Controlled Synthesis of Silver Nanoparticles for Plasmonic and Sensing Applications*, Plasmonics **4**, 171 (2009).

[19]   K.-C. Lee, S.-J. Lin, C.-H. Lin, C.-S. Tsai, and Y.-J. Lu, *Size Effect of Ag Nanoparticles on Surface Plasmon Resonance*, Surface and Coatings Technology **202**, 5339 (2008).

[20]   B. Mehrdel and A. A. Aziz, *The Sensitivity of Surface Plasmon Resonance Damping for Colloidal Silver Nanoparticles*, J. Phys.: Conf. Ser. **1083**, 012042 (2018).

[21]   V. Bonu, A. Das, A. K. Sivadasan, A. K. Tyagi, and S. Dhara, *Invoking Forbidden Modes in SnO2 Nanoparticles Using Tip Enhanced Raman Spectroscopy*, Journal of Raman Spectroscopy **46**, 1037 (2015).

[22]   C.-F. Wang, Z. Cheng, B. T. O'Callahan, K. T. Crampton, M. R. Jones, and P. Z. El-Khoury, *Tip-Enhanced Multipolar Raman Scattering*, J. Phys. Chem. Lett. **11**, 2464 (2020).

[23]   A. Hadj Youssef, J. Zhang, A. Ehteshami, G. Kolhatkar, C. Dab, D. Berthomieu, A. Merlen, F. Légaré, and A. Ruediger, *Symmetry-Forbidden-Mode Detection in SrTiO $_3$ Nanoislands with Tip-Enhanced Raman Spectroscopy*, J. Phys. Chem. C **125**, 6200 (2021).

[24]   K. Kroth, P. Klement, L. Chen, S. Chatterjee, and P. J. Klar, *Microscopic Origin of Near- and Far-Field Contributions to Tip-Enhanced Optical Spectra of Few-Layer MoS $_2$*, Nanoscale **13**, 17116 (2021).

[25]   S. Mignuzzi, N. Kumar, B. Brennan, I. S. Gilmore, D. Richards, A. J. Pollard, and D. Roy, *Probing Individual Point Defects in Graphene via Near-Field Raman Scattering*, Nanoscale **7**, 19413 (2015).

[26]   J. Stadler, T. Schmid, and R. Zenobi, *Nanoscale Chemical Imaging of Single-Layer Graphene*, ACS Nano **5**, 8442 (2011).

[27]   Y. Saito, P. Verma, K. Masui, Y. Inouye, and S. Kawata, *Nano-Scale Analysis of Graphene Layers by Tip-Enhanced near-Field Raman Spectroscopy*, Journal of Raman Spectroscopy **40**, 1434 (2009).

[28]   R. H. Rickman and P. R. Dunstan, *Enhancement of Lattice Defect Signatures in Graphene and Ultrathin Graphite Using Tip-Enhanced Raman Spectroscopy*, Journal of Raman Spectroscopy **45**, 15 (2014).

[29]   S. Kawata and V. M. Shalaev, editors , *Tip Enhancement* (Elsevier, Amsterdam ; Boston, 2007).

[30]   T.-X. Huang et al., *Rational Fabrication of Silver-Coated AFM TERS Tips with a High Enhancement and Long Lifetime*, Nanoscale **10**, 4398 (2018).

[31]   M. Moretti, G. Das, B. Torre, M. Allione, and E. Di Fabrizio, *Tip Enhanced Raman Spectroscopy of Rhodamine 6G on Nanostructured Gold Substrate*, Optics and Lasers in Engineering **76**, 52 (2016).

[32]   X. You, C. B. Casper, E. E. Lentz, D. A. Erie, and J. M. Atkin, *Fabrication of a Biocompatible Mica/Gold Surface for Tip-Enhanced Raman Spectroscopy*, ChemPhysChem **21**, 188 (2020).

[33]   A. Krayev, S. Krylyuk, R. Ilic, A. R. Hight Walker, A. Bhattarai, A. G. Joly, M. Velický, A. V. Davydov, and P. Z. El-Khoury, *Comparable Enhancement of TERS Signals from WSe $_2$ on Chromium and Gold*, J. Phys. Chem. C **124**, 8971 (2020).

[34]   W. Zhang, B. S. Yeo, T. Schmid, and R. Zenobi, *Single Molecule Tip-Enhanced Raman Spectroscopy with Silver Tips*, J. Phys. Chem. C **111**, 1733 (2007).

[35]   B. Pettinger, P. Schambach, C. J. Villagómez, and N. Scott, *Tip-Enhanced Raman Spectroscopy: Near-Fields Acting on a Few Molecules*, Annu. Rev. Phys. Chem. **63**, 379 (2012).

[36]   E. A. Pozzi et al., *Ultrahigh-Vacuum Tip-Enhanced Raman Spectroscopy*, Chem. Rev. **117**, 4961 (2017).

[37]   E. C. Le Ru, E. Blackie, M. Meyer, and P. G. Etchegoin, *Surface Enhanced Raman Scattering Enhancement Factors: A Comprehensive Study*, J. Phys. Chem. C **111**, 13794 (2007).

[38]   N. Kumar, W. Su, M. Veselý, B. M. Weckhuysen, A. J. Pollard, and A. J. Wain, *Nanoscale Chemical Imaging of Solid–Liquid Interfaces Using Tip-Enhanced Raman Spectroscopy*, Nanoscale **10**, 1815 (2018).

[39]   S.-C. Huang, J.-Z. Ye, X.-R. Shen, Q.-Q. Zhao, Z.-C. Zeng, M.-H. Li, D.-Y. Wu, X. Wang, and B. Ren, *Electrochemical Tip-Enhanced Raman Spectroscopy with Improved Sensitivity Enabled by a Water Immersion Objective*, Anal. Chem. **91**, 11092 (2019).

[40]   N. Martín Sabanés, L. M. A. Driessen, and K. F. Domke, *Versatile Side-Illumination Geometry for Tip-Enhanced Raman Spectroscopy at Solid/Liquid Interfaces*, Anal. Chem. **88**, 7108 (2016).

[41]   D. Bloch, *Testing the Distance-Dependence of the van Der Waals Interaction*, (n.d.).

[42]   *The Measurement of van Der Waals Dispersion Forces in the Range 1.5 to 130 Nm*, https://doi.org/10.1098/rspa.1972.0162.

[43]   S. Takahashi, *Longitudinal Mode Multilayer Piezoceramic Actuators*, Ceramic Bulletin **65**, 1156 (1986).

[44]   S. Wise and M. Hooker, Characterization of Multilayer Piezoelectric Actuators for Use in Active Isolation Mounts, Technical Memorandum No. 4742, National Aeronautics and Space Administration, 1997.

[45]   *IHR_Series_Brochure.Pdf*, (n.d.).

[46]   J.-M. Friedt and É. Carry, *Introduction to the Quartz Tuning Fork*, American Journal of Physics **75**, 415 (2007).

[47]   Rychen, *Piezoelectric Quartz Tuning Forks for Scanning Probe Microscopy*, Nanonis (2005).

[48]   *Tip Recycling for Atomic Force Microscopy-Based Tip-Enhanced Raman Spectroscopy*, https://doi.org/10.1177/0003702820916234.

[49]   B. R. Wood, E. Bailo, M. A. Khiavi, L. Tilley, S. Deed, T. Deckert-Gaudig, D. McNaughton, and V. Deckert, *Tip-Enhanced Raman Scattering (TERS) from Hemozoin Crystals within a Sectioned Erythrocyte*, Nano Lett. **11**, 1868 (2011).

[50]   T. Umakoshi, K. Kawashima, T. Moriyama, R. Kato, and P. Verma, *Tip-Enhanced Raman Spectroscopy with Amplitude-Controlled Tapping-Mode AFM*, Sci Rep **12**, 12776 (2022).

[51]   J. Hübner, T. Deckert-Gaudig, J. Glorian, V. Deckert, and D. Spitzer, *Surface Characterization of Nanoscale Co-Crystals Enabled through Tip Enhanced Raman Spectroscopy*, Nanoscale **12**, 10306 (2020).

[52] P. Walke, Y. Fujita, W. Peeters, S. Toyouchi, W. Frederickx, S. De Feyter, and H. Uji-i, *Silver Nanowires for Highly Reproducible Cantilever Based AFM-TERS Microscopy: Towards a Universal TERS Probe*, Nanoscale **10**, 7556 (2018).

[53] T. Shibata, H. Furukawa, Y. Ito, M. Nagahama, T. Hayashi, M. Ishii-Teshima, and M. Nagai, *Photocatalytic Nanofabrication and Intracellular Raman Imaging of Living Cells with Functionalized AFM Probes*, Micromachines **11**, 495 (2020).

[54] L. Meng, T. Huang, X. Wang, S. Chen, Z. Yang, and B. Ren, *Gold-Coated AFM Tips for Tip-Enhanced Raman Spectroscopy: Theoretical Calculation and Experimental Demonstration*, Opt. Express **23**, 13804 (2015).

[55] L. Gao, T. Li, X. Shi, P. Kumar, R. Li, and B. Liu, *The Fabrication of Gold Colloidal Nanoantennas by a Full Wet Surface Assembly Technique*, Appl. Phys. Express **12**, 064008 (2019).

[56] G. Kang, M. Yang, M. S. Mattei, G. C. Schatz, and R. P. Van Duyne, In Situ *Nanoscale Redox Mapping Using Tip-Enhanced Raman Spectroscopy*, Nano Lett. **19**, 2106 (2019).

[57] H. Wen et al., *Length-Controllable Gold-Coated Silver Nanowire Probes for High AFM-TERS Scattering Activity*, Nano Lett. acs.nanolett.2c03985 (2022).

[58] D. Aherne, D. M. Ledwith, M. Gara, and J. M. Kelly, *Optical Properties and Growth Aspects of Silver Nanoprisms Produced by a Highly Reproducible and Rapid Synthesis at Room Temperature*, Advanced Functional Materials **18**, 2005 (2008).

[59]   D. Gingery and P. Bühlmann, *Single-Step Electrochemical Method for Producing Very Sharp Au Scanning Tunneling Microscopy Tips*, Review of Scientific Instruments **78**, 113703 (2007).

[60]   M. Eisele, M. Krüger, M. Schenk, A. Ziegler, and P. Hommelhoff, *Note: Production of Sharp Gold Tips with High Surface Quality*, Review of Scientific Instruments **82**, 026101 (2011).

[61]   B. Ren, G. Picardi, and B. Pettinger, *Preparation of Gold Tips Suitable for Tip-Enhanced Raman Spectroscopy and Light Emission by Electrochemical Etching*, Review of Scientific Instruments **75**, 837 (2004).

[62]   S. Narasiwodeyar, M. Dwyer, M. Liu, W. K. Park, and L. H. Greene, *Two-Step Fabrication Technique of Gold Tips for Use in Point-Contact Spectroscopy*, Review of Scientific Instruments **86**, 033903 (2015).

[63]   J. Zhang, P. Wang, X. Zhang, H. Ji, J. Luo, H. Wang, and J. Wang, *Systematic Electrochemical Etching of Various Metal Tips for Tunneling Spectroscopy and Scanning Probe Microscopy*, Review of Scientific Instruments **92**, 015124 (2021).

[64]   C. Zhang, B. Gao, L. G. Chen, Q. S. Meng, H. Yang, R. Zhang, X. Tao, H. Y. Gao, Y. Liao, and Z. C. Dong, *Fabrication of Silver Tips for Scanning Tunneling Microscope Induced Luminescence*, Review of Scientific Instruments **82**, 083101 (2011).

[65]   K. Dickmann, F. Demming, and J. Jersch, *New Etching Procedure for Silver Scanning Tunneling Microscopy Tips*, Review of Scientific Instruments **67**, 845 (1996).

[66]   *JDS6600 Quick Guide.Pdf*, (n.d.).

[67]   *LabVIEW For Loops and While Loops Explained*, https://www.ni.com/en-

us/support/documentation/supplemental/08/labview-for-loops-and-while-loops-

explained.html.

[68]   PubChem, *Sulforhodamine B*, https://pubchem.ncbi.nlm.nih.gov/compound/65191.

[69]   M. Li, R. Lv, S. Huang, Y. Dai, Z. Zeng, L. Wang, and B. Ren, *Electrochemical Fabrication of*

Silver Tips for Tip-Enhanced Raman Spectroscopy Assisted by a Machine Vision System,

Journal of Raman Spectroscopy **47**, 808 (2016).

[70]   C. Zhang, B. Gao, L. G. Chen, Q. S. Meng, H. Yang, R. Zhang, X. Tao, H. Y. Gao, Y. Liao, and

Z. C. Dong, *Fabrication of Silver Tips for Scanning Tunneling Microscope Induced*

Luminescence, Review of Scientific Instruments **82**, 083101 (2011).

[71]   *MyDAQ University Kit*, https://www.ni.com/en-us/shop/hardware/products/mydaq-

student-data-acquisition-device.html.

[72]   *Thorlabs - Z812B 12 Mm Motorized Actuator, 3/8*, https://www.thorlabs.com.

[73]   *Kinesis® K-Cube^{TM} Brushed DC Servo Motor Controller*, https://www.thorlabs.com.

[74]   *150V 5x5x10mm Piezo Stack Actuator (SA050510) - PiezoDrive*,

https://www.piezodrive.com/product/150v-5x5x10mm-piezo-stack-actuator-sa050510/.

[75]   *PD200 60W Voltage Amplifier - PiezoDrive*,

https://www.piezodrive.com/product/pd200-60w-voltage-amplifier/.

[76]   *Stanford Research SR530 Dual Phase Lock-In Amplifier*,

https://www.bellnw.com/products/stanford-research-sr530.

[77]   *Triple-Divide^{TM} Rail Mount Aluminum Linear Stages*, https://www.newport.com/f/triple-

divide-translation-stages?q=:ranking-desc:suppress:false:manual-linear-stages-

axesofTravel:X,%20Y,%20Z:manual-linear-stages-maximumStageTravel:25%20mm:manual-

linear-stages-maximumStageTravel:25.4%20mm:manual-linear-stages-

maximumStageTravel:28%20mm:npCategory:single-row-ball-bearing-aluminum-stages.

[78]   *Life Sciences Atomic Force Microscope - Biology AFM for Research*,

https://www.afmworkshop.com/afm-products/atomic-force-microscopes/ls-afm.

[79]   *Oxford Instruments America TERS Microscope Price Quote*, (n.d.).

[80]   *Z812B-Manual.Pdf*, (n.d.).

[81]   F. Zhang, Y. Tan, J. Ding, D. Cao, Y. Gong, Y. Zhang, J. Yang, and T. Yin, *Application and

Progress of Raman Spectroscopy in Male Reproductive System*, Front. Cell Dev. Biol. **9**,

823546 (2022).

[82]   S. Elumalai, S. Managó, and A. C. De Luca, *Raman Microscopy: Progress in Research on

Cancer Cell Sensing*, Sensors (Basel) **20**, 5525 (2020).

8.   Appendices

A.   Schrödinger Equation Quantum Number (n=0) Eigenvalue Proof

These mathematical solutions for the eigenvalues of the Schrödinger equation eigenfunctions

will be a step-by-step process. Previous literature searches generally provide just the solutions

or if they contain steps, many are missing. For basic understanding, steps cannot be skipped.

We begin with the definition of the Schrödinger equation from (1-46)

$$\left[i\hbar \frac{\partial}{\partial t} + \frac{\hbar^2}{2\mu} \frac{\partial^2}{\partial q^2} - \frac{1}{2} kq^2 \right] \phi(q,t) = 0 \tag{A-1}$$

To apply this equation to an electron in an atom, we must make the following substitution

$$\phi(q,t) = e^{-iEt/\hbar} \phi(q) \tag{A-2}$$

This is allowed because the electrons are localized near a proton and has a definite energy. By

doing this, we've created a spatial component that is a time independent function. We can then

substitute this into (A-1)

$$\left[i\hbar \frac{\partial}{\partial t} + \frac{\hbar^2}{2\mu} \frac{\partial^2}{\partial q^2} - \frac{1}{2} kq^2 \right] e^{-iEt/\hbar} \phi(q) = 0 \tag{A-3}$$

First perform the partial derivative with respect to time

$$i\hbar \frac{\partial}{\partial t} e^{-iEt/\hbar} \phi(q) = -i^2 E \frac{\hbar}{\hbar} e^{-iEt/\hbar} \phi(q) \tag{A-4}$$

$$i\hbar \frac{\partial}{\partial t} e^{-iEt/\hbar} \phi(q) = E e^{-iEt/\hbar} \phi(q) \tag{A-5}$$

Rearranging (A-1) and putting the above solution for the partial derivative for time generates

the basic equation we will use for each quantum number

$$\frac{\hbar^2}{2\mu}\frac{\partial^2 \phi_n(q)}{\partial q^2}e^{-iEt/\hbar} + \left[E_n - \frac{1}{2}kq^2\right]e^{-iEt/\hbar}\phi_{n(q)} = 0 \qquad\text{(A-6)}$$

Since every term has a $e^{-iEt/\hbar}$ term, we can just divide the entire equation by this since no

other partial derivative deals with it.

$$\frac{\hbar^2}{2\mu}\frac{\partial^2 \phi_n(q)}{\partial q^2} + \left[E_n - \frac{1}{2}kq^2\right]\phi_{n(q)} = 0 \qquad\text{(A-7)}$$

The corresponding eigenfunction for the nth term is

$$\phi_n = \frac{(\alpha/\pi)^{1/4}}{\sqrt{2^n n!}}e^{-\alpha q^2/2}H_n\left(\sqrt{\alpha}q\right) \qquad\text{(A-8)}$$

Because $H_n\left(\sqrt{\alpha}q\right)$ is a nth term Hermitian polynomial, it has the following values for the

corresponding n-terms

$$n = 0 \qquad\qquad H_0(x) = 1 \qquad\qquad H_0\left(\sqrt{\alpha}q\right) = 1 \qquad\text{(A-9)}$$

$$n = 1 \qquad\qquad H_1(x) = 2x \qquad\quad H_1\left(\sqrt{\alpha}q\right) = 2\sqrt{\alpha}q \qquad\text{(A-10)}$$

$$n = 2 \qquad\quad H_2(x) = 4x^2 - 2 \qquad H_2\left(\sqrt{\alpha}q\right) = 4\alpha q - 2 \qquad\text{(A-11)}$$

We now begin our derivation with $n = 0$:

$$\frac{\hbar^2}{2\mu}\frac{\partial^2 \phi_0(q)}{\partial q^2} + \left[E_0 - \frac{1}{2}kq^2\right]\phi_{0(q)} = 0 \qquad\text{(A-12)}$$

$$\left[\frac{\hbar^2}{2\mu}\frac{\partial^2}{\partial q^2} + \left(E_0 - \frac{1}{2}kq^2\right)\right]\frac{(\alpha/\pi)^{1/4}}{\sqrt{2^0 0!}}e^{-\alpha q^2/2}H_0\left(\sqrt{\alpha}q\right) = 0 \qquad\text{(A-13)}$$

$$\left[\frac{\hbar^2}{2\mu}\frac{\partial^2}{\partial q^2} + \left(E_0 - \frac{1}{2}kq^2\right)\right]\frac{(\alpha/\pi)^{1/4}}{1}e^{-\alpha q^2/2}(1) = 0 \qquad\text{(A-14)}$$

$$\left[\frac{\hbar^2}{2\mu}\frac{\partial^2}{\partial q^2} + \left(E_0 - \frac{1}{2}kq^2\right)\right]\left(\frac{\alpha}{\pi}\right)^{\frac{1}{4}}e^{-\alpha q^2/2} = 0 \qquad\text{(A-15)}$$

For simplicity, we work with only the partial term on the left

$$\frac{\hbar^2}{2\mu}\frac{\partial^2}{\partial q^2}\left[\left(\frac{\alpha}{\pi}\right)^{\frac{1}{4}}e^{-\alpha q^2/2}\right]$$ (A-16)

$$\frac{\hbar^2}{2\mu}\frac{\partial}{\partial q}\left[\alpha q\left(\frac{\alpha}{\pi}\right)^{\frac{1}{4}}e^{-\alpha q^2/2}\right]$$ (A-17)

$$\frac{\hbar^2}{2\mu}\left[\alpha\left(\frac{\alpha}{\pi}\right)^{\frac{1}{4}}(\alpha q^2 - 1)e^{-\alpha q^2/2}\right]$$ (A-18)

Plugging this back into (A-15) yields

$$\left[\frac{\hbar^2}{2\mu}\alpha(\alpha q^2 - 1) + \left(E_0 - \frac{1}{2}kq^2\right)\right]\left(\frac{\alpha}{\pi}\right)^{\frac{1}{4}}e^{-\alpha q^2/2} = 0$$ (A-19)

We can remove the parts outside the bracket by dividing the entire equation by it after moving

the potential component $(\frac{1}{2}kq^2)$ to the right

$$\left[\frac{\hbar^2}{2\mu}\alpha(\alpha q^2 - 1) + E_0\right]\left(\frac{\alpha}{\pi}\right)^{\frac{1}{4}}e^{-\alpha q^2/2} = \left(\frac{1}{2}kq^2\right)\left(\frac{\alpha}{\pi}\right)^{\frac{1}{4}}e^{-\alpha q^2/2}$$ (A-20)

$$\frac{\hbar^2}{2\mu}\alpha(\alpha q^2 - 1) + E_0 = \frac{1}{2}kq^2$$ (A-21)

Now we will focus only on the far-left term containing the $\alpha -$ terms

$$\frac{\hbar^2}{2\mu}\alpha(\alpha q^2 - 1)$$ (A-22)

We make the substitutions from (1-49)

$$\alpha = 4\pi^2\mu\nu/h$$ (A-23)

$$\frac{\hbar^2}{2\mu}\alpha(\alpha q^2 - 1) = \frac{\hbar^2}{2\mu}\frac{4\pi^2\mu\nu}{h}\left(\frac{4\pi^2\mu\nu}{h}q^2 - 1\right)$$ (A-24)

Next, we must cancel terms after making the substitution $\hbar = \frac{h}{2\pi}$

161

$$\frac{\hbar^2}{2\mu}\alpha(\alpha q^2 - 1) = \frac{1}{2\mu}\left(\frac{h^2}{4\pi^2}\right)\frac{4\pi^2\mu\nu}{h}\left(\frac{4\pi^2\mu\nu}{h}q^2 - 1\right) \tag{A-25}$$

$$\frac{\hbar^2}{2\mu}\alpha(\alpha q^2 - 1) = \frac{h\nu}{2}\left(\frac{4\pi^2\mu\nu}{h}q^2 - 1\right) \tag{A-26}$$

Distributing and cancelling further terms

$$\frac{\hbar^2}{2\mu}\alpha(\alpha q^2 - 1) = 2\pi^2\nu^2\mu q^2 - \frac{h\nu}{2} \tag{A-27}$$

Using the definition found in (1-22) for ν

$$\nu = \frac{1}{2\pi}\sqrt{\frac{k}{\mu}} \tag{A-28}$$

We can make a substitution into the left term

$$\frac{\hbar^2}{2\mu}\alpha(\alpha q^2 - 1) = 2\pi^2\mu\left(\frac{1}{2\pi}\sqrt{\frac{k}{\mu}}\right)^2 q^2 - \frac{h\nu}{2} \tag{A-29}$$

$$\frac{\hbar^2}{2\mu}\alpha(\alpha q^2 - 1) = 2\pi^2\mu\left(\frac{k}{4\pi^2\mu}\right)q^2 - \frac{h\nu}{2} \tag{A-30}$$

Cancelling out terms again reduces the term further

$$\frac{\hbar^2}{2\mu}\alpha(\alpha q^2 - 1) = \frac{1}{2}kq^2 - \frac{h\nu}{2} \tag{A-31}$$

Plugging this expression back into (A-21) yields

$$\frac{1}{2}kq^2 - \frac{h\nu}{2} + E_0 = \frac{1}{2}kq^2 \tag{A-32}$$

Finally rearranging and cancelling out terms gives the eigenvalue for the energy of an electron

at the ground state:

$$E_0 = \frac{h\nu}{2} \tag{A-33}$$

B.   Basic Matrix Multiplication

For many readers, it may have been several years since they have used Linear Algebra in their everyday lives. This appendix will show basic matrix operations for the reader to refresh any skills. For matrix multiplication, the first matrix must have as many columns as the second matrix has rows. The elements of the final matrix are created using dot products of the rows of the first matrix with the columns of the second matrix. We start with the multiplication of a (3x2) matrix with a (2x3) matrix.

$$\begin{bmatrix} x_{11} & x_{12} \\ x_{21} & x_{22} \\ x_{31} & x_{33} \end{bmatrix} \begin{bmatrix} y_{11} & y_{12} & y_{13} \\ y_{21} & y_{22} & y_{23} \end{bmatrix} = \begin{bmatrix} z_{11} & z_{12} & z_{13} \\ z_{21} & z_{22} & z_{23} \\ z_{13} & z_{23} & z_{33} \end{bmatrix}$$

In this matrix, the first-row solutions for the z-matrix elements are:

$$z_{11} = (x_{11}y11) + (x_{12}y21), \qquad z_{12} = (x_{11}y_{12}) + (x_{12}y_{22}), \qquad z_{13} = (x_{11}y_{13}) + (x_{12}y_{23})$$

To further cement the process of matrix multiplication, we will use a matrix with actual values and show the steps to reach a solution:

$$\begin{bmatrix} 1 & 4 \\ 3 & 2 \\ -1 & 0 \end{bmatrix} \begin{bmatrix} 2 & -2 & 0 \\ 1 & 1 & 3 \end{bmatrix} = \begin{bmatrix} (1 \times 2) + (4 \times 1) & (1 \times -2) + (4 \times 1) & (1 \times 0) + (4 \times 3) \\ (3 \times 2) + (2 \times 1) & (3 \times -2) + (2 \times 1) & (3 \times 0) + (2 \times 3) \\ (-1 \times 2) + (0 \times 1) & (-1 \times -2) + (0 \times 1) & (-1 \times 0) + (0 \times 3) \end{bmatrix}$$

164

$$\begin{bmatrix} 1 & 4 \\ 3 & 2 \\ -1 & 0 \end{bmatrix} \begin{bmatrix} 2 & -2 & 0 \\ 1 & 1 & 3 \end{bmatrix} = \begin{bmatrix} 6 & 2 & 12 \\ 8 & -4 & 6 \\ -2 & 2 & 0 \end{bmatrix}$$

The product of a (3x2) matrix and a (2x3) matrix is a (3x3). The product of two matrices has the

number of rows of the first matrix and the number of columns of the second matrix. The

individual elements of a matrix do not have to be numbers but can be vectors, scalars, or even

functions.

C.   Polarizability of a Sphere in a Medium

We begin with a sphere in an external electrical field. The sphere in this external electric field has a dielectric constant ϵ_2 and a radius of R. The external electric field is applied to a medium with dielectric constant ϵ_1 in which the sphere is placed. We can set the electric field to be uniform and propagating in the z-axis.

There are no charges outside of the sphere so Laplace's equation ($\Delta\phi = 0$) is said to be satisfied. Inside the sphere there are also no charges present, so the equation is satisfied here. On the sphere's surface though, there are charges present, so the equation is not satisfied. To differentiate the two solutions to Laplace's equation, we will notate the two potentials as ϕ_1 and ϕ_2 as the outer and inner potentials respectively. The final step in the setup of the problem is to consider the sphere at the origin of the coordinate system and to use spherical coordinates. The benefit here in doing that is to use the Legrende Polynomial solutions for Laplace's equations with symmetry around the z-axis:

$$\phi_1 = \sum_{n=0}^{\infty} \left(A_n r^n + \frac{B_n}{r^{n+1}} \right) P_n(cos\theta) \tag{C-1}$$

$$\phi_2 = \sum_{n=0}^{\infty} \left(C_n r^n + \frac{D_n}{r^{n+1}} \right) P_n(cos\theta) \tag{C-2}$$

There are four boundary conditions present in this setup:

1. As $r \to \infty$, then $\phi_1 = -E_0 z$

2. At $r = R$, $\phi_1 = \phi_2$ or the potentials must be continuous

3. At $r = R$, $\epsilon_1 \left(\frac{\partial \phi_1}{\partial r} \right)_{r=R} = \epsilon_2 \left(\frac{\partial \phi_2}{\partial r} \right)_{r=R}$ or the dielectric displacement must be

   continuous

4. At $r = 0$, there can be no singularities

We will use the fourth boundary condition first. This boundary condition mandates that there

can be nothing divided by 0 when $r = 0$ so all solutions must have a coefficient for D equal to

zero. Thus

$$\phi_2 = \sum_{n=0}^{\infty} C_n r^n P_n(\cos\theta) \tag{C-3}$$

We now work on the first boundary condition. We can modify (C-1) by noting here that the B_n

term goes to zero because it is divided by infinity. So, we rewrite it

$$\phi_1 = \sum_{n=0}^{\infty} A_n r^n P_n(\cos\theta) \tag{C-4}$$

We need the solution to this to appear as

$$\phi_1 = -E_0 z = -E_0 r \cos(\theta) \tag{C-5}$$

We now need the first few solutions to the Legendre Polynomials to know which solution of n

we need

n	$P_n(x)$
0	1
1	x

2	$\frac{1}{2}(3x^2 - 1)$

We can see that $n = 1$ is the only solution that works here so we say:

$$\phi_1 = A_1 r^1 P_1(cos\theta) \tag{C-6}$$

With the condition of (D-5), we can say that

$$-E_0 r cos(\theta) = A_1 r cos(\theta) \tag{C-7}$$

Then it is easy to see here that the conditions for A_n are:

$$A_n = \begin{cases} -E_0, n = 1 \\ 0, n \neq 1 \end{cases} \tag{C-8}$$

At the boundary condition $r = R$, we are at the sphere surface. For all solutions where $n \neq 1$,

we need to evaluate both solutions and compare them together. Using the definition found in

(C-8), we can rewrite (C-1) for all solutions where $n \neq 1$ and analyze the third boundary

condition:

$$\phi_1 = \sum_{n=0, \neq 1}^{\infty} \frac{B_n}{R^{n+1}} P_n(cos\theta) \tag{C-9}$$

$$\frac{\partial}{\partial r} \left[\frac{B_n}{r^{n+1}} P_n(cos\theta) \right]_{r=R} = (n + 1) \frac{B_n}{R^{n+2}} P_n(cos\theta) \tag{C-10}$$

$$\phi_2 = \sum_{n=0, \neq 1}^{\infty} C_n R^n P_n(cos\theta) \tag{C-11}$$

$$\frac{\partial}{\partial r} [C_n r^n P_n(cos\theta)]_{r=R} = n C_n R^{n-1} P_n(cos\theta) \tag{C-12}$$

There is no way to equate (C-10) with (C-12) for all solutions where $n \neq 1$ unless the $C_n = B_n = 0$ but the potential is not zero at this boundary condition. We know that the correct n-value

must be $n = 1$ so the solutions for boundary condition 3 for the respective potentials are:

168

$$\epsilon_1 \left(\frac{\partial \phi_1}{\partial r}\right)_{r=R} = \epsilon_1 \frac{\partial}{\partial r} \left[\frac{B_1}{r^{1+1}} P_1(cos\theta) - A_1 r cos(\theta)\right]_{r=R} \tag{C-13}$$

$$\epsilon_1 \left(\frac{\partial \phi_1}{\partial r}\right)_{r=R} = -2\epsilon_1 \left[\frac{B_1}{R^3} cos(\theta) - E_0 cos(\theta)\right] \tag{C-14}$$

$$\epsilon_2 \left(\frac{\partial \phi_2}{\partial r}\right)_{r=R} = \epsilon_2 \frac{\partial}{\partial r} [C_1 r^1 P_1(cos\theta)]_{r=R} \tag{C-15}$$

$$\epsilon_2 \left(\frac{\partial \phi_2}{\partial r}\right)_{r=R} = \epsilon_2 C_1 cos(\theta) \tag{C-16}$$

We can compare the coefficients now

$$-\epsilon_1 \left[\frac{B_1}{R^3} + E_0\right] = \epsilon_2 C_1 \tag{C-17}$$

We now look at the coefficients with respect to boundary condition 2 to obtain a value for C_1:

$$(\phi_1)_{r=R} = \left[\frac{B_1}{r^{1+1}} P_1(cos\theta) - A_1 r cos(\theta)\right]_{r=R} \tag{C-18}$$

$$(\phi_1)_{r=R} = \frac{B_1}{R^2} cos(\theta) - E_0 R cos(\theta) \tag{C-19}$$

$$(\phi_2)_{r=R} = [C_1 r^1 P_1 cos(\theta)] \tag{C-20}$$

$$(\phi_2)_{r=R} = C_1 R cos(\theta) \tag{C-21}$$

Setting the coefficients equal

$$\frac{B_1}{R^2} - E_0 R = C_1 R \tag{C-22}$$

$$\frac{B_1}{R^3} - E_0 = C_1 \tag{C-23}$$

Plugging this value for C_1 into (C-17) will generate a solution for B_1

$$-\epsilon_1 \left[\frac{B_1}{R^3} + E_0\right] = \epsilon_2 \left(\frac{B_1}{R^3} - E_0\right) \tag{C-24}$$

$$\frac{B_1}{R^3}(\epsilon_1 + 2\epsilon_2) + E_0(\epsilon_1 - \epsilon_2) = 0 \tag{C-25}$$

$$B_1 = \left(\frac{\epsilon_2 - \epsilon_1}{\epsilon_1 + 2\epsilon_2}\right) R^3 E_0 \tag{C-26}$$

Plugging this back into (C-23) and then simplifying leads to a solution for C_1

$$\left(\frac{1}{R^3}\right) \left[\left(\frac{\epsilon_2 - \epsilon_1}{\epsilon_1 + 2\epsilon_2}\right) R^3 E_0\right] - E_0 = C_1 \tag{C-27}$$

$$\left(\frac{\epsilon_2 - \epsilon_1}{\epsilon_1 + 2\epsilon_2}\right) E_0 - \left(\frac{\epsilon_1 + 2\epsilon_2}{\epsilon_1 + 2\epsilon_2}\right) E_0 = C_1 \tag{C-28}$$

$$C_1 = -\left(\frac{3\epsilon_2}{\epsilon_1 + 2\epsilon_2}\right) E_0 \tag{C-29}$$

We can plug the values from (C-26) and (C-29) into the equations (C-1) and (C-3) to find

solutions to the potentials across all values of r where $n = 1$

$$(\phi_1) = \left(\frac{1}{r^2}\right) \left(\frac{\epsilon_2 - \epsilon_1}{\epsilon_1 + 2\epsilon_2}\right) R^3 E_0 cos(\theta) - E_0 r cos(\theta) \tag{C-30}$$

$$(\phi_1) = \left(\frac{\epsilon_2 - \epsilon_1}{\epsilon_1 + 2\epsilon_2} \frac{R^3}{r^3} - 1\right) E_0 r cos(\theta) \tag{C-31}$$

$$(\phi_2) = -\left(\frac{3\epsilon_2}{\epsilon_1 + 2\epsilon_2}\right) E_0 r cos(\theta) \tag{C-32}$$

Since we can say $z = rcos(\theta)$, we can express the terms with respect to the direction of

propagation of the electric field.

$$(\phi_1) = \left(\frac{\epsilon_2 - \epsilon_1}{\epsilon_1 + 2\epsilon_2} \frac{R^3}{r^3} - 1\right) E_0 z \tag{C-33}$$

$$(\phi_2) = -\left(\frac{3\epsilon_2}{\epsilon_1 + 2\epsilon_2}\right) E_0 z \tag{C-34}$$

If we ignore the potential from the external electric field and only focus on the potential terms with respect to the surface charges, we can rewrite (D-33) and (D-34) by modifying removing the external term from (D-33) and (D-28) for ϕ_1 and ϕ_2 respectively. The new terms will be prime terms for their previous expressions.

$$\left(\phi'_1\right) = \left(\frac{\epsilon_2 - \epsilon_1}{\epsilon_1 + 2\epsilon_2}\frac{R^3}{r^3}\right)E_0 z \tag{C-35}$$

$$\left(\phi'_2\right) = \left(\frac{(\epsilon_2 - \epsilon_1)}{\epsilon_1 + 2\epsilon_2}\right)E_0 z \tag{C-36}$$

We are concerned with the external component (ϕ'_1). By comparing this term to the definition of a potential due to an ideal dipole at the center of the sphere, we can say that the dipole moment for this situation can be expressed

$$\vec{p} = \frac{\epsilon_2 - \epsilon_1}{2\epsilon_1 + \epsilon_2}R^3\vec{E}_0 \tag{C-37}$$

If we put that sphere in a vacuum, we can say that the new dielectric term for the sphere is $\epsilon_2 = \epsilon$ and $\epsilon_1 = 1$. We can then write the total electric field outside the sphere with the sphere being substituted for a dipole vector

$$\vec{m} = \frac{\epsilon + 1}{\epsilon + 2}R^3\vec{E}_0 \tag{C-38}$$

If we define the sphere as being polarized linearly, we can use the induced dipole moment $(\vec{m})$ to define the polarizability (α) of the sphere by the relationship between the induced dipole moment and the electric field for linear polarization:

$$\vec{m} = \alpha\vec{E}_0 \tag{C-39}$$

Thus, the polarizability of the sphere with dielectric constant ϵ is

$$\alpha = \frac{\epsilon - 1}{\epsilon + 2} R^3 \qquad\qquad\text{(C-40)}$$

D.   Drude Model Derivation

Many textbooks simply state that they are using the Drude model and do not contain any derivations of the model. Those that do, generally devote more time to specific components of the derivation and can be hard to follow. This is an attempt to alleviate the confusing aspects and present a detailed derivation.

The general Drude model derivation starts with a driven, damped harmonic oscillator with a net force on an electron as:

$$\vec{F}_{\text{net}} = \vec{F}_{\text{driving}} + \vec{F}_{\text{spring}} + \vec{F}_{\text{damping}} \tag{D-1}$$

The driving force on the electrons is the Lorentz force, $\vec{F}_L = q(\vec{E} + \vec{v} \times \vec{B})$. In this derivation, we will ignore the $\vec{B}$-component. The damping force for the harmonic oscillator will be shown with a coefficient that allows the expression to have a mass term. The spring force is from Hooke's law, so the total net force expression is then:

$$m\frac{d^2\vec{x}}{dt^2} = q\vec{E} + (-kx) + \left(-\gamma m \frac{d\vec{x}}{dt}\right) \tag{D-2}$$

We need to rearrange this to have the driving force by itself and all factors of x together.

$$q\vec{E} = m\frac{d^2\vec{x}}{dt^2} + \gamma m \frac{d\vec{x}}{dt} - k\vec{x} \tag{D-3}$$

The next step is to factor out a mass term from both sides:

$$\frac{q\vec{E}}{m} = \frac{d^2\vec{x}}{dt^2} + \gamma \frac{d\vec{x}}{dt} - \frac{k}{m}\vec{x} \tag{D-4}$$

We know that the electric field vector and the position vector can be expressed in complex notation with respect to their maximum values.

$$\vec{E} = \vec{E}_0 e^{-i\omega t} \tag{D-5}$$

$$\vec{x} = \vec{x}_0 e^{i\omega t} \tag{D-6}$$

The derivatives of the position vector with respect to time are:

$$\frac{d}{dt}\left(\vec{x}_0 e^{-i\omega t}\right) = -i\omega \vec{x}_0 e^{-i\omega t} \tag{D-7}$$

$$\frac{d^2}{dt^2}\left(\vec{x}_0 e^{-i\omega t}\right) = \omega^2 \vec{x}_0 e^{-i\omega t} \tag{D-8}$$

We take these solutions and substitute them back into (D-4).

$$\frac{q\vec{E}}{m} = \left[-\omega^2 - i\omega\gamma + \frac{k}{m}\right]\vec{x}_0 e^{-i\omega t} \tag{D-9}$$

We need to solve this for the position vector $\vec{x}$

$$\frac{q\vec{E}}{m}\left(\frac{1}{-\omega^2 - i\omega\gamma + \frac{k}{m}}\right) = \vec{x} \tag{D-10}$$

We can show relationship between the spring frequency of the spring between the electrons and the nuclei (ω_0) and the spring constant (k)

$$\omega_0 = \sqrt{\frac{k}{m}} \tag{D-11}$$

This will allow us to write the denominator in only ω-terms

$$\frac{q\vec{E}}{m}\left(\frac{1}{-\omega^2 - i\omega\gamma + \omega_0^2}\right) = \vec{x} \tag{D-12}$$

174

Since the system is oscillating and is a dipole, oscillating dipole moment ($\vec{p}$), not be confused

with momentum, can be written as:

$$\vec{p} = q\vec{x} \tag{D-13}$$

Direction substitution of (D-12) yields

$$\vec{p} = \frac{q^2\vec{E}}{m}\left(\frac{1}{-\omega^2 - i\omega\gamma + \omega_0^2}\right) \tag{D-12}$$

The polarization of the material ($\vec{P}$) is the dipole moments (D-12) times the total dipole density

(N).

$$\vec{P} = N\vec{p} \tag{D-13}$$

Now we need to look at how EM waves behave in a metal. We start with Maxwell's

Equations in a medium

$$\nabla \cdot \vec{D} = \rho_{ext} \tag{D-14}$$

$$\nabla \cdot \vec{B} = 0 \tag{D-15}$$

$$\nabla \times \vec{E} = -\frac{\partial \vec{B}}{\partial t} \tag{D-16}$$

$$\nabla \times \vec{H} = \vec{J}_{ext} + \frac{\partial \vec{D}}{\partial t} \tag{D-17}$$

The definitions of the included vectors are as listed: the dielectric displacement ($\vec{D}$), the

external electric field ($\vec{E}$), the magnetic flux density ($\vec{B}$), and the magnetic field ($\vec{H}$).

Additionally, we must note the external charge density (ρ_{ext}) and the external current density

($\vec{J}_{ext}$). The total charge density is given as

$$\rho_{tot} = \rho_{ext} + \rho_{in} \tag{D-18}$$

It follows that the total current density is

$$\vec{J}_{tot} = \vec{J}_{ext} + \vec{J}_{in} \tag{D-19}$$

It should be noted that the external components drive the system while the internal

components respond. We can now further define the dielectric displacement and the magnetic

field

$$\vec{D} = \epsilon_0 \vec{E} + \vec{P} \tag{D-20}$$

$$\vec{H} = \frac{1}{\mu_0} \vec{B} - \vec{M} \tag{D-21}$$

If the material that the EM waves propagate is non-magnetic, then $\vec{M} = 0$. Since we previously

defined $\vec{P}$ in (D-13), we can relate it to the internal charge density

$$\nabla \cdot \vec{P} = \rho_{in} \tag{D-22}$$

In the effort to relate all the different components together, we can relate the internal current

density with the polarization through the conservation of charge ($\nabla \cdot \vec{J} = -\frac{\partial \rho}{\partial t}$)

$$\vec{J}_{in} = \frac{\partial \vec{P}}{\partial t} \tag{D-23}$$

With this relation, we can express the external electric field ($\vec{E}$) as the summation of the

internal and external fields by using (D-14):

$$\nabla \cdot \vec{D} = \nabla \cdot \left(\epsilon_0 \vec{E} + \vec{P} \right) \tag{D-24}$$

$$\nabla \cdot \vec{D} = \nabla \cdot \epsilon_0 \vec{E} + \nabla \cdot \vec{P} \tag{D-25}$$

$$\nabla \cdot \vec{D} = \nabla \cdot \epsilon_0 \vec{E} + \rho_{in} \tag{D-26}$$

$$\rho_{\text{tot}} - \rho_{\text{in}} = \nabla \cdot \epsilon_0 \vec{E} \qquad \text{(D-27)}$$

$$\frac{\rho_{ext}}{\epsilon_0} = \nabla \cdot \vec{E} \qquad \text{(D-28)}$$

In vacuum, we could write out the dielectric displacement as:

$$\vec{D} = \epsilon_0 \vec{E} \qquad \text{(D-29)}$$

If the material we are examining also is linear and isotropic, we can define the relationship between the external field and the polarization as:

$$\vec{P} = \epsilon_0 \chi_0 \vec{E} \qquad \text{(D-30)}$$

The χ_0-term is the electric susceptibility of the material which is a measure of the degree of polarization of the material in response to the external electric field. If we substitute this definition into (D-20) we have the dielectric displacement in only external electric field terms

$$\vec{D} = \epsilon_0 \vec{E} + \epsilon_0 \chi_0 \vec{E} \qquad \text{(D-31)}$$

$$\vec{D} = \epsilon_0 (1 + \chi_0) \vec{E} \qquad \text{(D-32)}$$

We will further substitute terms in using the definition of the effective permittivity (ϵ)

$$\epsilon = \epsilon_0 (1 + \chi_0) \qquad \text{(D-33)}$$

$$\vec{D} = \epsilon \vec{E} \qquad \text{(D-34)}$$

We can now go back to (D-30) to write out χ_0 as a ratio of $\vec{P}$ and $\vec{E}$

$$\chi_0 = \frac{\vec{P}}{\epsilon_0 \vec{E}} \qquad \text{(D-35)}$$

The other definition of the effective permittivity is a relationship between the vacuum permittivity (ϵ_0) and the relative permittivity of the medium (ϵ_r):

$$\epsilon = \epsilon_0 \epsilon_r \tag{D-36}$$

By comparing (D-36) and (D-33), the relative permittivity is then

$$\epsilon_r = 1 + \chi_0 \tag{D-37}$$

We now substitute (D-35) and (D-13) into (D-37)

$$\epsilon_r = 1 + \frac{\vec{P}}{\epsilon_0 \vec{E}} \tag{D-38}$$

$$\epsilon_r = 1 + \frac{N\vec{p}}{\epsilon_0 \vec{E}} \tag{D-39}$$

Substituting (D-12) into (D-39) and simplifying gives

$$\epsilon_r = 1 + \frac{N}{\epsilon_0} \frac{q^2}{m} \left(\frac{1}{-\omega^2 - i\omega\gamma + \omega_0^2} \right) \tag{D-40}$$

The term outside the parenthesis is defined as the plasma frequency squared (ω_p^2). This allows us to write the generalized solution for the Drude Model as shown in (D-42)

$$\epsilon_r = 1 + \left(\frac{\omega_p^2}{-\omega^2 - i\omega\gamma + \omega_0^2} \right) \tag{D-40}$$

$$\epsilon_r = 1 + \left((-1) \frac{\omega_p^2}{\omega^2 + i\omega\gamma - \omega_0^2} \right) \tag{D-41}$$

$$\epsilon_r = 1 - \left(\frac{\omega_p^2}{\omega^2 + i\omega\gamma - \omega_0^2} \right) \tag{D-42}$$

To apply this generalized solution to a metal medium, we set $\omega_0^2 = 0$ as there are no restoring forces in metals. This is because the Drude model solution is for valence electrons in the medium and for metals, the valence electrons are not attached to the nuclei. The Drude Model for a metal is:

$$\epsilon_r = 1 - \left(\frac{\omega_p^2}{\omega^2 + i\omega\gamma} \right) \qquad \text{(D-43)}$$

E.   Complex Refractive Index of Noble Metals from Christy & Johnson

eV	Wavelength (nm)	Frequency(ω)	Silver		Gold		Copper	
			n	k	n	k	n	k
0.64	1934.59820553	9.72E+14	0.24	14.08	0.92	13.78	1.09	13.43
0.77	1607.97772927	1.17E+15	0.15	11.85	0.56	11.21	0.76	11.12
0.89	1391.17174330	1.35E+15	0.13	10.1	0.43	9.519	0.6	9.439
1.02	1213.86554073	1.55E+15	0.09	8.828	0.35	8.145	0.48	8.245
1.14	1086.09022065	1.73E+15	0.04	7.795	0.27	7.15	0.36	7.217
1.26	982.65305678	1.91E+15	0.04	6.992	0.22	6.35	0.32	6.421
1.39	890.75025291	2.11E+15	0.04	6.312	0.17	5.663	0.3	5.768
1.51	819.96215334	2.29E+15	0.04	5.727	0.16	5.803	0.26	5.18
1.64	754.96515338	2.49E+15	0.03	5.242	0.14	4.542	0.24	4.665
1.76	703.49025656	2.67E+15	0.04	4.838	0.13	4.103	0.21	4.205
1.88	658.58662316	2.86E+15	0.05	4.483	0.14	3.697	0.22	3.747
2.01	615.99146843	3.05E+15	0.06	4.152	0.21	3.272	0.3	3.205
2.13	581.28772373	3.24E+15	0.05	3.858	0.29	2.863	0.7	2.704
2.26	547.85081927	3.43E+15	0.06	3.586	0.43	2.455	1.02	2.577
2.38	520.22808888	3.62E+15	0.05	3.324	0.62	2.081	1.18	2.608
2.5	495.25714062	3.80E+15	0.05	3.093	1.04	1.833	1.22	2.564
2.63	470.77674963	4.00E+15	0.05	2.869	1.31	1.849	1.25	2.483

2.75	450.23376420	4.18E+15	0.04	2.657	1.38	1.914	1.24	2.397
2.88	429.91071234	4.38E+15	0.04	2.462	1.45	1.948	1.25	2.305
3	412.71428385	4.56E+15	0.05	2.275	1.46	1.958	1.28	2.207
3.12	396.84065754	4.74E+15	0.05	2.07	1.47	1.952	1.32	2.116
3.25	380.96703124	4.94E+15	0.05	1.864	1.46	1.933	1.33	2.045
3.37	367.40143963	5.12E+15	0.07	1.657	1.48	1.895	1.36	1.975
3.5	353.75510044	5.32E+15	0.1	1.419	1.5	1.866	1.37	1.916
3.62	342.02841203	5.50E+15	0.14	1.142	1.48	1.871	1.36	1.864
3.74	331.05423838	5.68E+15	0.17	0.829	1.48	1.883	1.34	1.821
3.87	319.93355337	5.88E+15	0.81	0.392	1.54	1.898	1.38	1.783
3.99	310.31149161	6.06E+15	1.13	0.616	1.53	1.893	1.38	1.729
4.12	300.52010960	6.26E+15	1.34	0.964	1.53	1.889	1.4	1.679
4.24	292.01482348	6.44E+15	1.39	1.161	1.49	1.878	1.42	1.633
4.36	283.97771824	6.62E+15	1.41	1.264	1.47	1.869	1.45	1.633
4.49	275.75564622	6.82E+15	1.41	1.331	1.43	1.847	1.46	1.646
4.61	268.57762506	7.00E+15	1.38	1.372	1.38	1.803	1.45	1.668
4.74	261.21157205	7.20E+15	1.35	1.387	1.35	1.749	1.41	1.691
4.86	254.76190361	7.38E+15	1.33	1.393	1.33	1.688	1.41	1.741
4.98	248.62306256	7.57E+15	1.31	1.389	1.33	1.631	1.37	1.783
5.11	242.29801400	7.76E+15	1.3	1.378	1.32	1.577	1.34	1.799
5.23	236.73859494	7.95E+15	1.28	1.367	1.32	1.536	1.28	1.802
5.36	230.99680066	8.14E+15	1.28	1.357	1.3	1.497	1.23	1.792

5.48	225.93847656	8.33E+15	1.26	1.344	1.31	1.46	1.18	1.768
5.6	221.09693778	8.51E+15	1.25	1.342	1.3	1.427	1.13	1.737
5.73	216.08077688	8.71E+15	1.22	1.336	1.3	1.387	1.08	1.699
5.85	211.64835069	8.89E+15	1.2	1.325	1.3	1.35	1.04	1.651
5.98	207.04729959	9.09E+15	1.18	1.312	1.3	1.304	1.01	1.599
6.1	202.97423796	9.27E+15	1.15	1.296	1.33	1.277	0.99	1.55
6.22	199.05833626	9.45E+15	1.14	1.277	1.33	1.251	0.98	1.493
6.35	194.98312623	9.65E+15	1.12	1.255	1.34	1.226	0.97	1.44
6.47	191.36674676	9.83E+15	1.1	1.232	1.32	1.203	0.95	1.388
6.6	187.59740175	1.00E+16	1.07	1.212	1.28	1.188	0.94	1.337

F.   Dispersion Relation Derivation for Surface Plasmon on a Flat Metal Surface

We begin with the transverse magnetic-field (TM) mode electric field and magnetic field equations. The equations are separated into two categories, inside ($z < 0$) and outside ($z > 0$) the flat, metal surface. For $z > 0$, the equations are:

$$\vec{E}_2 = (E_{x2}, 0, E_{z2})e^{i(k_{x2}x - k_{z2}z - \omega t)} \tag{G-1}$$

$$\vec{H}_2 = (0, H_{y2}, 0)e^{i(k_{x2}x - k_{z2}z - \omega t)} \tag{G-2}$$

For $z < 0$

$$\vec{E}_1 = (E_{x1}, 0, E_{z1})e^{i(k_{x1}x + k_{z1}z - \omega t)} \tag{G-3}$$

$$\vec{H}_1 = (0, H_{y1}, 0)e^{i(k_{x1}x + k_{z1}z - \omega t)} \tag{G-4}$$

The wavevectors (k) are opposite signed to each other so that as the respective values of z move away from $z = 0$, the z-component fields decay. The above equations must satisfy Maxwell's equations for a system with no external charges

$$\nabla \times \vec{H} = \frac{\epsilon}{c}\frac{\partial \vec{E}}{\partial t} \tag{G-5}$$

$$\nabla \times \vec{E} = \frac{1}{c}\frac{\partial \vec{H}}{\partial t} \tag{G-6}$$

$$\nabla \cdot \vec{E} = 0 \tag{G-7}$$

$$\nabla \cdot \vec{H} = 0 \tag{G-8}$$

At the surface, the respective TM mode solutions must be continuous

$$E_{x1} = E_{x2} \tag{G-9}$$

$$H_{y1} = H_{y2} \tag{G-10}$$

$$\epsilon_1 E_{z1} = \epsilon_2 E_{z2} \tag{G-11}$$

At the surface ($z = 0$), we can compare the solutions for E_x and H_y in (G-1) and (G-3)

$$E_{x1}e^{i(k_{x1}x-\omega t)} = E_{x2}e^{i(k_{x2}x-\omega t)} \tag{G-12}$$

$$H_{y1}e^{i(k_{x1}x-\omega t)} = H_{y2}e^{i(k_{x2}x-\omega t)} \tag{G-13}$$

It should be apparent that for these two equivalencies to be valid, that the x-component

wavevectors are related

$$k_{x1} = k_{x2} = k_x \tag{G-14}$$

To prove the continuity in (G-11), we must use (G-5). The curl of the magnetic field is

$$\nabla \times \vec{H} = \left(\frac{\partial H_z}{\partial y} - \frac{\partial H_y}{\partial z}\right)\hat{\imath} + \left(\frac{\partial H_x}{\partial z} - \frac{\partial H_z}{\partial x}\right)\hat{\jmath} + \left(\frac{\partial H_y}{\partial x} - \frac{\partial H_x}{\partial y}\right)\hat{k} \tag{G-15}$$

The magnetic-field is zero in the x and z-directions and there is no variability in the x-direction,

so the curl reduces to

$$\nabla \times \vec{H} = -\frac{\partial H_y}{\partial z} = \frac{\epsilon}{c}\frac{\partial E_x}{\partial t} \tag{G-16}$$

Plugging in the respective values of the magnetic-field and electric-field from (G-1) and (G-2)

will give the solution of the curl outside the surface

$$k_{z2}H_{y2} = -\frac{\omega}{c}\epsilon_2 E_{x2} \tag{G-17}$$

The solution for inside the sphere is then

$$k_{z1}H_{y1} = \frac{\omega}{c}\epsilon_1 E_{x1} \tag{G-18}$$

The next step is to rearrange the two curl solution equations so that the electric field terms are

by themselves

$$-\frac{c}{\omega}\frac{k_{z2}}{\epsilon_2}H_{y2} = E_{x2} \qquad \text{(G-19)}$$

$$\frac{c}{\omega}\frac{k_{z1}}{\epsilon_1}H_{y1} = E_{x1} \qquad \text{(G-20)}$$

The continuity relation described in (G-9) and (G-10) allows us to relate them together and simplify

$$-\frac{c}{\omega}\frac{k_{z2}}{\epsilon_2}H_{y2} = \frac{c}{\omega}\frac{k_{z1}}{\epsilon_1}H_{y1} \qquad \text{(G-21)}$$

$$-\frac{c}{\omega}\frac{k_{z2}}{\epsilon_2}H_{y1} = \frac{c}{\omega}\frac{k_{z1}}{\epsilon_1}H_{y1} \qquad \text{(G-22)}$$

$$\frac{k_{z2}}{\epsilon_2} + \frac{k_{z1}}{\epsilon_1} = 0 \qquad \text{(G-23)}$$

We can further define the propagating wavevector (k_x) in (G-14) using the wave equation for the magnetic field. The magnetic field wave equation outside the sphere becomes

$$\left(\nabla^2 - \frac{\epsilon_2}{c^2}\frac{\partial^2}{\partial t^2}\right)\vec{H}_2 = 0 \qquad \text{(G-24)}$$

For clarity, we will perform the two different operators on the magnetic field outside the sphere separately and then combine them back together for the wave equation solution. Since the magnetic field for TM modes only has a y-component in this setup as shown in (G-2), the x and z-components will have a zero value and thus the magnetic field is decoupled. This means we will apply the operators only to the H_y components.

$$\nabla^2\vec{H} = \frac{\partial^2 H_{y2}}{\partial x^2} + \frac{\partial^2 H_{y2}}{\partial y^2} + \frac{\partial^2 H_{y2}}{\partial z^2} \qquad \text{(G-25)}$$

$$\nabla^2\vec{H} = (-k_{x2}^2 - k_{z2}^2)\vec{H} \qquad \text{(G-26)}$$

The next step is to perform the second part of the wave equation

185

$$\frac{\epsilon_2}{c^2}\frac{\partial^2}{\partial t^2}\vec{H} = -\epsilon_2\frac{\omega^2}{c^2}\vec{H} \tag{G-27}$$

Putting all the components back together gives a solution

$$\left(\epsilon_2\frac{\omega^2}{c^2} - k_{x2}^2 - k_{z2}^2\right)\vec{H} = 0 \tag{G-28}$$

Using the definition of the wavevector $(k_0 = \frac{\omega}{c})$, we can reorganize and substitute (G-14) into

(G-27)

$$\epsilon_2 k_0^2 = k_x^2 + k_{z2}^2 \tag{G-29}$$

The wavevector equation for the outer sphere holds true for the inner sphere as well with the

required value changes.

$$\epsilon_1 k_0^2 = k_x^2 + k_{z1}^2 \tag{G-30}$$

The final steps are to substitute in (G-23) and (G-29) into (G-28) after some rearranging and

solve for k_x. Every step will be displayed for reference as no textbook shows these steps to my

knowledge.

$$k_x^2 = \epsilon_2 k_0^2 - k_{z2}^2 \tag{G-31}$$

$$k_x^2 = \epsilon_2 k_0^2 - \left(\frac{\epsilon_2^2}{\epsilon_1^2}\right)(k_x^2 - \epsilon_1 k_0^2) \tag{G-32}$$

$$k_x^2 + \frac{\epsilon_2^2}{\epsilon_1^2}k_x^2 = \epsilon_2 k_0^2 + \frac{\epsilon_2^2}{\epsilon_1}k_0^2 \tag{G-33}$$

$$\frac{\epsilon_1^2}{\epsilon_1^2}k_x^2 + \frac{\epsilon_2^2}{\epsilon_1^2}k_x^2 = \frac{\epsilon_1\epsilon_2}{\epsilon_1}k_0^2 + \frac{\epsilon_2^2}{\epsilon_1}k_0^2 \tag{G-34}$$

$$\frac{\epsilon_1^2 + \epsilon_2^2}{\epsilon_1^2}k_x^2 = \frac{\epsilon_2}{\epsilon_1}(\epsilon_1 + \epsilon_2)k_0^2 \tag{G-35}$$

$$\frac{\epsilon_1^2 + \epsilon_2^2}{\epsilon_1 \epsilon_2} k_x^2 = (\epsilon_1 + \epsilon_2) k_0^2 \qquad \text{(G-36)}$$

$$k_x^2 = \frac{\epsilon_1 \epsilon_2}{\epsilon_1 + \epsilon_2} k_0^2 \qquad \text{(G-37)}$$

$$k_x = k_0 \sqrt{\frac{\epsilon_1 \epsilon_2}{\epsilon_1 + \epsilon_2}} \qquad \text{(G-38)}$$

This is the dispersion relation for a p-polarized EM wave propagating in the x-direction.